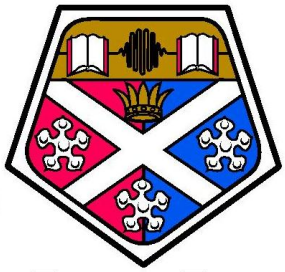

University of Strathclyde Glasgow

DEPARTMENT OF PHYSICS

Generation and transport of high-current relativistic electron beams in high intensity laser-solid interactions

by

Mireille COURY

A thesis submitted in fulfillment of the requirements for the degree of Doctor of Philosophy in Physics

2013

Copyright Declaration

Signed:

Date: 30.May.2013

Abstract

In this thesis, the generation and transport of ultra-high intensity laser-driven relativistic electron beams in overdense plasma is investigated experimentally and numerically. The fast electron beam is experimentally diagnosed by means of a 2D Cu Kα imager and the TNSA-generated proton beam. Analytical models together with a 3D hybrid-PIC code are employed to simulate the beam properties in solids. The effects of the self-generated fields on the fast electron beam transport, the effect of the preplasma density scale length on the laser energy coupling to fast electrons and the influence of the laser spot size on the fast electron beam generation and transport, and on the subsequent proton beam, are reported.

Fast electron injection and transport in metal foils irradiated at laser intensity up to 4×10^{20} W/cm^2, is investigated . The beam transport is simulated over a wide range of beam source conditions and with or without inclusion of self-generated magnetic fields. The resulting hot electron beam properties are used in rear-surface plasma expansion calculations to compare with measurements of the beam of accelerated protons. An injection half-angle of $\sim 50^\circ - 70^\circ$ is inferred, which is larger than that derived from previous experiments under similar conditions.

The influence of laser spot size on laser energy coupling to electrons, and subsequently to the TNSA-generated protons, in foil targets is reported. Proton acceleration is characterized for laser intensities ranging from 2×10^{18} - 6×10^{20} W/cm^2, by variation of the laser energy for a fixed spot size, and by variation of the spot size for a fixed energy. At a given laser pulse intensity, the maximum proton energy is higher under defocus illumination compared to tight focus. The results are explained in terms of higher laser pulse energy and geometrical changes to the hot electron injection.

The laser-to-electron energy conversion efficiency is investigated in metal foils over a wide range of preplasma density scale lengths. A hybrid-PIC code is employed to model the fast electron beam transport in the solid, for a given hot electron source. The resulting fast electron density is used to infer the maximum proton energy for comparison with experimental results. It is shown, in agreement with previous published work, that some preplasma density scale length leads to an enhancement of the energy coupling efficiency of laser light to fast electrons.

Acknowledgement

I would like to thank my supervisor Paul McKenna. I would like also to thank Alex Robinson, Bernhard Ertsfeld and Raoul Trines for their theoretical support. Thanks also goes to Gregory Vieux, the rest of the SILIS group at Strathclyde University and John Pasley for their support. Finally, I would like to to thank the collaborators who I have worked with on the different experiments. This work is dedicated to Sherine Yahmi.

Role of the author & list of publications

During her PhD, the author has participated in the planning, set-up and running of four experimental campaigns. She also participated in the radiation commissioning of the target area on the Gemini laser and in the beamline set-up, for an experimental campaign, of target area west on the Vulcan laser. This includes diagnostics choice, design, assembling and alignment in the target area as well as a day-to-day operation of these diagnostics (mainly X-ray 2D imager, X-ray spectrometer diagnostics and proton RCF stack diagnostics). After the experimental run the author has performed complete experiment data analysis (X-ray and proton data), including the development of analytical models and the use of numerical simulation codes (Hybrid-PIC and PIC codes). The author has two first-author peer-reviewed papers [1, 2] resulting from work presented in this thesis.

1. **"Influence of laser irradiated spot size on energetic electron injection and proton acceleration in foil targets"**, M. Coury, D. C. Carroll, A.P.L. Robinson, X. H. Yuan, C. M. Brenner, M. Burza, R. J. Gray, M. N. Quinn, K. L. Lancaster, Y. T. Li, X. X. Lin, O. Tresca, C.-G. Wahlström, D. Neely, and P. McKenna, *Applied Physics Letters*, **100**, 074105, 2012.

2. **"Injection and transport properties of fast electrons in ultraintense laser-solid interactions"**, M. Coury, D. C. Carroll, A.P.L. Robinson, X. H. Yuan, C. M. Brenner, M. Burza, R. J. Gray, K. L. Lancaster, Y. T. Li, X. X. Lin, D. A. MacLellan, H. Powell, M. N. Quinn, O. Tresca, C.-G. Wahlström, D. Neely, and P. McKenna, *Physics of plasma*, **20**, 043104, 2013.

3. **"Controlling the properties of ultra-intense laser-proton sources using transverse refluxing of hot electrons in shaped mass-limited targets"**, O. Tresca, D. C. Carroll X. H. Yuan, B. Aurand, V. Bagnoud, C. M. Brenner, M. Coury, J. Fils, R. J. Gray, T. Kühl, C. Li, Y. T. Li, X. X. Lin, M. N. Quinn, R. G. Evans, B. Zielbauer, M. Roth, D. Neely and P. McKenna, *Plasma Physics and Controlled Fusion*, **53**, 10, 2011.

4. **"Spatially resolved X-ray spectroscopy using a HOPG crystal"**, X. H. Yuan, D. C. Carroll, M. Coury, R. J. Gray, C. M. Brenner, X. X.

Lin, Y. T. Li, M. N. Quinn, O. Tresca, and B. Zielbauer, D. Neely, and P. McKenna, *Nuclear Instruments and Methods in Physics Research Section A: Accelerators, Spectrometers, Detectors and Associated Equipment*, **6531**, 145-149, 2011.

5. **"Refluxing of fast electrons in solid targets irradiated by intense, picosecond laser pulses"**, M. N. Quinn, X. H. Yuan, X. X. Lin, D. C. Carroll, O. Tresca, R. J. Gray, M. Coury, C. Li, Y. T. Li, B. Aurand, J. Fils, T. Kühl and P. McKenna, *Plasma Physics and Controlled Fusion*, **532**, 025007, 2011.

6. **"Effect of Lattice Structure on Energetic Electron Transport in Solids Irradiated by Ultraintense Laser Pulses"**, P. McKenna, A. P. L. Robinson, D. Neely, M. P. Desjarlais, D. C. Carroll, M. N. Quinn, X. H. Yuan, C. M. Brenner, M. Burza, M. Coury, P. Gallegos, R. J. Gray, K. L. Lancaster, Y. T. Li, X. X. Lin, O. Tresca and C-G. Wahlström, *Physical Review Letters*, **106**, 185004, 2011.

7. **"Surface transport of energetic electrons in intense picosecond laser-foil interactions"**, R. J. Gray, X. H. Yuan, D. C. Carroll, C. M. Brenner, M. Coury, M. N. Quinn, O. Tresca, B. Zielbauer, B. Aurand, V. Bagnoud, J. Fils, T. Kühl, X. X. Lin, C. Li, Y. T. Li, M. Roth, D. Neely, and P. McKenna, *Applied Physics Letters*, **99**, 171502, 2011.

8. **"Soft-X-Ray Harmonic Comb from Relativistic Electron Spikes"**, A. S. Pirozhkov, M. Kando, T. Zh. Esirkepov,P. Gallegos, H. Ahmed, E. N. Ragozin, A.Ya. Faenov, T. A. Pikuz, T. Kawachi, A. Sagisaka, J. K. Koga, M. Coury, J. Green, P. Foster, C. Brenner, B. Dromey, D. R. Symes, M. Mori, K. Kawase, T. Kameshima, Y. Fukuda, L. Chen, I. Daito, K. Ogura, Y. Hayashi, H. Kotaki, H. Kiriyama,1 H. Okada,1 N. Nishimori,7 T. Imazono,1 K. Kondo,1 T. Kimura,1 T. Tajima,1 H. Daido,1 P. Rajeev,2 P. McKenna, M. Borghesi, D. Neely, Y. Kato, and S.V. Bulanov, *Physical Review Letters*, **108**, 135004, 2012.

9. **"Relativistic high-current electron-beam stopping-power characterization in solids and plasmas: Collisional versus resistive effects"**, B. Vauzour, J. J. Santos, A. Debayle, S. Hulin, H.-P. Schlenvoigt, X. Vaisseau, D. Batani, S. D. Baton, J. J. Honrubia, Ph. Nicola; F. N. Beg, R. Benocci, S. Chawla, M. Coury, F. Dorchies, C. Fourment, E. dHumieères, L. C. Jarrot, P. McKenna, Y. J. Rhee, V. T. Tikhonchuk, L. Volpe, and V. Yahia , *Physical Review Letters*, **109**, 255002, 2012.

Contents

List of Figures

List of Tables

Chapter 1

Introduction

With the advent of the chirped pulse amplification (CPA) technique [3] in the 1980s, state of the art laser systems can now deliver peak intensities on target of the order of 10^{21}-10^{22} W.cm^{-2}. These ultra-high intensities have enabled the investigation of numerous nonlinear and relativistic phenomena and have provided great stimulation for the development of approaches in controlled nuclear fusion. One of these applications concerns the fast ignition (FI) scheme, as proposed by Tabak *et al.* in 1994 [4]. In this scheme, a solid D-T target is compressed to a density of $\sim$400 g/cm^3 with a high-energy, nanosecond laser pulse in direct- or indirect-drive mode. Following this, an ultra-high intensity (UHI) laser acts as the initiator for the fusion burn. For the ignition a typical laser pulse of $\sim$100-200 kJ in 10-20 ps is required. The pulse bores through the expanding lower density plasma surrounding the target and, at the relativistic critical density surface, a large fraction of its energy is converted into electrons with an average energy of $\sim$1 MeV [5]. In the FI concept, this electron beam is pictured as traversing a density gradient of approximately four orders of magnitude in a well defined narrow column, depositing its energy in the compressed core and heating it so fast that the process is isochoric, *i.e.* without a change of density [4–6]. Thus, the FI scheme relies on the production and transport of well defined electron beams and involves complex plasma physics such as self-focusing, hole-boring and relativistic effects.

Fast electron generation during laser-overdense plasma interactions are theoretically and experimentally widely investigated. However, the generation, transport and control of well defined electron beams, subject to many interrelated plasma phenomena, is far from fully understood. The author's research project concerns the investigation and control of the production and transport of fast electrons beams in dense matter. More specifically, (1) the effect of the self-generated magnetic field on the fast electron beam injection and transport divergence angles in metal targets, (2) the effect of the preplasma density scale length on the laser-to-electron energy conversion efficiency in metal targets, and (3) the influence of the laser irradiated spot size on both fast electrons and proton acceleration.

1.1 Motivation

Transport of energy and heating by relativistic electrons is an important aspect of high energy density physics. The properties of dense matter, the production of secondary radiation sources [7], the generation of high intensity ion beams [8–10], and fast ignition of fusion targets, using fast electrons to ignite a precompressed D-T target, are included in this field.

Inertial confinement fusion (ICF)

ICF is one of two approaches to controlled fusion intended to ensure a future of clean, safe and abundant energy generation in order to meet long-term demand for electricity. Fusion reactions bring two atoms very close together such that they fuse, releasing great amounts of energy. The fuel pellet contains 100s of micrograms of deuterium and tritium. These two hydrogen isotopes fuse together to form a He-4 nucleus and emit a high energy neutron

$$D + T \rightarrow 4He(3.5MeV) + n(14.1MeV)$$

Two research routes are investigated to fusion energy :

- Magnetic Confinement Fusion, usually based around 'tokamak' type facilities, producing a low density plasma ($\sim 10^{14}$ cm^{-3}) over a relatively long period of time (100s of seconds).
- Laser-driven ICF, on experimental research facilities such as the National Ignition Facility (NIF) in the US or the European project HIPER in the future, produces very dense plasma ($\sim 10^{26}$ cm^{-3}) but only for very short periods of time ($\sim 10^{-11}$ s).

The ICF fusion energy release, represented in figure (1.1), is generated by compressing the fuel to a density of 100s of g/cm^3 and heating the central region of this fuel to million degrees Celsius, in a short period of time ($\sim$ 20 ns). This is achieved by rapidly ablating the outer part of the pellet. The rest of the pellet moves towards the center, compressing the DT mixture. Very high temperatures are then achieved at the center (hotspot), and the hotspot ignites the rest of the fuel.
The fuel can be compressed in two ways:

- Direct Drive consists of imploding the pellet of DT by laser beams directly focused on the target.
- Indirect drive [11], the laser beams are directed on to the internal walls of a high-Z cylinder, called a hohlraum, containing the pellet in order to produce intense X-ray radiation. The radiation is trapped within this cavity where the temperature can reach 3-4 $\times 10^6$ degrees. The X-rays rapidly heat the outer surface of the pellet, rapidly ablating the surface material and imploding the fuel capsule in a similar manner to that achieved with the lasers directly in Direct Drive.

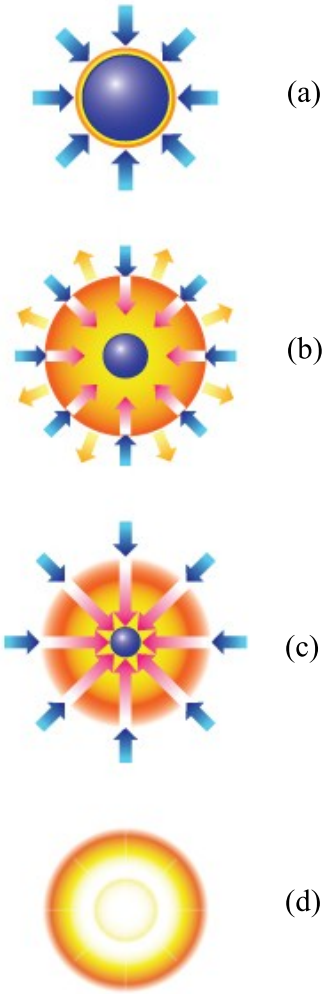

Figure 1.1: ICF sequence reproduced from [12]: (a) The laser beam rapidly heats the surface of the fusion target forming a surrounding plasma envelope; (b) The fuel is compressed by rocket-like blowoff of the hot surface material; (c) The fuel core reaches 20 times the density of lead and ignites at 100,000,000 degrees Celsius; (d) Thermonuclear burn spreads rapidly through the compressed fuel, yielding many times the input energy.

There are also two ways to start the fusion reaction, by central hotspot ignition where the central area is heated and compressed through compression or, alternatively by fast ignition.
The fast ignition approach, represented in figure (1.2), decouples the phases of compression and heating of the DT pellet. The compression is achieved with con-

ventional ICF lasers (peak intensity of $\sim 10^{15}$ W.cm^{-2}, pulse duration of 10s of ns). The compression must be done as adiabatically as possible and, ideally, without creating the central hot spot. A mm-length underdense plasma surrounds the fuel. An UHI short pulse laser ($\sim 10^{18}$ W.cm^{-2}, $\sim$100 ps) bores a channel in the subcritical corona, and pushes the critical surface towards the dense core of the capsule. This channel is then used as guide for the UHI short pulse ignitor laser ($\geq 10^{20}$ W.cm^{-2}, $\sim$1 ps) which lunches an intense fast electron beam in to the dense fuel. The fast electrons (with mean energies $\sim 1-3$ MeV) travel a few 100s of microns and then step in a small region of the compressed core a few 10s of μm across to achieve ignition, as shown in figure (1.3). Simulations of Atzeni *et al.* [13] indicated that efficient heating can be obtained by an energy of 10 to 20 kJ contained in MeV electrons injected within 20 ps over a region of 30 μm.

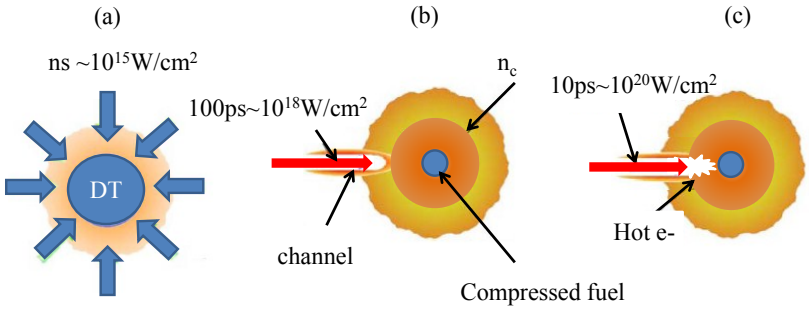

Figure 1.2: Fast ignition concept: (a) Fuel compression by nanosecond laser pulses; (b) Creation of a density channel by an ultra-high intensity laser pulse through the low density ablated plasma up to the critical density (n_c); (c) Fast electron generation by an UHI laser pulse propagating through the channel, transport through the overdense plasma and fuel ignition

The control of the fast electron beam divergence and temperature is crucial to achieve ignition. If the beam is too divergent, the electrons will inefficiently heat the fuel. Many factors can affect the beam divergence, such as the laser intensity [14, 15], the background plasma density and structure [16, 17], the preplasma density scale length [18–20], beam-plasma instabilities [21, 22] and the self-generated magnetic fields [23–25]. Equally, inefficient heating can be also due to a mismatch between the required and the effective fast electron beam temperature [26]. This thesis is concerned with the laser energy coupling to fast electrons under different preplasma conditions and the control of the fast electron beam divergence by means of self-generated fields.

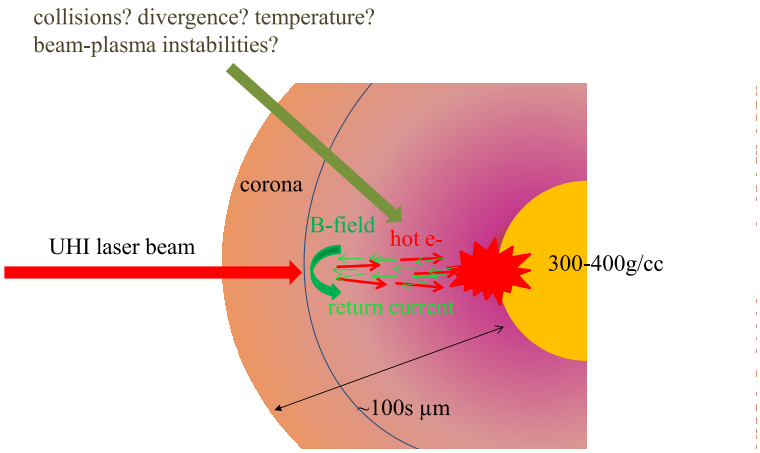

Figure 1.3: Fast ignition concept: fast electron generation and transport in overdense plasma.

For neither approach to ignition has been successful, although it is hoped that ignition will be demonstrated by the central hotspot approach approach within the next few years at the NIF. Achieving a high enough laser-to-electron energy conversion efficiency, matching the fast electron energy to the hot spot and the transport of the fast electron beam in hot dense plasma are also major obstacles to achieve fast ignition.

Generation of high-quality sheath-accelerated ion beams

Driving laser generated fast electrons into a solid target, as shown in figure (1.4), leads to ion acceleration at the front and rear of the target-vacuum boundaries [10, 27]. The mechanism for such is discussed in chapter 3. Basically, the target normal sheath acceleration (TNSA)-generated ion beam maximum energy being proportional to the fast electron beam density, is then dependent on the fast electrons divergence and number (laser-to-fast electron energy coupling). Therefore, minimizing the fast electron beam divergence and increasing the laser energy absorption into fast electrons will enhance the properties of the TNSA- generated ions.

The generation of multi-MeV proton beams has been intensively studied, and having low transverse emittance and given their a localized energy deposition (Bragg peak), several applications have been proposed and tested.

One of the applications suggested is proton and ion cancer therapy [28]. The sources for such are presently generated by means of synchrotron/cyclotron accelerators [29], could be considerably down-sized and cost effective if a compact, high-quality laser-driven accelerator can be developed [30–34]. The high energy density and short bunch duration of the ion beam allow it to heat up solid density matter, and create matter at 1-10 times solid density and temperatures up to 100 eV (Warm Dense Matter) [9, 35]. Protons and ions are alternatives [36] to electrons in fast ignition, in spite of being generated less efficiently, due to their highly localized energy deposition profile, the low emittance of the beam and its subsequent high focusability [37].

Secondary X-ray emission

Multi MeV electrons, generated during laser-solid interaction, generate MeV bremsstrahlung X-ray emission [38] as they propagate into a (high-Z) solid target. Those X-ray photons have been used to obtain high resolution radiographic images of dense media that is evolving rapidly [39]. Gamma rays can be produced

by high energy electrons [40]. The X-rays can also be used as a diagnostic in fast electron transport experiments [41–43].

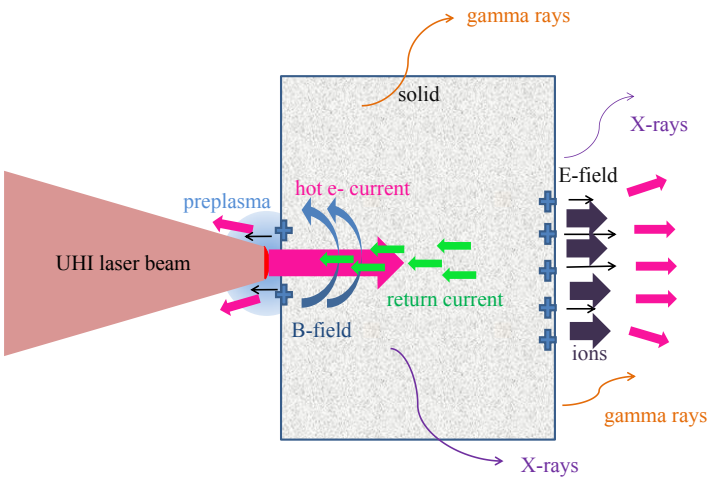

Figure 1.4: Target normal sheath acceleration: The laser amplified spontaneous emission (ASE) creates a preplasma on the target front surface. The main pulse interacts with the preplasma and accelerates hot electrons into the overdense plasma region, at the critical density. The electrons travel through the target, subject to self-generated fields, beam-plasma instabilities and collisions with the background material, altering the divergence of the hot electron current. Some of the hottest electrons escape into the vacuum at the rear side, resulting in a dense sheath. An electric field due to charge-separation is then created. This field, of the order of (TV/m), ionizes and accelerates atoms at the surface; Collisions of the hot electrons with the background plasma lead to the generation of secondary X-ray emissions.

1.2 Thesis layout

This thesis is divided into two main parts corresponding to the basic theory and discussion of the physics of laser-generated fast electrons and to the experimental and modeling work of the author. The next two chapters introduce the basic

theoretical background and the final three chapters cover the experimental work that has been carried out by the author. Chapter 2 presents a brief introduction to laser produced plasmas and fast electron generation mechanisms in overdense plasma. Chapter 3 describes the main processes involved in fast electron transport in overdense plasma. Chapter 4 presents an example of a CPA laser chain, the propagation of a laser beam in vacuum, the work on large scale facilities and the main diagnostics used during the different experimental campaigns in this project. Chapter 5 reports investigation of various factors, such as self-generated fields and the background plasma density, that alter the fast electron beam divergence. Chapter 6 presents the effect of the laser spot size on the fast electron beam injection and transport and consequently, on the TNSA-generated protons. Chapter 7 describes the effect of the preplasma on the laser to fast electron energy coupling, and on the maximum proton energy at a given laser intensity. Finally, a conclusion of the main results and future work is given in chapter 8.

Chapter 2

Fast electron generation in picosecond ultra-high intensity laser-solid interactions

This chapter provides the theoretical foundations of ultra high intensity laser-plasma interactions. The basics of the laser-generated plasma, different absorption mechanisms and the properties of the fast electron source are discussed.

2.1 Description of a plasma

Plasma is referred to as the fourth state of matter after solid, liquids and gases. Plasma can be described as ionized gas composed of electrons and ions. Ionization can occur through heating or photoionization. When a gas or solid is heated sufficiently, collisions between atoms free bound electrons, thus creating a plasma. In equilibrium, plasma is quasi-neutral. Any space-charge separation between ions and electrons gives rise to electric fields while a flow of charged particles gives rise to current generated fields, i.e. magnetic fields. These fields are responsible for a wide range of phenomena, giving plasmas unique properties. This section presents a basic description of plasma [44, 45].

2.1.1 Basic concept

Plasma consists of N species of charged particles (ions (N-1) and electrons) coupled by the electric and magnetic fields they generate, and subject to fields that are applied externally. The ions and electrons have distributions in energy, characterized by temperatures T_i and T_e , which are not necessarily the same. In equilibrium, plasma is electrically neutral on length scales much larger than the Debye length λ_D, the characteristic electrostatic screening scale defined in later in this section. The plasma can be collisional or collisionless (collisions are reduced at high temperatures as the collision rate scales with $T^{-3/2}$), and the self-generated fields give rise to collective, coherent motion of particles.

In principle, the plasma behavior could be investigated at the microscopic level by tracking the position and momentum of all the particles in the plasma. This would imply that the equation of motion were solved for every single particle, which is unrealistic for large volume dense plasmas. A feasible solution is to reduce the degrees of freedom, via a kinetic description of the plasma, by using a macroscopic statistical description of each species in the plasma leading to a Vlasov or Vlasov Fokker Planck equation. Finally, the fluid description reduces further the degrees of freedom by evaluating only the charge and current densities (and possibly the temperature).

The different methods are described in the next subsection and summarized in figure 2.1. Unless specified, the plasma described in the next subsections is a collisionless fully ionized plasma with no recombination, composed of j particles, N species in a volume V.

2.1.2 Vlasov equation

The distribution function $f_s(\mathbf{r}, \mathbf{v}, t)$ is a 6-D phase space distribution function which characterizes the location of species in position $\mathbf{r}$ and velocity $\mathbf{v}$ as a function of time t [44]. As there is no ionization or recombination, $f_s(\mathbf{r}, \mathbf{v}, t)$ must

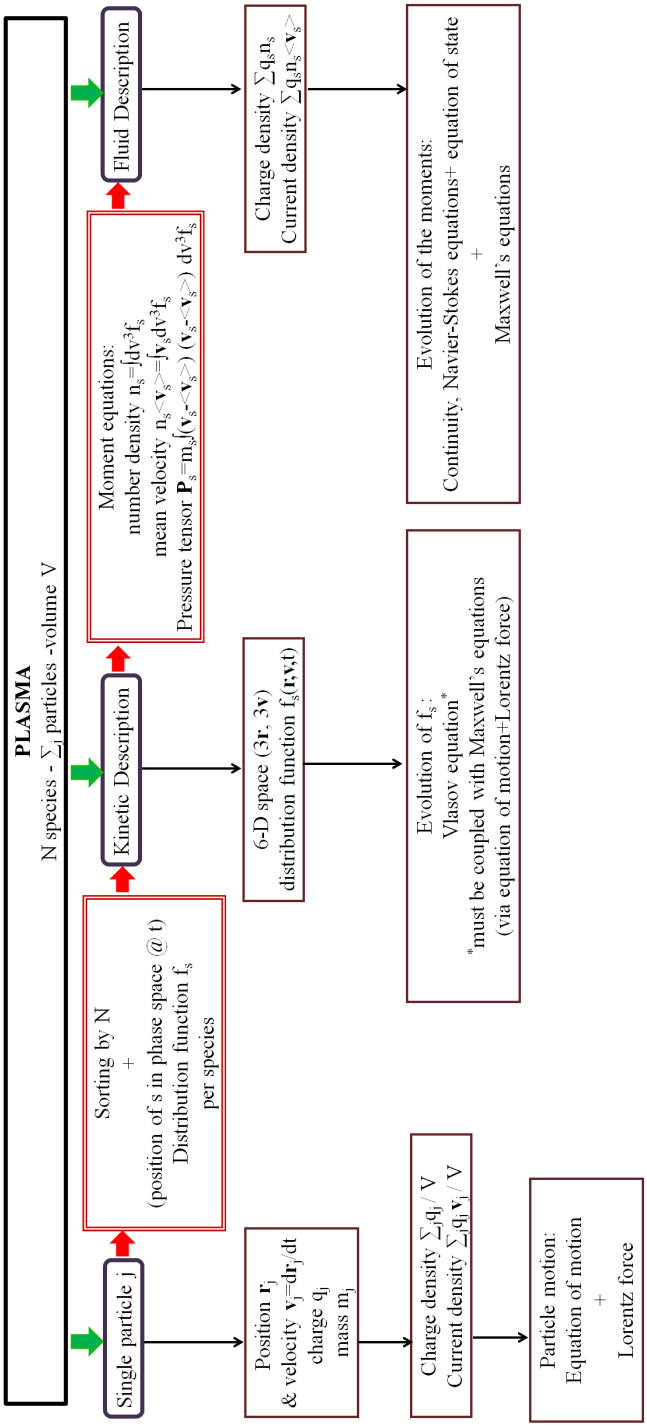

Figure 2.1: Methods to describe a plasma.

obey the continuity equation (conservation of number)

$$\frac{\partial f_s}{\partial t} + \frac{\partial}{\partial \mathbf{r}}(\mathbf{v} f_s) + \frac{\partial}{\partial \mathbf{v}}(\dot{\mathbf{v}} f_s) = 0, \tag{2.1}$$

with $\dot{\mathbf{v}}$ the acceleration that is given by the equation of motion and the Lorentz force

$$\dot{\mathbf{v}} = \frac{q_s}{m_s}(\mathbf{E} + \mathbf{v} \times \mathbf{B}), \tag{2.2}$$

with m_s the mass and q_s the charge of the species s. $\mathbf{E}$ and $\mathbf{B}$ the self-generated electric and magnetic fields associated with the collective behavior.
$\mathbf{E}$ and $\mathbf{B}$ derive from Maxwell's equations

$$\nabla \cdot \mathbf{E} = \frac{\rho}{\epsilon_0}, \tag{2.3}$$

$$\nabla \cdot \mathbf{B} = 0 \tag{2.4}$$

$$\nabla \times \mathbf{E} = -\frac{\partial \mathbf{B}}{\partial t} \tag{2.5}$$

$$\nabla \times \mathbf{B} = \mu_0 \epsilon_0 \frac{\partial \mathbf{E}}{\partial t} + \mu_0 \mathbf{J}, \tag{2.6}$$

with ϵ_0 the vacuum permittivity, ρ the total charge density, μ_0 the vacuum permeability and $\mathbf{J}$ the total current density and c the speed of light.
The Vlasov equation, describing the time evolution of the distribution function (with $\mathbf{r}(t)$ and $\mathbf{v}(t)$), is equation (2.2) substituted in equation (2.1)

$$\frac{\partial f_s}{\partial t} + \mathbf{v}.\frac{\partial f_s}{\partial \mathbf{r}} + \frac{q_s}{m_s}(\mathbf{E} + \mathbf{v} \times \mathbf{B}).\frac{\partial f_s}{\partial \mathbf{v}} = 0 \tag{2.7}$$

The collisionless plasma is fully described by the Vlasov equation augmented with Maxwell's equations.

2.1.3 The moment equations: Fluid equations

The distribution function allows the calculation for each species (by integration over velocities), of the number density (also referred to as density in the rest of the manuscript) n_s, the mean velocity $< \mathbf{v_s} >$ and the pressure tensor $\mathcal{P}_\mathbf{s}$

$$n_s = \int f_s(\mathbf{r}, \mathbf{v}, t) d^3v \tag{2.8}$$

$$< \mathbf{v_s} > = \frac{1}{n_s} \int \mathbf{v_s} f_s(\mathbf{r}, \mathbf{v}, t) d^3v \tag{2.9}$$

$$\mathcal{P}_\mathbf{s} = m_s \int (\mathbf{v_s} - < \mathbf{v_s} >)(\mathbf{v_s} - < \mathbf{v_s} >) f_s(\mathbf{r}, \mathbf{v}, t) d^3v \tag{2.10}$$

Different moments of the Vlasov equation (2.7) link these macroscopic parameters. Averaging the Vlasov equation over velocities gives

$$\int d^3v \left[\frac{\partial f_s}{\partial t} + \mathbf{v}.\frac{\partial f_s}{\partial \mathbf{r}} + \frac{q_s}{m_s}(\mathbf{E} + \mathbf{v} \times \mathbf{B}) \frac{\partial f_s}{\partial \mathbf{v}} \right] = 0 \tag{2.11}$$

The first moment of the Vlasov equation leads to the continuity equation (particle conservation)

$$\frac{\partial n_s}{\partial t} + \frac{\partial}{\partial \mathbf{r}}.(n_s < \mathbf{v_s} >) = 0 \tag{2.12}$$

The next moment leads to the force equation for the velocity (Navier-Stokes equation). Assuming an isotropic pressure $\mathcal{P}_\mathbf{s} = \mathbf{I} p_s$, with $\mathbf{I}$ the identity matrix and p_s the scalar pressure.

$$m_s n_s \left[\frac{\partial < \mathbf{v_s} >}{\partial t} + < \mathbf{v_s} >. \frac{\partial < \mathbf{v_s} >}{\partial \mathbf{r}} \right] = n_s q_s (\mathbf{E} + < \mathbf{v_s} > \times \mathbf{B}) - \frac{\partial p_s}{\partial \mathbf{r}}, \tag{2.13}$$

As can be noticed, the equation for each moment of the Vlasov equation calls for the next order. In order to close the system, the moment equations can be truncated by making assumptions about the heat transfer, expressed in the equation of state. The equation of state gives the spatial and temporal evolution of a macroscopic parameter such as the pressure. For example, the ideal gas law is

one of the equations of state $p_s = n_s k_B T_s$, with k_B the Boltzmann constant, that can be used.

Thus, the fluid equations (2.12,2.13), coupled with the equation of state and Maxwell's equations describe the plasma. A plasma composed of electrons and one species of ions constitute the so-called **two-fluid model**. The full derivation of the moments equation can be found in [44].

2.1.4 Vlasov Fokker Planck (VFP) equation

The **collisional** plasma is described by the VFP equation. Collisions occur between pairs of charged particles as the plasma is considered fully ionized. The charged particles collide via Coulomb collisions, i.e. interactions on a timescale much shorter than the typical time evolution of the fields in the averaged model. As for the collisionless plasma, the temporal evolution of the collisional plasma can be described kinetically or hydrodynamically. Therefore, a distribution function and an equation describing its time evolution need to be defined. The latter is the so-called VFP equation. The VFP equation is basically the Vlasov equation (2.7) with an additional term modeling collisions between the particles

$$\frac{\partial f_s}{\partial t} + \mathbf{v}.\frac{\partial f_s}{\partial \mathbf{r}} + \frac{q_s}{m_s}(\mathbf{E} + \mathbf{v} \times \mathbf{B}).\frac{\partial f_s}{\partial \mathbf{v}} = \left(\frac{\partial f_s}{\partial t}\right)_{coll}, \tag{2.14}$$

with $\left(\frac{\partial f_s}{\partial t}\right)_{coll}$ giving the temporal evolution of the distribution function due to collisions. The electron collision term $\left(\frac{\partial f_s}{\partial t}\right)_{coll}$ is the sum of contributions from electron-electron collisions (C_{ee}) and electron-ion collisions (C_{ei}).

Coulomb collisions force the particles to randomly exchange energy and gradually drive them into thermal equilibrium. For a plasma, the charged particles have a Boltzmann or Maxwell-Boltzmann velocity distribution.

2.1.5 The plasma wave

This subsection presents the main characteristic parameters associated with the collective effects in a plasma. The full derivation of these parameters can be found in [44, 45].

2.1.5.1 Debye shielding

Inside the plasma, a charged particle attracts/repulses other particles with opposite/same charge. The cloud of charges surrounding the particle give rise to the particle's Coulomb field falling off exponentially at large radii r (rather than falling as $1/r^2$). As an example, a single charge Q at rest is placed in a plasma with electrons and ions. The electron and ion density, n_e and n_i, are both described by a Boltzmann distribution. Furthermore, charge neutrality imposes the electron mean charge density to be equal to the ion mean charge density ($n_e = Zn_i$, with Z the atomic number). Starting with an isothermal system, the electron temperature is equal to the ion temperature $T_e = T_i$. The electrostatic potential $\Phi(r)$ of the single charge Q can be derived as [44] $\Phi(r) = \frac{Q}{4\pi\epsilon_0 r}\exp(-r/\lambda_D)$, with λ_D the Debye length. λ_D is given by

$$\lambda_D = \sqrt{\frac{\epsilon_0 k_B T_e}{[n_e(Z+1)]e^2}}, \tag{2.15}$$

with n_e the electron density and the electron charge e.

2.1.5.2 Cold plasma oscillation

One of the phenomena occurring in a plasma is the oscillation of the plasma electrons and ions. Electromagnetic oscillations (light waves) can also exist in a plasma. The plasma frequency corresponds to the typical electrostatic oscillation frequency of a given species in response to a small charge separation. For instance, consider a 1D situation where the electrons are displaced from their equilibrium

by a distance δr, leaving the protons unmoved. An electric field $E = en_e\delta r/\epsilon_0$, proportional to δr, is generated due to charge separation. The electric field pulls back and accelerates both the plasmas electrons and ions. The ion acceleration can be neglected due to fact that ions are much heavier than electrons. Solving the equation of motion, it is found that the electrons oscillate sinusoidally at the electron plasma frequency given by

$$\omega_{pe}[rad/s] = \sqrt{\frac{n_e e^2}{\epsilon_0 m_e}}, \tag{2.16}$$

with m_e the electron mass and m_p the proton mass.
The ion plasma frequency is given by $\omega_{pi}[rad/s] = \sqrt{\frac{n_i Z^2 e^2}{\epsilon_0 m_i}}$, with n_i and m_i the ion density and mass.

2.1.5.3 Dispersion relation: The critical density

Waves of different frequency travel at different velocities in a dispersive medium. Their frequency ω can be expressed as a function of the wavenumber k. For a light wave in vacuum, the dispersion relation is linear as the frequency is proportional to the wavenumber $\omega = ck$. The dispersion relation for an electromagnetic (EM) wave propagating in an electron plasma is

$$\omega^2 = \omega_{pe}^2 + k^2 c^2, \tag{2.17}$$

with ω_{pe} the electron plasma frequency. It can be noticed, in (2.17), that ω_{pe} is the minimum frequency for light propagation in an electron plasma as k becomes imaginary for $\omega < \omega_{pe}$. Therefore, $\omega = \omega_{pe}$ defines the maximum plasma density, called the critical density n_c defined later in this chapter, to which the EM wave can penetrate.

2.1.6 Collisions and Plasma Resistivity

This subsection presents the main parameters characterizing electron collisions in a two-species plasma and the resulting plasma resistivity.

2.1.6.1 Coulomb collisions

The plasma considered is a two-species electron-ion plasma with the ions immobile, and only collisions of electrons with ions are taken into account. Collisions of electrons in the plasma lead to resistivity and provide a mechanism for heating (ohmic heating or joule heating).

To approximate the plasma resistivity [46], consider an electron impinging on an ion which is at rest. Figure 2.2 shows the trajectory of an electron deflected by the Coulomb field of an ion, with b the impact parameter and θ the scattering angle.

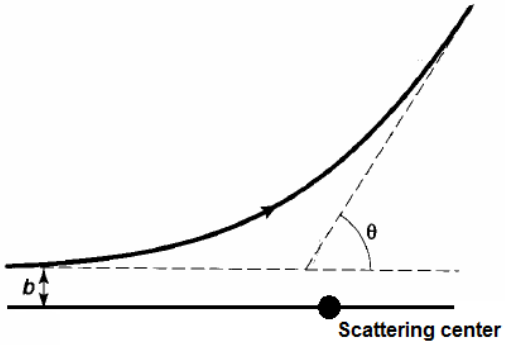

Figure 2.2: Trajectory of en electron deflected by the Coulomb field of an ion.

An expression of the impact parameter as a function of θ can be obtained, at the large angle limit $\theta = \pi/2$, using conservation of momentum and energy: $b_{90} = Ze^2/(4\pi\epsilon_0 m_e v_e^2)$.

The ion scattering cross section, corresponding to the area which describes the likelihood of a particle to be scattered by another particle, for 90° scattering can be estimated by: $\sigma_{90} = \pi b_{90}^2$. Substituting the expression of b_{90} in the expression of σ_{90} leads to $\sigma_{90} = \pi[Ze^2/(4\pi\epsilon_0 m_e v_e^2)]^2$. The collision frequency at large angle,

ν_{90}, is obtained by considering the flux of particles coming into this cross section

$$\nu_{90} = n_e v_e \sigma_{90} = \frac{\pi n_e Z^2 e^4}{(4\pi\epsilon_0)^2 m_e^2 v_e^3} \tag{2.18}$$

However, the Coulomb force is a long-range force and therefore small angle interactions need to be taken into account. Spitzer *et al.* [47] shows that the scattering cross section, integrated over all impact parameters, is larger than σ_{90} by the factor $\ln\Lambda$, called the Coulomb logarithm. The collision frequency at any impact angle, ν_{ei}, is given by

$$\nu_{ei} = \frac{n_e Z^2 e^4}{(4\epsilon_0)^2 \pi m_e^2 v_e^3} \ln\Lambda, \tag{2.19}$$

where Λ is the ratio of the maximum impact parameter $\sim \lambda_D$ and the minimum impact parameter b_{min}. b_{min} is taken equal to b_{90} in the classical case. $\ln\Lambda$ ranges between 3 and 10 over most of the accessible range of density and temperature for a plasma.

2.1.6.2 Plasma resistivity

When an electric field is applied to a plasma, electrons are accelerated opposite to $\mathbf{E}$. Coulomb collisions between electrons and ions limits the electrical current that can drive the electric field. In equilibrium, the current density is proportional to the electric field by $\mathbf{E} = \eta\mathbf{J} = -\eta n_e e\mathbf{v}$ (Ohm's law), with η the plasma resistivity. Substituting Ohm's law into the equation of motion of an electron in an electric field leads to $m_e \dfrac{\partial \mathbf{v}}{\partial t} = -e\mathbf{E} = \eta n_e e^2 \mathbf{v}$. To give a rough estimate of the resistivity, the time derivation can be reduced to $m_e \dfrac{\mathbf{v}}{\tau_{ei}} = \eta n_e e^2 \mathbf{v}$, with the collision time $\tau_{ei} = 1/\nu_{ei}$. This leads to

$$\eta = \frac{\pi Z^2 e^2}{(4\pi\epsilon_0)^2 m_e v_e^3} \ln\Lambda \tag{2.20}$$

Equation (2.20) gives the so-called Spitzer resistivity [47] in a fully ionized, unmagnetized, plasma (resistivity due to binary Coulomb collisions). Expression (2.20) shows that the resistivity is insensitive to the density because the number

density is included inside the expression $\ln\Lambda$. Using $v_e \sim \sqrt{k_B T_e/m_e}$, corresponding to the thermal electron velocity of a Maxwellian distribution, in expression (2.20) gives

$$\eta = \frac{\pi Z^2 e^2 m_e^{1/2}}{(4\pi\epsilon_0)^2 (k_B T_e)^{3/2}} \ln\Lambda \tag{2.21}$$

This shows that the resistivity scales with $T_e^{-3/2}$. As the temperature of the plasma increases the resistivity drops, therefore plasmas at very high temperature are, to a good approximation, collisionless. The Spitzer resistivity also $\to \infty$ when $T_e \to 0$ (i.e. very high collisions frequency). However, as example in Al, the experimental results of Milchberg *et al.* [48] show a linear increase in resistivity at low temperature, up to a peak value $\sim 2.2 \times 10^{-6}$ Ωm at $T_e \sim 50$ eV, and tends to Spitzer resistivity. The Lee-More model [49] limits the collision frequency, thus reducing the resistivity, at low temperature.

2.2 Picosecond Laser-plasma interaction

This section will now describe in more detail the interactions of an electromagnetic wave with a plasma. As a plasma is a charged medium, propagation of an electromagnetic wave within it generates a large number of linear and nonlinear phenomena. This section describes the main phenomena responsible for fast electron generation and acceleration in UHI laser-solid interaction.

2.2.1 Ionization processes of a single atom

When an UHI laser pulse irradiates a solid target, the matter up to the skin depth is rapidly ablated and ionized forming a surface plasma layer. Electrons are extracted from the atom and move under the Lorentz force associated with the laser field. Several mechanisms can be responsible for the ionization, as shown in figure 2.3. If the photon energy ($h\nu$) is less than the binding energy, an atom can be ionized by absorbing several of these photons. This process is called **Mul-**

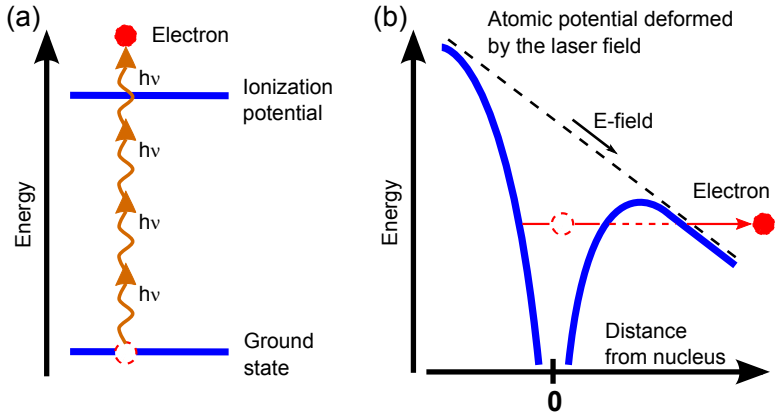

Figure 2.3: Ionization processes: (a)Multiphoton ionization; (b)Tunneling ionization.

tiphoton ionization [50, 51].

At high intensities, the laser field deforms the atomic potential so strongly that bound electrons can tunnel through the remaining potential barrier, this process is called **Tunneling ionization** [50–52]. The 'Ammosov, Delone, Krainov' (ADK) theory predicts the probability of tunnel ionization [53]. At very high intensities, the laser field amplitude can be higher than the field-ionization threshold of the atom, this process is called **Over the barrier ionization** by the electric field [52]. In this case, an electron is directly extracted from the atom and will oscillate in the wave. For example, the electric field strength to ionize the hydrogen such that over-the-barrier ionization just occurs is $E_h = 5.1 \times 10^{11}$ V/m. The field strength, corresponding to a laser intensity of 10^{18} W/cm^2, is $\sim 10^{12}$ V/m, higher than the ionization threshold value. Finally, free energetic electrons can ionize atoms via collisions with bound electrons, this process is called **Collisional ionization**.

2.2.2 Motion of a single electron in an electromagnetic plane wave

When light interacts with a charged particle, this particle moves in the electromagnetic (EM) field associated to the wave. A linearly polarized EM wave, propagating in the vacuum along the z-axis in the positive way, can be described

by:

$$\mathbf{E}(\mathbf{r},t) = E_0(\mathbf{r},t)e^{i(\omega_L t - kz)}\mathbf{x} \tag{2.22}$$

$$\mathbf{B}(\mathbf{r},t) = B_0(\mathbf{r},t)e^{i(\omega_L t - kz)}\mathbf{y} = \mathbf{z}\times\mathbf{E}/c \tag{2.23}$$

In the vaccum, $\mathbf{k}$ is the laser wave vector with a wavenumber equal to ω_L/c (in vacuum, the direction of $\mathbf{k}$ is the direction in which the plane wave is propagating), $\mathbf{r}$ is the position vector in 3D, $B_0(\mathbf{r},t)$ and $E_0(\mathbf{r},t)$ are the slow varying amplitudes of, respectively, the magnetic field $\mathbf{B}$ and the electric field $\mathbf{E}$, $\mathbf{x},\mathbf{y}$ are unit vectors both normal to the propagation direction $\mathbf{z}$. The motion of a single electron, with charge e, in presence of the EM wave is described by the Lorentz force

$$\frac{d(\gamma m_e \mathbf{v})}{dt} = \frac{d\mathbf{p}}{dt} = -e(\mathbf{E} + \mathbf{v}\times\mathbf{B}), \tag{2.24}$$

and the energy equation

$$\frac{d\gamma}{dt} = -\frac{e}{m_e c^2}(\mathbf{v}\cdot\mathbf{E}), \tag{2.25}$$

with $\mathbf{p} = \gamma m_e \mathbf{v}$ the particle momentum, m_e and $\mathbf{v}$ the electron mass and velocity. γ is the relativistic factor also called Lorentz factor

$$\gamma = \frac{1}{\sqrt{1 - v^2/c^2}} = \sqrt{1 + p^2/m_e^2 c^2} \tag{2.26}$$

The vector potential $\mathbf{A}$ is defined by $\mathbf{E} = -\partial\mathbf{A}/\partial t$. The normalized vector potential $\mathbf{a}$ is equal to $(e\mathbf{A}/(cm_e) = e\mathbf{E}/(cm_e\omega_L))$. The dimensionless quantity a_0, which is the peak of the normalized vector potential $\mathbf{a}$, is used to define the boundary between the non-relativistic and relativistic regime in a monochromatic EM wave. a_0 is given by

$$a_0 = \frac{eE_0}{cm_e\omega_L}. \tag{2.27}$$

a_0 is related to the laser intensity and wavelength, for linearly polarized laser pulse, via $a_0 = 0.85\sqrt{I_{L,18}\lambda_L[\mu m]^2}$, with $\mathrm{I}_{L,18}$ the laser intensity given in units of 10^{18} W/cm^2. For circular polarization, a_0 is divided by $\sqrt{2}$.

Under **non-relativistic** laser irradiation ($v \ll c$, i.e. $a_0 \ll 1$ and $\gamma = 1$), the effect of the magnetic field on the electron is neglected. Thus, the equation of motion reads

$$\frac{\partial \mathbf{v}}{\partial t} = -\frac{e}{m_e}\mathbf{E} \tag{2.28}$$

The linear solution of the equation of motion, taking the real part of the fields, is

$$\mathbf{v} = -eE_0\mathbf{x}\sin(\omega_L t - kz)/m_e\omega_L \tag{2.29}$$

Consequently, only the electric field acts on the charged particle, leading the electron to oscillate in the electric field direction (perpendicular to the propagation axis). The velocity amplitude (quiver velocity) is given by [1]

$$v_{osc} = ca_0 = eE_0/m_e\omega_L. \tag{2.30}$$

At **relativistic** laser irradiation, when v becomes comparable to c ($a_0 \geq 1$) [54], the magnetic component of the Lorentz force also has to be taken into account. The particle velocity is evaluated to second order

$$\mathbf{v} = \mathbf{v^{(1)}} + \mathbf{v^{(2)}}, \tag{2.31}$$

then, the term (2.31) is inserted into the equation of motion to identify the solutions at the first and second order of the velocity expansion

$$\frac{\partial \mathbf{v}^{(1)}}{\partial t} = -\frac{e}{m_e}\mathbf{E}, \quad \frac{\partial \mathbf{v}^{(2)}}{\partial t} = -e\frac{\mathbf{v}^{(1)}}{m_e} \times \mathbf{B}. \tag{2.32}$$

The lowest order $\mathbf{v^{(1)}}$ is the linear solution (2.29). Using $\mathbf{v^{(1)}}$, $\mathbf{v^{(2)}}$ is given by $\mathbf{v^{(2)}} = \mathbf{z}(-e^2E_0^2/4cm_e^2\omega_L^2)\cos(2(\omega_L t - kz)) = -\mathbf{z}(a_0^2 c/4)\cos(2(\omega_L t - kz))$.
The electron trajectory forming a 'figure-of-eight' (in the average rest frame), represented in figure 2.4, is then the superposition of the lowest order oscillation at ω_L along the x-axis and the second order oscillating at $2\omega_L$ along the propagation

[1] In the relativistic regime, the velocity amplitude is given by $v_{osc} = ca_0/\gamma$.

axis **z**. The EM wave can be represented by **A** which is transverse ($\perp$) to the

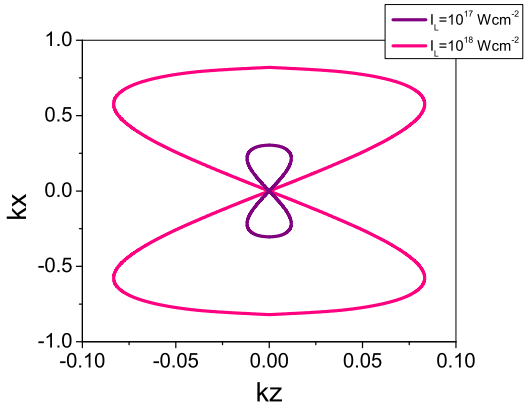

Figure 2.4: Figure-of-eight in the frame at rest (no average drift along the propagation axis), for different laser intensities.

propagation direction, therefore **E** and **B** are substituted by $\mathbf{E} = -\partial\mathbf{A}/\partial t$ and $\mathbf{B} = \nabla \times \mathbf{A}$ in the equation of motion 2.24. The transverse component of 2.24 gives

$$\frac{d\mathbf{p}_\perp}{dt} = e\frac{d\mathbf{A}_\perp}{dt}, \tag{2.33}$$

which after integrating gives the canonical momentum $\mathbf{p}_{\perp\mathbf{0}} \equiv \mathbf{p}_\perp - e\mathbf{A}_\perp$. For a linearly polarized wave, $p_{x0} \equiv p_x - eA_x$

The longitudinal components of 2.24 and 2.25 lead to

$$\frac{dp_{//}}{dt} = \frac{dp_z}{dt} = \frac{d(\gamma)}{dt}, \tag{2.34}$$

which after integrating gives $\gamma - p_x = \alpha$, where α is a constant of motion.

The electron, in addition to its transversal momentum, acquires a forward movement (along the propagation axis) independent of the EM wave polarization, due to the magnetic force. The longitudinal drift velocity of the electron can be approximated by $\mathbf{v}_D/c = [a_0^2/(4 + a_0^2)]\mathbf{z}$, assuming the electron is initially immobile ($\gamma = 1$).

Even though the electron oscillates in the fields of the plane wave and drifts along the propagation axis, after the laser has passed the net energy gained by the electron in an EM plane wave propagating in the vacuum is null (due to preservation of the canonical momentum, i.e. Lawson-Woodward theorem [55]).

The full derivation of, both non-relativistic and relativistic, electron motion in an EM plane wave propagating in the vacuum can be found in [56–58].

2.2.3 The Ponderomotive force

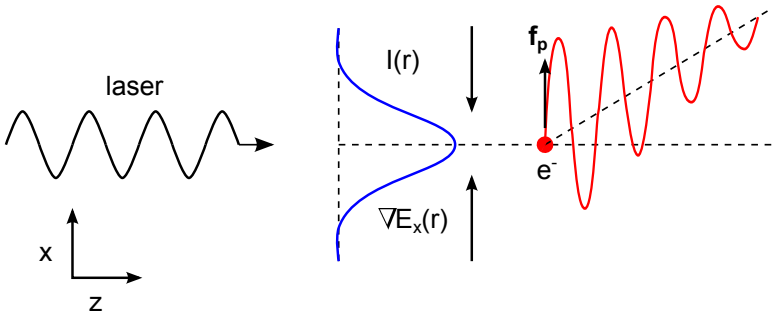

Figure 2.5: 1D cartoon representing the radial drift of the oscillating single electron in the wave field due to the laser intensity gradient.

A real laser pulse, far from being a plane wave, presents a strong transverse (radial) intensity gradient, especially when focused to few μm, and a longitudinal gradient due to its temporal profile. The laser EM wave propagating in a plasma, interacts with, and transfers momentum to, the plasma by means of the ponderomotive force (F_p). The derivation of the ponderomotive force is presented in this section.

Interaction with a single electron

At $v \ll c$ (the magnetic field is neglected) [57], the equation of motion for a single electron in a electromagnetic wave traveling in the z-direction is

$$\frac{\partial v_x}{\partial t} = -\frac{e}{m_e} E_x(r), \tag{2.35}$$

where $E_x(r)$ contains the spatial intensity dependence of the amplitude, which is in the x-direction only. $\Re(E_x(r))$ can be expanded into Taylor series as $E_x(r) \cong E_x^{(1)}(r) + E_x^{(2)}(r)... \cong E_0(x)cos(\omega_L t - kz) + x\frac{\partial E_0(x)}{\partial x}cos(\omega_L t - kz) + ...$ The

lowest order $E_x^{(1)}(r)$ of this expansion gives $v_x = -v_{osc}\sin(\omega_L t - kz)$, and $x = \frac{v_{osc}}{\omega_L}\cos(\omega_L t - kz)$, with the peak electron oscillation velocity $v_{osc} = eE_0/(m_e\omega_L)$ defined by equation (2.30). In lowest order, the electron simply oscillates around its current position due to the electric field.

In the second order approximation the calculation becomes nonlinear. By substituting x by $\dfrac{v_{osc}}{\omega_L}\cos(\omega_L t - kz)$ in the second order of the Taylor series expansion, the equation of motion becomes

$$\frac{\partial v_x}{\partial t} = -\frac{e^2}{m_e^2\omega_L^2}E_0(x)\frac{\partial E_0(x)}{\partial x}\cos^2(\omega_L t - kz) \tag{2.36}$$

The nonlinear force acting on the electron is then

$$F_{nl} = m_e\frac{\partial v_x}{\partial t} = -\frac{e^2}{2m_e\omega_L^2}\frac{\partial E_0^2(x)}{\partial x}\cos^2(\omega_L t - kz) \tag{2.37}$$

The non-relativistic ponderomotive force acting on the electron, is the average of F_{nl} over a laser period; this is

$$F_p = < m_e\frac{\partial v_x}{\partial t} > = -\frac{e^2}{4m_e\omega_L^2}\frac{\partial E_0^2(x)}{\partial x} = -\frac{\partial \Phi_p}{\partial x}, \tag{2.38}$$

with $\Phi_p = [(e^2/4m_e\omega_L^2)]E_0^2(x)$ the ponderomotive potential. The electron, because of the intensity gradient changing the value of $E_x(r)$, drifts away (i.e. are expelled) from regions where the intensity is higher as shown in figure 2.5, picking up a velocity equal to ($v \sim v_{osc}$).

The fields are expressed in term of the vector potential A in the equation of motion (2.24), using $\dfrac{dp}{dt} = \dfrac{\partial p}{\partial t} + \dfrac{\partial r}{\partial t}.\dfrac{\partial p}{\partial r} = \dfrac{\partial p}{\partial t} + v.\dfrac{\partial p}{\partial r}$,

$$\frac{\partial \mathbf{p}}{\partial t} + (v.\nabla)\mathbf{p} = e\frac{\partial \mathbf{A}}{\partial t} - e\mathbf{v}\times(\nabla\times\mathbf{A}). \tag{2.39}$$

The velocity associated with the ponderomotive force varies more slowly than the electron quiver velocity (i.e. slow variation of the laser envelope compared to phase). Thus, the timescales of the electron motion are separated into slow and fast components ($\mathbf{p} = \mathbf{p^s} + \mathbf{p}^f$), with the fast transverse component of the

electron momentum is $\mathbf{p}^f = e\mathbf{A}$. The relativistic ponderomotive force averaged over a laser period, derived in Gibbon [57], is given by

$$\mathbf{F_p} = \frac{d\mathbf{p}^s}{dt} = -m_e c^2 \nabla \langle\gamma\rangle, \tag{2.40}$$

where $\langle\gamma\rangle$ is the cycle-averaged relativistic factor derived in Mora *et al.* [59]. $\langle\gamma\rangle$ is equal to $\sqrt{1 + p_s/m_e^2c^2 + a_0^2/2}$ for a linearly polarized laser pulse and equal to $\sqrt{1 + p_s/m_e^2c^2 + a_0^2}$ for a circularly polarized laser pulse.
The final kinetic energy acquired by the electron is given by $\Delta U = (\langle\gamma\rangle - 1)m_e c^2$ [57]. This energy is extracted from the EM field via multiphoton momentum transfer. The fast electron are ejected in the vacuum from the laser beam focus at an angle [57, 60]

$$\tan\theta = \sqrt{\frac{2}{\gamma - 1}} \tag{2.41}$$

Interaction with a plasma

F_p also acts on ions (as F_p is proportional to the charge squared). However, its effect on ions is negligible as F_p scales with the inverse of the particle mass. Therfore, when the EM wave interacts with a plasma, the electrons of the plasma are pushed away (in the transverse and longitudinal direction) from regions of higher intensity to lower intensities because of the laser radial and temporal profiles.The acceleration is mainly due to the longitudinal electron oscillation at the vacuum plasma interface, that can be strong enough for the electron to escape this forced oscillation. Therefore, MeV electrons are accelerated towards the overdense plasma region every half-cycle ($F_p(2\omega_L)$). This acceleration mechanism is called J $\times$ B heating. The ponderomotive force can deform the target surface in mildly overdense plasmas up to $10\times n_c$ (hole boring) [61].

2.2.4 Dynamics of the laser- plasma interaction

Nowadays most of the UHI laser systems possess an UH laser pulse contrast ratio of the order of 10^{7-8} (without using plasma mirrors [62]). However, the edge of the laser pulse and the intensity of the remaining laser pedestal or of the prepulse arriving a few nanoseconds before the main pulse, can be high enough to generate a preplasma at the solid front surface. This intensity can reach 10^{13} W/cm^2 which is high enough to ionize atoms in the solid, leading to the formation of a preplasma at the target front surface. The density scale length of this preplasma, depending on the laser-plasma interaction condition, is a critical parameter that strongly affects the laser energy absorption mechanism and consequently the fast electron mean temperature and number, discussed in the next section and in chapter 7.

The surface plasma layer is created by field ionization. The laser light ionizes atoms and ablates the solid in the interaction region, creating the plasma. This plasma, containing electrons and ions, can be considered to be in thermal equilibrium for long laser pulses (nanoseconds).

Therefore, the main laser pulse interacts first with the preplasma expanding isothermally into the vacuum at the sound speed. The preplasma, with an exponentially decreasing form [44] (assuming a 1D expansion), can expand over a distance varying from ∼tens of nanometers to tens of mirons. The preplasma density scale length, L_n, is defined by

$$L_n = n_e \frac{dz}{dn_e} = c_s \tau_L, \tag{2.42}$$

for a plasma density $n_e \propto exp(-z/L_n)$, where dn_e/dz is the slope of the density at the density n_e [63], c_s the sound speed and τ_L the laser pulse duration. The sound speed is defined by

$$c_s = \sqrt{\frac{Z^* k_B T_e}{m_i}}, \tag{2.43}$$

with Z^* the effective ion charge and m_i the ion mass. The laser pulse propagates through this underdense plasma where its energy is partly absorbed and

transferred to the plasma electrons, until it reaches the critical density, where the plasma frequency is equal to the laser frequency, given by

$$n_c[cm^{-3}] = \frac{\epsilon_0 m_e}{e^2}\omega_L^2 = \frac{1.1 \times 10^{21}}{\lambda_L[\mu m]^2}, \tag{2.44}$$

with e the electron charge, m_e the electron mass. A part of the laser light can be absorbed and another reflected around the critical density. However, the laser wave propagates slightly beyond n_c as it becomes evanescent. The wave amplitude decreases exponentially over a distance called the collisionless skin depth equal to c/ω_{pe} in the non relativistic limit.

At high intensities ($\geq 10^{18}$ W/cm^2), nonlinear effects appear, as the electrons become relativistic and their mass is increased (γm_e) by the relativistic factor. The relativistic electron motion in the laser wave modifies the plasma frequency ω_{pe} and thus the refractive index and the critical density (γn_c). As an example, for a linearly polarized laser wave with $a_0 \gg 1$, γ becomes ($\cong a_0/\sqrt{2}$) and ω_{pe}, divided by $\sqrt{\gamma}$, is ($\propto \sqrt{n_e/a_0}$) and therefore the laser light can propagates deeper into the overdense plasma (self-induced transparency [57, 64]). Because of the change in the refractive index with a maximum on the beam axis the laser wave front is curved, causing the convergence of the beam on axis. Therefore, the laser beam remains focused over a distance longer than the Rayleigh length while propagating in underdense plasma (relativistic self-focusing [65]). In addition, the ponderomotive force, expelling the electrons away from the region of high laser intensity, increases the refractive index on the beam axis and leads to the ponderomotive self-focusing of the laser beam [66].

The mechanisms for absorption of laser energy, leading to fast electron acceleration are described in the next section.

2.3 Laser energy absorption mechanisms and fast electron generation

Several laser energy absorption mechanisms can operate simultaneously when a laser pulse interacts with a plasma. Those mechanisms occur according to the interaction conditions characterized by the laser parameters and the preplasma density gradient. Those absorption mechanisms are described in this section.
Note that when the temperature T is in unit of energy [eV], this means $T[eV] = k_B[eV/K]T[K]$.

2.3.1 Collisional absorption

Collisional absorption dominates at low laser intensities ($I_L < 10^{15}$ W.cm^{-2}). Electrons oscillating in the laser electric field absorb part of the laser energy, via **Inverse bremsstrahlung** . By colliding with plasma ions, the electrons lose their coherence in the wave and can leave the interaction zone with a non-zero momentum. The absorption rate can be found in Rozmus *et al.* [67].
As the intensity of the laser increases, the plasma is heated in the interaction region to a temperature up to 100s of eV. The Spitzer collision frequency [47], proportional to $T_e^{-3/2}$, is then reduced and thus collisional processes decrease. The increasing electron oscillation velocity is added to the thermal velocity, reducing the collision frequency further [68]. Collisional coupling becomes negligible.

2.3.2 Collisionless absorption

There is a number of collisionless processes, such as **resonance absorption** and **vacuum heating** occurring at 'moderate' laser intensity and for p-polarized laser wave incident obliquely on the plasma. **Ponderomotive heating** occurs at any linear polarization and for laser intensity higher than 10^{18} W.cm^{-2}. The energy coupling is more efficient at normal incidence and involves nonlinear processes.

Those processes are described in this section.

Resonance absorption

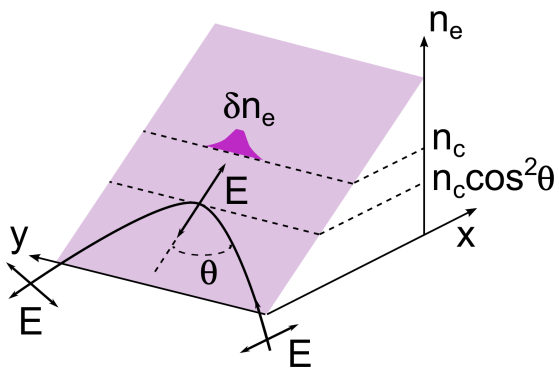

Figure 2.6: Cartoon representing Resonant absorption in an overdense plasma: the p-polarized wave, obliquely incident on the critical surface, is reflected at the density $n_c cos^2(\theta)$. δn_e electrons of the resonant electron plasma wave are accelerated at n_c into the overdense plasma.

Resonance absorption occurs for a p-polarized laser wave interacting, at an oblique angle θ with the target, so that the electric field (perpendicular to the k vector) points into the overdense plasma. The energy coupling process is also more efficient for a plasma density scalelength $L_n >> \lambda_L$. The electric field component normal to the density gradient resonantly excites a longitudinal electron plasma wave at the laser frequency at a surface of critical density. The laser propagates to a density equal to $(n_c \cos^2 \theta)$ and is reflected. The electrons in the plasma wave are accelerated into the overdense plasma to high energies mainly via wave breaking (the electron acceleration is hence normal to the target surface). The propagation equation of the laser has been numerically solved by Ginzburg [69]. It shows that absorption of 50% is achieved for an angle $\theta_{max} = \arcsin[0.8[\lambda_L/2\pi L_{n,L}]^{1/3}]$. Forslund *et al.* [70] derived the fast electron temperature (T_f) as

$$T_f[keV] \sim 10[T_e[keV] I_{L,16} \lambda_L[\mu m]^2]^{1/3}, \tag{2.45}$$

with $I_{L,16}$ the laser intensity given in units of 10^{16} W/cm^2 (T_e is the background electron temperature).

Vacuum heating (Brunel effect)

Vacuum heating [71] is similar to resonance absorption, except that it occurs in steep density gradient plasma. The electrons are directly heated by the laser field. They are extracted from the target, normally to its surface, towards the vacuum, by the longitudinal component of the electric field during the laser first half cycle. The electrons are re-injected into the overdense plasma region during the second half of the laser cycle. Bunches of electrons are produced at the laser frequency, carrying the energy acquired in the longitudinal oscillation. The average kinetic energy of the hot electrons, for $L_n/\lambda_L < 0.1$ and $I_L \sim 10^{14-18}$ W/cm^2, is proportional to $\propto [I_L \lambda_L [\mu m]^2]^\alpha$ [72], with α between 1/2 and 1/3.

J×B heating

Both previous collisionless coupling mechanisms are driven by the electric field in the Lorentz force (at frequency ω_L), thus they require p-polarization and oblique incidence so that the electric field in the plane of incidence has a component toward the overdense plasma surface. For high intensities nonlinear oscillations can be driven by the longitudinal v×B force (at a frequency $2\omega_L$) [73]. J×B heating is similar to vacuum heating as the electron are directly accelerated by the laser field, along the laser axis direction, at the critical density. J×B heating occurs for any linear polarization of the laser light and is most efficient at normal incidence. The longitudinal oscillating force ($\mathbf{v} \times \mathbf{B}$) vanishes for circular polarization and at normal incidence. This coupling mechanism has been experimentally verified by Malka *et al* [74].

The temperature of the fast electrons generated through the J×B mechanism is proportional to the ponderomotive potential [63]:

$$T_f[keV] = 511 \times [\sqrt{\frac{1 + I_{L,18}\lambda_L[\mu m]^2}{2 \times 1.37}} - 1], \tag{2.46}$$

for linearly polarized laser pulse, with $I_{L,18}$ the laser intensity given in units of 10^{18} W/cm^2.

2.3.3 Parametric absorption

Amplified spontaneous emission leads to the formation of a laser pedestal or prepulse that can contain enough energy to ionize the target before the main pulse arrives creating a plasma of few tenths of micrometers in length. The laser pulse interacts with a large subcritical plasma via non-linear mechanisms. The light wave, in the case of Raman instabilities, is coupled into scattered light and an electron plasma wave. Energetic electrons are produced via wave breaking of the large amplitude electron plasma wave.

2.4 Properties of the laser-generated fast electron beam

Laser-generated relativistic electron beams in a solid are being intensely investigated both experimentally and theoretically. The difficulty in experimentally measuring the fast electron parameters, such as the source density, energy distribution, injection angle, beam current density and divergence angle while propagating in the solid, comes from the indirect experimental techniques available to probe the beam inside the solid. Several suggested form for the fast electron energy and angular distributions can be found in the literature. The energy distribution can be inferred from numerical simulations or experimentally from the secondary X-ray emission spectrum or the TNSA-generated proton spectrum proportional to the fast electron spectrum. An exponential decay or a Maxwellian distribution are often used with a mean temperature scaling with the laser intensity, as discussed in the previous section.

The mean temperature, for laser irradiance higher than 10^{18} W/cm^2, depends on the ponderomotive potential and therefore scales as $\sim \sqrt{I_L \lambda^2}$ [43, 63]. How-

ever, for example, Beg *et al.* [75–77] experimentally inferred that the temperature scales as $\sim (I_L\lambda^2)^{1/3}$. For this experimental study, targets were irradiated at 30° compared to the target normal with laser intensities from $\sim 10^{17}$ to 10^{19} W/cm^2 and p-polarized light. The results of Beg [75] has attributed this temperature scaling to resonance absorption rather than to $J \times B$ heating due to the radiation pressure that can be high enough to balance the plasma expansion and thus induces a steepening of the density profile.

Beg results [75] and the work of [18, 42, 43, 78–85] highlight the importance of the laser- preplasma/solid interaction conditions in changing the fast electron acceleration mechanism and the laser-to-electron conversion efficiency. The conversion efficiency η_{L-e} can be experimentally inferred from the K-shell yield measurement [42, 43, 85] and numerically from PIC simulations. Nilson *et al.* [42, 43, 85] found a fixed $\eta_{L-e} = 0.2$ over a wide range of laser intensity. Davies *et al.* [84], by fitting experimental data, found that η_{L-e} scales with the laser intensity and increases with increasing intensity ($\eta_{L-e} \sim 0.5$ for $I_L \sim 10^{20}$ W/cm^2). The variation of laser-to-electron conversion efficiency with the laser parameters is discussed in chapter 7. The number of electrons generated during the interaction, within a laser spot volume of $\pi r_L^2 c\tau_L$, can be approximated by an energy balance relation $(\eta_{L-e}E_L)/(T_f[eV])$ [25], with r_L the laser spot radius, τ_L the laser pulse duration, E_L the laser pulse energy. Moore *et al.* [60] experimentally demonstrated the angular-energy distribution of equation (2.41) (ejection towards the vacuum). Sheng *et al.* [86] derived the angular-energy injection distribution in solids, at a specific angle of incidence of the laser pulse. Another scaling of the electron energy and angular distribution function was derived by Sherlock [87], based on 1D Vlasov-Fokker-Planck simulations of laser-plasma interactions for a laser intensity range of 10^{19}-2×10^{20} W.cm^2.

2D/3D PIC simulations of Adam *et al.* [21] show an initial divergence half-angle of the fast electron beam (20°-40°), for laser intensities varying from 10^{18} to 10^{21} W.cm^{-2} interacting with a sharp density gradient (up to $160\times n_c$). This is due to the development of filaments produced as a result of the Weibel instability.

The recent PIC simulations of Ovchinnikov *et al.* [20] show that the fast-electron

divergence angle increases almost linearly with the preplasma scale length for a fixed laser intensity. For a fixed preplasma scale length, the laser intensity affects little the divergence angle in the range between 10^{18}-10^{21} W/cm^2.

Experimental measurements of the divergence angle at a given depth in the solid [14, 15], based on the X-ray emission of a fluorescent layer inserted in the solid, gave a value ranging between $\sim 30^\circ - 55^\circ$. The angle increases with I_L.

Chapter 3

Transport of fast electrons in a solid

Electron beams of energy up to a few tens of MeV, generated during laser-plasma interaction around the critical density, can propagate through 100s of μm-thick overdense plasma. A limit for the current that can, in principle, be transported in vacuum was given by Alfvèn [88]. In a plasma, the Alfvèn limit is exceeded as the beam is neutralized by a cold return current of the same magnitude, with a larger number of slow electrons.

Propagation of a beam of charged particles in a solid involves several interlinked mechanisms, related to the background plasma and to the fast electron distribution function. This chapter describes the collisional and collective transport of electrons in overdense plasma, including the production of secondary radiation and ion acceleration at the solid boundaries.

3.1 Collisional transport of fast electrons

While propagating in a solid, incident fast electrons collide *via* elastic or inelastic collisions with ions, bound electrons and free electrons of the background plasma. Inelastic collisions with bound electrons are the principal cause for energy loss.

The fast electron transfers part of its kinetic energy to the bound electron in the form of excitation, ionization or loses energy via Bremsstrahlung. Elastic collisions with ions of the background lead to angular diffusion of the electron beam with almost no energy loss due to the particles mass ratio [89]. Figure 3.1 presents the different interaction processes.

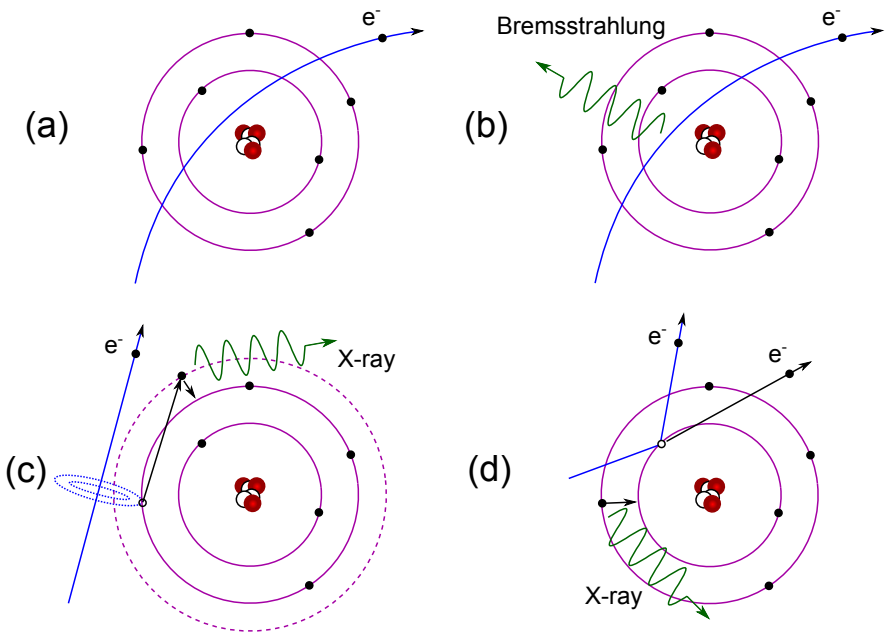

Figure 3.1: (a) Elastic collision; (b) Bremsstrahlung; (c) Inelastic collision: excitation; (d) Inelastic collision: ionization.

3.1.1 Fast electron angular scattering

As mentioned above, elastic collision of fast electrons with background ions leaves the ion in the same ionization state and the electron with almost no kinetic energy loss. However, the electron is deflected. Globally, elastic collisions lead to the angular broadening of the electron beam. Due to the long range of the Coulomb force, the collisions are predominantly small angle scattering events. The multiple scattering at small angles can be described, in first approximation, by the classical Rutherford differential scattering cross section which is function of the deflection angle θ: $\frac{d\sigma_R}{d\Omega} = \frac{4Z^2e^4}{(4\pi\epsilon_0 m_e c^2)^2\beta^4}\frac{1}{(4sin^2\theta/2)^2}$, with $\beta = v/c$, Ω the solid

angle function of θ. The expression of the Rutherford cross section shows that the angular diffusion will be important in high Z material and for low energy electron. Note that the cross section tends to infinity for $\theta \to 0$ due to the infinite range of potential, which can be solved by taking into account the screened Coulomb potential.

The scattering distribution function (small angles and multiple scattering) is well represented by Molière's theory, later corrected by Nigam *et al* [90–92]. The distribution is roughly Gaussian for small angles, and reproduces the Rutherford scattering for larger angles. The half-width of the distribution function is mainly dependent on the atomic number Z, the degree of ionization Z^*, the relativistic factor, β and the plasma density. The mean deflection angle $< \theta >$ increases with increasing plasma density, thickness and decreases with increasing incident electron energies.

3.1.2 Collisional and radiative collisional stopping power

Electrons lose energy in matter by, at 'low' electron energies, primarily ionization or excitation of background ions, while radiation emission by bremsstrahlung (interaction with nuclei) dominates for electron energies above a few tens of MeV in most materials.

The energy loss of electron while propagating in a solid is represented by the stopping power discussed in the next subsection.

Stopping power

The total stopping power $S(E)_t = -\dfrac{dE}{ds}$ is the rate of kinetic energy loss (dE) per unit path length (ds). $S(E)_t$ is the sum of both the ionization-excitation stopping power $S(E)_i$ and the radiative stopping power $S(E)_r$. The latter becomes important for MeV electrons and high Z material.

As example, the total stopping power of electrons in Al, Cu and Au, obtained from the data base Estar [93], are shown in figure 3.2.

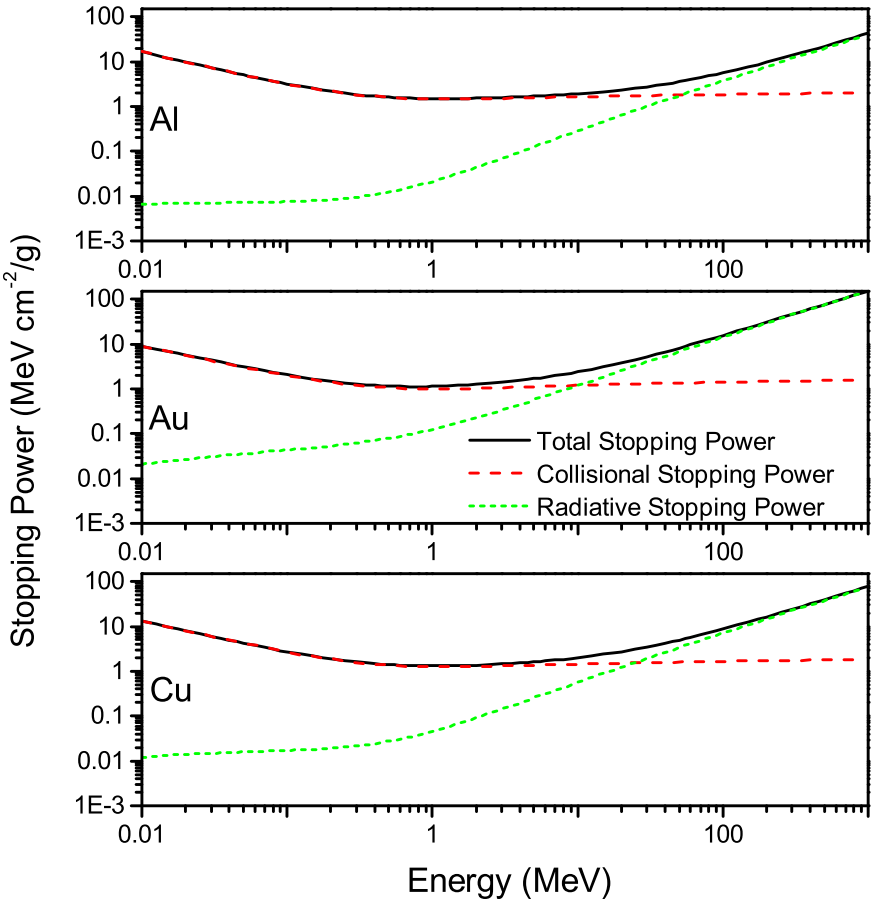

Figure 3.2: Total stopping power of electrons in Al, Au, Cu, obtained from the data base Estar [93], as function of the electron incident energy.

In a cold plasma, the interactions with free electrons are neglected and the stopping power can be 'split' in two terms depending on the incident electron kinetic energy:

→ If ΔE, the energy transferred by an incident electron to electrons in the solid, is higher than the electron binding energy, the bound electron becomes free. The stopping power is derived using the Møller cross section [94].

→ If ΔE is lower than the electron binding energy, the electron remains bound and its atomic transitions need to be evaluated. The stopping power is derived in [95] using Bethe's relativistic formula [96], coupled with the material average ionization potential, using the empirical formula of Sternheimer *et al.* [97]. The latter, given by $I_p[eV] \sim 9.76Z + 58.8Z^{-0.19}$, depends on the atomic number Z.

The sum of both stopping powers for free and bound electrons gives the collisional stopping power of electrons in a cold, moderately dense plasma [98]. Corrections to the stopping power calculated from Bethe's theory includes, for example, the 'density correction' δ [99]. The density effect reduces the energy loss by partially suppressing the relativistic rise of $S(E)$.

$$S(E)_i = -n_i 2\pi r_e^2 m_e c^2 \frac{Z}{\beta^2}\left[\ln\left(\frac{(\gamma+1)E^2}{2I_p^2}\right) + \frac{1-(2\gamma-1)\ln 2 + (\gamma-1)^2/8}{\gamma^2} - \delta\right], \tag{3.1}$$

with r_e the classical electron radius.

In a hot plasma characterized by its ionization state Z^*, in addition to collisions with bound electrons, the electron undergoes collisions with free electrons and plasmons (i.e. quasiparticles resulting from the quantization of the plasma oscillations).

Z^* modifies the average ionization potential. Based on the semi-empirical formula of More [100] $I_{p,Z^*} = 10eV \times Z\frac{\exp\left(1.29(Z^*/Z)^{0.72-0.18Z^*/Z}\right)}{\sqrt{1+Z^*/Z}}$. The stopping power associated with electron- bound electron collisions is given by Bethe formula (3.1), without the density correction δ and substituting I_p by I_{p,Z^*} and Z by $Z - Z^*$ The stopping power associated with electron- free electron collisions derived in

[101, 102] reads

$$S(E)_{i,e} = -n_i 2\pi r_e^2 m_e c^2 \frac{Z^*}{\beta^2}\left[\ln\left(\frac{(\gamma-1)m_e^2c^2\lambda_D^2}{2\hbar^2}\right)+1-\frac{(2\gamma-1)\ln 2}{\gamma^2}+\frac{(\gamma-1)^2}{8\gamma^2}\right], \tag{3.2}$$

with $\hbar = h/2\pi$ the reduced Planck constant. And the stopping power due to excitation of plasmons is given by [103].

$$S(E)_{i,p} = -n_i 2\pi r_e^2 m_e c^2 \frac{Z^*}{\beta^2}\ln\left[\frac{\beta^2c^2}{\omega_p^2\lambda_D^2}\right]. \tag{3.3}$$

The total collisional stopping power in an ionized plasma is then the sum of the three stopping powers. The collisional stopping power varies slightly with increasing background electron temperature. However, for moderately ionized plasma (i.e. low background electron temperature), energy losses are mainly due to electron-bound electron collisions and at higher plasma electrons temperature, they are predominantly due to electron-free electron collisions.

In addition to energy losses via collisions, **radiation losses** (bremsstrahlung) [104] due to deceleration of the incident electron when deflected by the nuclei, have to be considered at incident energies of tens of MeV and in high material density. $S(E)_r$ scales with the incident electron energies and Z^2, and also contributes to the total stopping power, for example in high density material such as Pb [105]. A 'critical energy' E_c, corresponding to $S(E_c)_r = S(E_c)_i$ can be approximated in a solid using $E_c = \frac{610MeV}{Z+1.24}$. As example, in Cu E_c ~20 MeV, in Al $E_c \sim 42$ MeV and in Au $E_c \sim 7$ MeV.

The stopping power gives an estimate of the continuous slowing down approximation (CSDA) range R, which is the distance it takes to slow down an electron with initial kinetic energy E_1 to rest. The calculation assumes that the electron slows down continuously from the initial to the final energy
$R = \int_{E_1}^{0} (\frac{dE}{ds})^{-1} dE$ [106].

3.2 High-current fast electron beam transport in the solid

A fast electron beam propagating in matter experiences, along with the collisional processes, collective effects due to the self-generated fields in the matter. As example, at laser intensity of the order of 10^{19} W.cm^{-2}, 10^{14} electrons can be produced, with energies ranging from 250 keV to 1 MeV and beam density of the order of 10^{19} cm^{-3}. The propagation of such a beam, with a very high current density $\sim kA/\mu m^2$, is possible if its current is neutralized. The current propagation and the perturbation of the background neutrality leads to self-generated fields that act on the beam propagation.

3.2.1 Beam transport in cold plasma beyond the Alfven limit : Charge neutrality and return current of thermal electrons

The propagation of an electron beam, with density of the order of 10^{21} cm^{-3}, in few orders of magnitude higher matter with electron density (10^{23} cm^{-3}), should be limited by the Coulomb explosion (the beam would explode without the surrounding matter). However, the localized excess of negative charges generates an electric field. This excess is neutralized as the thermal electrons are pushed out of the incoming fast electron beam by the electric field, thus enabling the beam propagation. The charge equilibrium is achieved in a time equal to $\sim 1/\omega_{pe}$ in a collisionless medium and $\sim 1/\sigma \sim \nu_{ei}/\omega_{pe}^2$ in a collisional medium, with σ the medium conductivity.

The current that can propagate in a solid is limited by the self-generated magnetic field that tends to pinch the beam and can reverse the course of the outer electrons in the beam. The maximum current that can travel in vacuum is given by the Alfvèn limit $I_A[A] = \frac{\beta\gamma mc^3}{e} \sim 1.7.10^4\beta\gamma$, with β and γ the velocity normalized to c and the Lorentz factor of the fast electron beam respectively. A

current exceeding this limit is stopped. This limit means that a current larger than I_A generates a magnetic field large enough that the Larmor radius (r_g) of the electrons becomes smaller than the beam radius.

The fast electron current ($\sim MA$) can propagate in a solid, beyond the Alfvèn limit, due to the 'return current'. The return current maintains the total current value below the Alfvèn limit. This return current originates from the 'axial electrostatic field' E_{emf} (Faraday's law) induced by the temporal variation of the self-generated azimuthal magnetic field. E_{emf} prevents the B-field growth by generating a 'return' or 'cold' counter propagating current. However, the fast electron beam radius, r_f, has to be bigger than the magnetic skin depth of the plasma $\lambda_e \sim c/\omega_{pe}$, the distance over which the magnetic field expands, in order to obtain an efficient neutralization of the current. The conductivity σ of the propagation medium also affects the current neutralization, as the collisions in the solid lead to a diffuse return current and thus magnetic diffusion. Therefore, an efficient beam neutralization takes place during a limited time of the order of the magnetic diffusion time, given by $\tau_d = [\mu_0 r_f^2 \sigma]$. For the experimental studies presented in this manuscript, $\tau_d \sim$10s of ps (longer than the beam duration $\sim$1 ps).

3.2.2 Self-generated fields

The fast electron beam can propagate in the solid beyond the Alfvèn limit due to current neutralization (i.e. cancellation of the local magnetic field). However, even with quasi perfect current neutralization resistive fields appear in the solid. The magnetic collimation of fast electron beams has been widely investigated numerically and experimentally [23–25, 107–114].

Suppose perfect current neutralization($J_f = J_b$), using Ohm's laws

$$\mathbf{E} = -\eta \mathbf{J_f} = \eta \mathbf{J_b}, \tag{3.4}$$

with $\mathbf{J_b}$, $\mathbf{J_f}$ the thermal and fast electron current density respectively, and Maxwell-Faraday's equation

$$\frac{\partial \mathbf{B}}{\partial t} = -\nabla \times \mathbf{E} = \nabla \times (\eta \mathbf{J_f}) = (\nabla \eta) \times \mathbf{J_f} + \eta(\nabla \times \mathbf{J_f}), \tag{3.5}$$

Davies *et al.* [115] derive simple expressions linking the electric and magnetic fields to the laser parameters (assuming a Gaussian laser pulse profile) and the background resistivity

$$E_{max}[V/m] \sim 6{\times}10^{9}\left[\left(\frac{\eta}{2\times10^{-6}[\Omega m]}\right)\left(\frac{\eta_{L-e}}{0.3}\right)\left(\frac{I_L}{10^{17}[W/cm^2]}\right)^{2/3}\left(\frac{1[\mu m]}{\lambda_L}\right)^{2/3}\right], \tag{3.6}$$

and

$$B_{max}[T] \sim 230\left[\left(\frac{\eta}{2\times10^{-6}[\Omega m]}\right)\left(\frac{2\tau_L}{1[ps]}\right)\left(\frac{10[\mu m]}{r_f}\right)\left(\frac{\eta_{L-e}}{0.3}\right)\left(\frac{I_L}{10^{17}[W/cm^2]}\right)^{2/3}\left(\frac{1[\mu m]}{\lambda_L}\right)^{2/3}\right] \tag{3.7}$$

Those expressions make it feasible to infer the threshold I_L below which the fast electron beam transport is more likely collisional [115]. Davies *et al.* [115] conclude that noncollisional effects are most important at high intensities. Furthermore, the magnetic field is higher in calculations with tighter focal spots and longer pulses.

From equation (3.5), the term $((\nabla\eta) \times \mathbf{J_f})$ implies that the spatial variation of the background resistivity affects the magnetic field [76, 108, 109], i.e. the fast electrons are pushed toward high resistivity regions of the plasma. Whereas, the term $(\eta(\nabla \times \mathbf{J_f}))$ pushes the electrons to higher J_f and focuses the beam. Finally, as the fast electrons propagating on axis can rapidly heat the plasma to high temperature, the resistivity, scaling as $T_b^{-3/2}$, is then reduced on axis and the beam forms an annular pattern.

3.2.3 Background plasma heating

Part of the fast electron beam kinetic energy is transferred to the return beam via the self-generated fields. The return current, in turn, transfers part of its energy *via* Ohmic heating to the background plasma. The Ohmic heating can be approximated using a simple model [116, 117], assuming that part of the energy lost by J_f is transfered to the background plasma via resistive heating associated to J_b, and the rest to the magnetic field.

Using Poynting's theorem (energy conservation for the electromagnetic field), the rate of energy transfer per unit length can be obtained by time integration of the power lost by the fast electron beam to the E-field ($\mathbf{J_f} \cdot \mathbf{E}$). For a Gaussian beam profile, the kinetic energy lost by the fast electron beam per unit length is given by

$$W_f(t) = \frac{I_f^2}{4\pi\epsilon_0 c^2} \ln\left(1 + 2\frac{t}{\tau_d}\right), \tag{3.8}$$

with $I_f = e\pi r_f^2 n_f v_f$ the total current of the fast electron beam and n_f, v_f the fast electron beam density and velocity respectively. The beam, after 1 ps, typically loses tens of mJ per μm.

The Ohmic heating of the background plasma per unit length is obtained by time integration of $\mathbf{J_b} \cdot \mathbf{E} = \eta J_b^2$

$$W_b(t) = \frac{1}{2}\frac{I_f^2}{4\pi\epsilon_0 c^2} \ln\left(1 + 4\frac{t}{\tau_d}\right) \tag{3.9}$$

The background plasma temperature (in pratical units) can be deduced by using a perfect gas model [117]

$$T_b[eV] \approx 400\beta^2 \left(\frac{Z^* n_i}{6.10^{22}[cm^{-3}]}\right)^{-1} \left(\frac{n_f}{10^{20}[cm^{-3}]}\right) \left(\frac{\eta}{10^{-6}[\Omega m]}\right) \left(\frac{t}{500[fs]}\right), \tag{3.10}$$

with β the velocity of the fast electron beam normalized to c. The ionization state Z^*, as a function of the temperature, can be approximated using More's formula [100] based on the Thomas-Fermi's theory.

A rough estimate of the collisional heating (for a cold plasma and neglecting the

density correction) can be obtained by multiplying the collisional stopping power of equation (3.1) with the number of fast electrons, in a duration t, equal to $(n_f \pi r_f^2 v_f t)$.
The ratio of collisional heating and Ohmic heating, for the typical experimental parameters of this work (in Al targets), shows that heating of the target is mainly due to the return current, thus of Ohmic origin [117].

3.2.4 Fast electron recirculation

After escaping the dense plasma, while the electrons propagate into the vacuum region strong self-generated electrostatic fields, due to charge separation, slow them down and pull the 'low energy' electrons back into the target [43, 118–120], where they recirculate. The fast electrons reaching the front boundary can also be reinjected into the solid where they recirculate until they lose their energy. The fast electrons can make multiple round-trips of the target, depending on their initial velocity and the target thickness and density, as their collisional range can be several hundred microns at solid density. Note that if the electrons are still collimated within the laser focal spot at the front surface, they can be reaccelerated in the solid by the laser pulse (if the laser pulse is still present). Finally, only a small fraction of the fast electron beam (few%) [43, 121], with energies > few MeV, escapes the sheath potential.
Fast electron recirculation, depending on the target thickness and volume, can modify the fast electron beam distribution, heat the background plasma to 100s of eV for mass limited targets [41, 85] and enhance the maximum proton energy in thin foils [122].

3.3 Beam- plasma instabilities

In the previous section, a perfect current neutralization is assumed and the self-induced fields act little on the electron distribution. However, various microscopic

(within the fast electron beam) and macroscopic (on a scale of the order of the beam radius or larger) instabilities can occur while the beam propagates in the plasma, altering the fast electron beam distribution. Some of them are described in this section.

3.3.1 Microscopic instabilities

Microscopic instabilities originate from the inter-penetration of two counter streaming beams. This gives place to a longitudinal and transverse velocity dispersion that turns into instabilities. The importance of any type of instability is defined by its growth rate. The growth rate of microscopic instabilities is proportional to the beam or background electron plasma frequency.

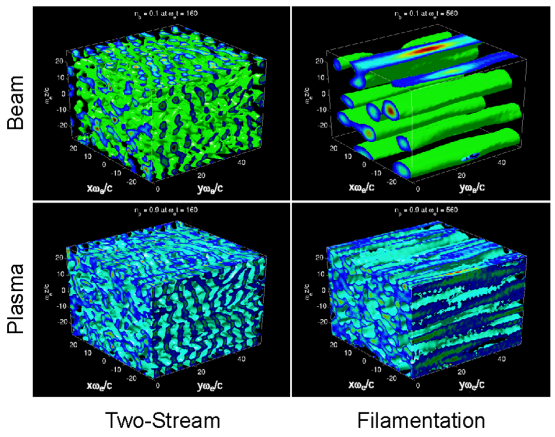

Figure 3.3: 3D PIC simulation copied from Bret *et al.* [123]. The figure presents isosurfaces of the fast electron beam and the background at $\omega_{pe}t$=160 (two-stream instability) and $\omega_{pe}t$=560 (filamentation instability). The run is made at a density ratio (fast electrons (f) and background plasma (b)) n_f/n_b=0.1, γ_f=3, k_BT_f=50 keV and k_BT_b=5 keV.

The **two-stream instability** [124] is of electrostatic longitudinal nature with a wave vector (**k**) parallel to the beam. The two-stream instability, shown in figure 3.3, can be suppressed in a highly collisional plasma. It can be induced by an

energetic beam injected in a plasma, exciting a plasma wave. The plasma wave has a lower velocity, so this difference in the velocities tends to slow down the electron beam. This instability can lead to an important energy transfer between the fast electron beam and the background plasma.

The electromagnetic filamentation instability or **Weibel instability** [125], associated with a non collisional, hot or moderately dense plasma, is mostly electromagnetic and transverse, i.e. $\mathbf{k}$ is normal to the beam. It originates from the magnetic repulsion between the counter-propagating beams that perturbs the magnetic fields, then leads to a break up of the beam currents into filaments. Consider homogeneous current which is neutralized by a counter propagating one. Due to a small perturbation of its density profile and hence of the magnetic field, the plasma return current will not fully neutralize the perturbed magnetic field. Consequently, micro-currents (filaments) are generated with a typical size of skin depth $\sim c/\omega_{pe}$ ($\sim 1.6 \times 10^{-3}$ μm for a typical solid density of 10^{23} cm^{-3}), surrounded by an azimuthal magnetic field that will further pinch each filament, carrying at maximum about the Alfvèn limit current[126]. The micro-currents and magnetic fields develop until saturation and if there are neighboring co-propagating filaments their like currents attract and they tend to coalesce. Therefore, the number of filaments decreases with propagation distance. Because the coalescence of two Alfvèn current carrying filaments produces a filament that can't exceed the Alfvèn limit, the excess energy contained in the original filaments is transferred to the background, which is heated [127]. The Weibel instability does not affect significantly the macroscopic beam transport inside the solid, however 2D/3D PIC simulations by Adam *et al.* [21] show that the initial divergence of the fast electron beam (20°-40°), for laser intensities varying from 10^{18} to 10^{21} W.cm^{-2}, interacting with a sharp density gradient, is due to the development of very thin and very intense filaments.

While the Weibel instability is associated with a collisionless background plasma, **Resistive filaments** [22, 128], which are dominant at high densities, are driven by the magnetic field associated with $(\nabla\eta) \times \mathbf{J_f}$. Disregarding the displacement current, the return current can be expressed from Ohm's law taking into account

the magnetic diffusion

$$\frac{\partial \mathbf{B}}{\partial t} + \frac{1}{\mu_0}\nabla \times (\eta \nabla \times \mathbf{B}) = \nabla \times (\eta \mathbf{J_f}) \tag{3.11}$$

$$\mathbf{E} = \eta \mathbf{J_b} = \eta(\frac{1}{\mu_0}\nabla \times \mathbf{B} - \mathbf{J_f}) \tag{3.12}$$

As for the Weibel instability, it originates from the magnetic repulsion of counter-propagating electron currents. The typical time of B-field generation within a micro-current of radius a is of the order of the magnetic diffusion time $\mu_0 a^2/\eta$. The filaments are ∼2-5 μm wide, with a total current per filament close to the Alfvén limit. Gremillet [117] also demonstrated that the growth rate increases with the resistivity, increasing the magnetic field strength. However, the growth rate saturates more quickly as the magnetic diffusion time decreases with increasing resistivity.

3.3.2 Macroscopic instabilities

The limited conductivity of the background plasma generates instabilities that develop on the scale of the fast electron beam radius. The growth time of the macroscopic instabilities is comparable to the magnetic diffusion time (∼ ps), much slower than the microscopic mechanisms.

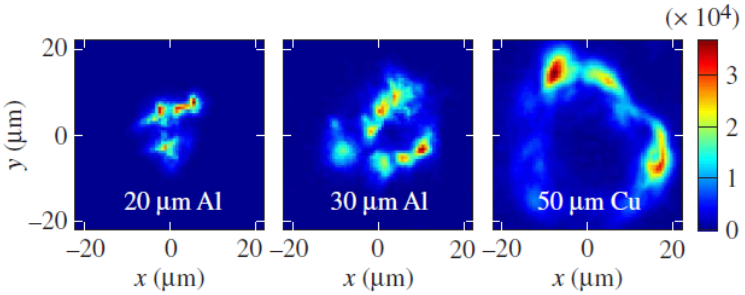

Figure 3.4: Images of the CTR emission spatial distribution copied from Storm *et al.* [17]. The images show the target's rear surface emission. An annular structure can be seen for the 50 μm-thick Cu target.

The **Hollowing instability** [76, 108, 109, 117] reduces the fast electron beam current to a minimum value on-axis. Consider a fast electron beam injected in a plasma; the finite conductivity of the background plasma results in a non-zero total current, which focuses the fast electron beam on-axis. The peak on-axis density leads to localized on-axis plasma heating. The plasma resistivity, scaling with $T_e^{-3/2}$, is then reduced on-axis, leading to an on-axis return current density peak. Mutual repulsion of forward and counter propagating current leads the electron beam to hollow (forming an annular pattern) as it propagates [17], as shown in figure 3.4.

A transverse motion of the fast electron beam should be balanced by the restoring force of the magnetic field. Thus, the beam oscillates around its initial propagation axis before stabilization. Due to the finite conductivity of the background plasma, the return current is then diffused, preventing the beam stabilization (**Hosing instability**) [117, 129].

The **ionization instability** [130, 131] occurs when the fast electron beam propagates in a dielectric target, where the field ionization by the fast electron beam generates free electrons which can step up the neutralization current. The strong electric field is due to the charge separation at the edge of the propagating fast electron beam. Filaments form due to the instabilities of the ionization front related to the electric field ionization process. This instability is located only at the fast beam edge during its propagation through the insulator. The penetration depth of the fast electron beam in plastic targets is comparable with that in metals, however in plastic beam filamentation appears after a propagation of few 10s of μm.

3.4 Ion acceleration

Several ion acceleration mechanisms have been identified in laser-solid interactions. In the target normal sheath acceleration (TNSA) mechanism [8], a fast electron population expanding into the vacuum leads to ion acceleration. In the

radiation pressure acceleration (RPA) mechanism [132], the accelerating field is due to the charge separation induced by the combination of the radiation pressure and electrostatic force. The breakout afterburner (BOA) [133] ion acceleration, in the ultrahigh contrast ratio laser- ultrathin targets (10s of nm), is sequence of TNSA, enhanced TNSA and the laser "break out afterburner". A complete description of ion acceleration in laser-plasma interaction can be found in [10, 27]. TNSA generated protons are used in this work as diagnostic of the fast electrons. This acceleration mechanism and the model used to link both species are described in this section.

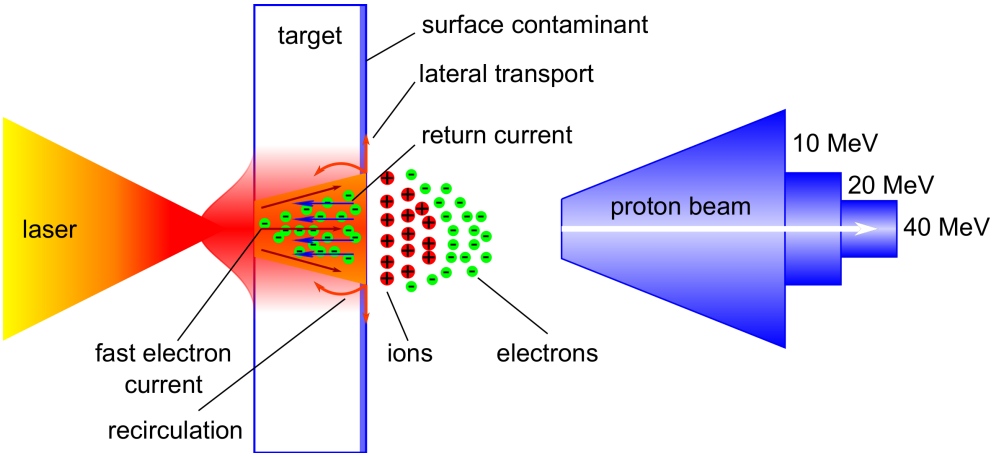

Figure 3.5: Cartoon representation of the TNSA mechanism. The protons are accelerated by the space-charge electric field generated by fast electrons escaping from the target.

3.4.1 TNSA

It was well established since 1986 [134] that the physics underlying the ion acceleration processes, in laser-matter interactions, is directly linked to the fast electrons properties. The fast electron beam, generated at the target front surface during the interaction, propagates through the solid and reaches the rear surface. There, the fast electrons escaping the solid set up an electrostatic field (TV/m) due to charge separation. This shield field expands up to the Debye length of hot electrons. Contaminants like water and oil vapor condensed on the back of the target

are ionized and accelerated in the direction normal to the rear boundary by this strong E-field, as shown in figure 3.5. This accelerated proton beam is quasi collimated and can reach peak energies of tens of MeV.

In parallel to the ion acceleration, as already mentioned part of the electrons trapped in this sheath field are reinjected into the solid where they recirculate, enhancing the proton acceleration [122]. Some electrons recirculate within the sheath field or spread laterally at the rear boundary. The most energetic electrons of the energy distribution, with kinetic energies higher than the potential of the sheath fields, escape into the vacuum. In the same way, at the target front surface a sheath field is also created that leads to ion acceleration from the front surface and to recirculation of the electrons in the solid [135].

3.4.2 Plasma expansion model

As already mentioned, TNSA generated protons can be used as diagnostic of the fast electron beam. The model of 1D isothermal plasma expansion into vacuum links the experimentally measured proton maximum energy to the fast electron beam density. This model, described below, was derived by Mora [136] in 2003. The model has been widely used previously and it requires knowledge of three main parameters: the fast electron density, the fast electron mean temperature and the ion acceleration time. Those parameters can be extracted from numerical simulations.

The isothermal expansion is described by a fluid model with hot electrons of a given temperature and cold ions, i.e. protons in this work.

At **t=0**, a semi infinite plasma initially occupies the half space ($x < 0$), with $x = 0$ the plasma-vacuum interface. The protons are cold and at rest with a step-like density profile ($n_p = n_{p0}$ for $x < 0$ and $n_p = 0$ for $x > 0$), whereas, the electron density, n_{e0}, follows a Boltzmann distribution

$$n_e(x) = n_{e0} \exp\left(e\Phi(x)/k_B T_e\right), \tag{3.13}$$

with Φ the electrostatic potential, and $n_{e0} = Zn_{p0}$ the initial electron density in the unperturbed plasma ($x = -\infty$). Z, the atomic number, is equal to 1 for the proton. The electrostatic potential satisfies Poisson's equation

$$\frac{\partial^2 \phi(x)}{\partial x^2} = \frac{e}{\epsilon_0}(n_e - Zn_p) \tag{3.14}$$

The initial electric field $E_{front,0} = -\partial\Phi/\partial x$, at the ion front (initially at $x = 0$), is obtained by integration of equation (3.14) from $x = 0$ to ∞

$$E_{front,0} = \sqrt{\frac{2}{\exp(1)}} E_0, \tag{3.15}$$

with $E_0 = \sqrt{\frac{n_{e0} k_B T_e}{\epsilon_0}} = \frac{k_B T_e}{e\lambda_{D,0}}$, and $\lambda_{D,0}$ the initial Debye length. The electric field, maximum at the plasma-vacuum interface, decreases exponentially in the plasma and as $k_B T_e/(ex)$ in the vacuum. As an example, for $k_B T_e$ ~1 MeV and $n_{e0} \sim 1 \times 10^{21}$ cm^{-3}, the peak electric field reaches $\sim 3 \times 10^{12}$ V/m, much higher than the threshold for field-ionization of hydrogen.

At $\mathbf{t > 0}$, the protons expand driven by the electric field, which is generated by the fast electrons escaping the target and forming a sheath field at the target rear boundary. The model makes the assumption of quasi-neutrality $n_e \simeq Zn_p$ and the electrons are assumed to stay in equilibrium with Φ. The ion expansion is governed by the hydrodynamic equations of continuity and motion

$$(\partial/\partial t + v_p \partial/\partial x) n_p = -n_p \partial v_p/\partial x \tag{3.16}$$

$$(\partial/\partial t + v_p \partial/\partial x) v_p = -(Ze/m_p)\partial\Phi/\partial x, \tag{3.17}$$

with v_p the ion velocity and m_p the ion mass. A self similar solution is found, for $x + c_s t > 0$, based on the quasi-neutrality assumption and using the ion sound velocity $c_s = \sqrt{(Zk_B T_e)/m_p}$ [136]

$$n_e = Zn_p = n_{e0} \exp\left(-\frac{x}{c_s t} - 1\right) \tag{3.18}$$

$$v_p = c_s + \frac{x}{t} \tag{3.19}$$

$$E_{ss} = \frac{k_B T_e}{e c_s t} = \frac{E_0}{\omega_{pp} t}, \tag{3.20}$$

with ω_{pp} the proton plasma frequency and E_{ss} the self similar electric field. The self-similar solution is valid for $\omega_{pp}t > 1$ (i.e. when $\lambda_{D,0}$ is smaller than the proton density scale length $c_s t$). Furthermore, the self-similar model predicts a proton velocity increasing without limit for $x \to \infty$. To solve this problem, the position of the ion front, where the ion velocity is maximum, can be roughly estimated from the limit of validity of the self similar solution (i.e. where the local Debye length equals $c_s t$). At this position, the self similar solution predicts a proton velocity equal to $2c_s \ln(\omega_{pp}t)$. The electric field at the ion front is then $2E_{ss}$ [136]. The electric field at the ion front, valid for any time is given by [136]

$$E_{front} = \sqrt{\frac{2}{\exp(1)}} \frac{E_0}{\sqrt{1 + t_p^2}}, \tag{3.21}$$

with $t_p = \omega_{pp}t/(2\exp(1))^{1/2}$. Knowing E_{front} from expression (3.21), the ion front velocity using the equation of motion, then the ion front position can be derived as function of time

$$v_{front} \simeq 2c_s \ln\left(t_p + \sqrt{t_p^2 + 1}\right) \tag{3.22}$$

$$x_{front} \simeq 2\sqrt{2\exp(1)}\lambda_{D,0}[t_p \ln\left(t_p + \sqrt{t_p^2 + 1}\right) - \sqrt{t_p^2 + 1} + 1] \tag{3.23}$$

The maximum proton energy is then

$$E_{max} \simeq \frac{1}{2} m_p v_{front}^2 \simeq 2Z k_B T_e \left[\ln(t_p + \sqrt{t_p^2 + 1})\right]^2 \tag{3.24}$$

The complete derivation can be found in Mora's paper [136] and also in [137]. From expression (3.24), it can be noticed that there is no time limit to ion en-

ergy gain. The electric field, being proportional to a constant T_e (isothermal) and uniform in space (1D), provides an infinite energy source for ion acceleration. However, the expansion can be considered as isothermal as long as the laser pulse accelerates electrons in the solid. Therefore, a cutoff energy E_{max} is obtained by using a finite acceleration time, t_{acc} of the order of the laser pulse duration, in the expression $t_p = \omega_{pp} t_{acc}/(2\exp(1))^{1/2}$ [135, 138, 139].

The drawbacks of this simple model come from the simplifying assumptions that do not take into account, for example, the finite size of the target that limits the fast electron reservoir, and the cooling down of the electrons, so that the distribution is no longer isothermal. The fact that electrons escape the target limits the acceleration potential. To include some of these effects, Mora [140] also developed a model taking into account the finite size of the target, and adiabatic cooling down, and including [141] a two temperature electron distribution function. Other expansion models are presented in [10, 27]. However, this model is widely used, and in spite of the limits of the model it reproduces with reasonable error margins the maximum proton energy, energy spectra while remaining relatively simple to implement.

3.4.3 Ion beam characteristics

Since the ions are accelerated by the electron sheath on the target surface (TNSA), their spatial and angular characteristics are determined by the spatial distribution of the electron sheath. Structures in the proton beam spatial profile arise from a perturbed or filamented electron beam [142].

The accelerating electric field being normal to the electron density iso-contours, a bell-shaped electron beam density distribution leads to a divergent ion beam. Therefore, ions of lower energy will have larger divergence than the ones accelerated from the sheath tip [143]. Fits to experimental data confirm that the sheath distribution is a Gaussian-like distribution [144] as has also been observed directly in sheath imaging data [145]. The ion source size [146] can be inferred using, for example, grooved targets or metal meshes placed between the ion source and the

detector [147, 148]. Using microgrooved targets [149], a proton beam source size equal to $\sim$240μm has been obtained on the Vulcan laser. Moreover, a decreasing full angle of beam spread is found for increasing proton energy (from 62° to 15° for the Vulcan laser) [149].

TNSA generated proton beams typically show an exponential energy spectrum up to a specific cutoff energy [150, 151].

Finally, the quality of a beam is defined by its emittance. A low emittance means a high beam laminarity (i.e. the proton trajectories do not overlap) and focusability. The transverse beam emittance ([mm.mrad]) is the product of the beam radius at the waist by the beam divergence. The transverse emittance of laser accelerated protons can be less than ~ 0.1 πmm.mrad [10].

Chapter 4

Methods

The experimental results discussed in this thesis were obtained using high intensity laser systems employing the chirped-pulse amplification (CPA) technique [3], introduced in the first section. The energy of the Gaussian laser pulses on target varied from 3 J to 135 J, in a pulse duration 0.8 ± 0.2 ps, giving peak intensities varying from 2×10^{18} to 6×10^{20} W/cm^2. The laser pulse was focused by an off-axis parabolic mirror onto a solid target to a spot diameter of order of few microns. The targets used are metallic foils, typically aluminium, gold or copper with thicknesses ranging from 5 to 1500 μm. To characterize the properties of the beam of fast electrons generated during the laser-solid interaction several direct and indirect techniques are commonly employed [152]. A main constraint on the choice of detector, placed inside the interaction chamber, is that it must survive the electromagnetic pulse generated during the interaction. An optical probe can be used to characterize the preplasma expansion and density at the target front surface [153]. The reflected laser beam at the target front surface enables the percentage of laser energy absorbed in the solid to be inferred. Harmonic generation at the target front surface enables the dynamics of the critical surface to be investigated [154]. Indirect methods based on X-ray emission measurements (2D imaging and spectroscopy [42, 155]) are used to probe the transport of the fast electron beam in the solid. A direct measurement of the fast electron beam distribution at the target vacuum boundaries can be made by imaging Coherent

and Optical Transition Radiation emission [118, 156].The TNSA-generated protons can be also be used as to infer the fast electron beam density. GafChromic ®Radiochromic films (RCF) [149] built into stacks are positioned a few centimeters behind the target rear surface. The energy distribution of the fast electrons leaving the solid can be obtained using an electron spectrometer [157].
To support the experimental observations, a range of numerical tools, from simple 1D analytical models to sophisticated 3D numerical simulations provide additional insight into the laser-matter interaction, hot electron generation and transport processes. This chapter describes the methods used in obtaining the results presented in the experimental chapters such as the TNSA-generated ion-beam measurement technique and the 2D imager of the $K\alpha$ emission from a fluorescent layer. Finally, the different numerical methods are presented. The chapter begins with an overview of CPA pulse generation and focusing.

4.1 CPA laser chain

In this section a typical laser chain based on the chirped-pulse amplification technique [3] is presented.

4.1.1 CPA laser chain

Since the discovery of the CPA technique, presented in figure (4.1), pulsed laser system are able to reach relativistic peak laser intensities of the order of 10^{18}-10^{22} W/cm^2. Such high laser intensities enable, among other things, to accelerate relativistic electrons. Femtosecond laser pulses enable time resolved pump-probe experiments or micro-machining applications.
The CPA technique involves the generation of tens of femtoseconds, ∼tens of nanojoules pulse (oscillator) which is stretched temporally to up to tens of picoseconds (stretcher), then amplified to up to tens-hundreds of Joules ($\sim 3-4$ amplifier stages) and then re-compressed to ∼ tens of femtoseconds (compressor).

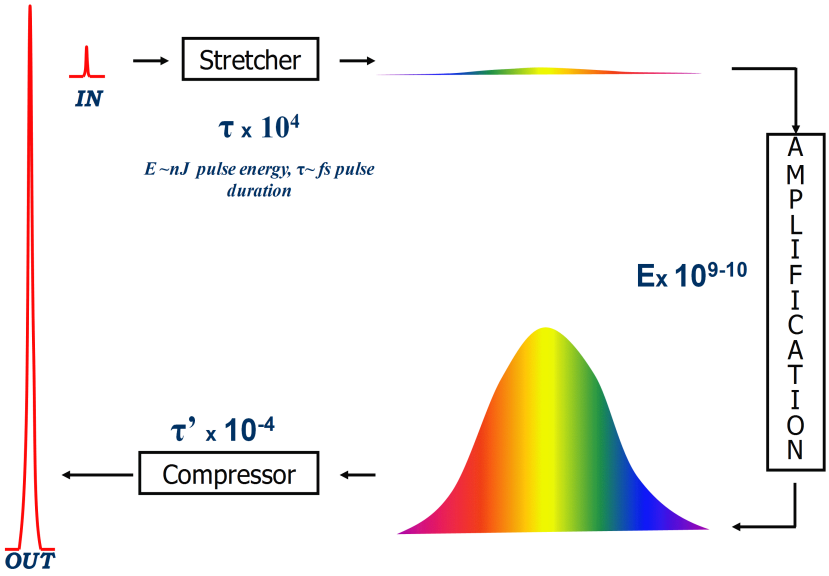

Figure 4.1: CPA technique: The nanojoule femtosecond laser pulse is temporally stretched to tens of picoseconds then the pulse energy is amplified to tens of Joules before being re-compressed temporally to obtain tens of Joules, tens of femtoseconds laser pulses.

This temporal stretching of the pulse is necessary as a direct amplification of the pulse would result in a pulse peak power much higher than the damage threshold of optical elements. In general the laser pulse temporal (imposed by the gain medium) and spatial profiles (imposed by the laser cavity) are Gaussian.

4.1.1.1 The oscillator

A typical pulsed oscillator, shown in figure (4.2), consists of a gain medium cut at a Brewster angle such as a highly doped Ti:sapphire crystal, that possesses a broadband spectral bandwidth ranging from 650 to 1100 nm and peaking at around ~800 nm, dichroic dispersive focusing mirrors, high reflective mirrors and an output coupler (OC). The dispersive mirrors are inserted to compensate for spectral dispersion induced in the laser rod. The output coupler is wedged to prevent unwanted reflections from the rear of the substrate. The additional spatial

chirp introduced by the wedged plate has to be compensated by a compensating plate (CP). The Ti:sapphire crystal is pumped by a 5 W CW (continuous wave) laser operating at 532 nm. The pump beam is focused by a lens placed behind the cavity mirror. A typical oscillator delivers $\sim$ 25 fs 4 nJ pulses at a repetition rate of 75 MHz. Without forcing the mode-locking of the cavity, then obtain a laser pulse, the system will operate in CW mode. The mode-locking of a laser cavity consists in forcing the longitudinal modes of the cavity (i.e. the standing waves frequency) to be in phase, there is only one place in the cavity where the electric fields add together constructively. Therefore, the laser oscillator must support a large number of longitudinal modes ($10^4 - 10^5$). The mode-locking can be forced in the oscillator through three main techniques referred to as passive, active and self-mode-locking. Passive mode-locking is achieved by placing a saturable absorber in the laser cavity. The absorber, which may be a dye solution, normally opaque gradually bleaches (become transparent) with increasing light intensity. Active mode-locking is achieved by amplitude modulation using an electro- or acousto-optic modulator. Self-mode-locking, the most used technique, is based on the optical Kerr effect. The laser pulse experiences in the cavity additional focusing through the nonlinear refractive index of the gain medium. The cavity is arranged for perfect overlap of the high intensity pulse in the gain medium. Generation of an initial high-intensity spike is obtained by physically perturbing a cavity mirror to create an instability in the cavity resonator.

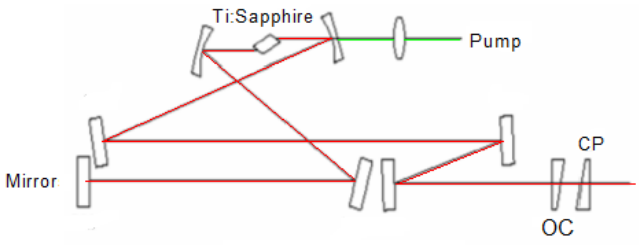

Figure 4.2: Typical MHz Ti:Sa Femtosource oscillator, reproduced from an internal report, delivering nJ-fs laser pulses at 800 nm central wavelength.

4.1.1.2 The pulse stretcher/compressor

The temporal stretching and the re-compression of a laser pulse is obtained by varying the optical path lengths for the different wavelengths, the principal of both optical systems in shown in figure (4.3). The pulse is temporally stretched by traveling through a positive delay line (the long wavelength 'red' travel the shortest path) consisting of a pair of antiparallel diffraction gratings separated by a magnification of (-1) optical system. The re-compression [158] occurs when the pulse passes through a negative delay line consisting of a pair of two parallel gratings (pulse compressor), that should compensate the positive delay line. The stretching/re-compression of the pulse is obtained by tunning the distance between the gratings. The most used stretcher is based on the Öffner triplet, the stretcher detailed design and calculations can be found in [159]. The triplet combination is composed of two spherical mirror (one mirror concave and the second convex) and a single grating. The system is almost aberration-free [160, 161] as it utilizes no lens.

4.1.1.3 The regenerative amplifier and multi-pass amplifiers

After the stretcher, the seed pulse is injecting into a regenerative amplifier by a fast polarization switch using thin film polarizers and a Pockels cell made of KDP (potassium dihydrogene phosphate). The regenerative amplifier is a laser cavity where the laser pulse is amplified to 1.2 mJ by successive passes (around 12 round trips) through the gain medium pumped by a Q-switched pump laser. After gain saturation the seed pulse is expelled from the laser cavity and then injected into a multi-pass pre-amplifier (to ∼20 mJ), where it performs several passes through the gain medium. It is then amplified to ∼2 J in the following amplifier stages consisting of a 4 pass in the gain medium pumped by several Q-switched pump lasers.

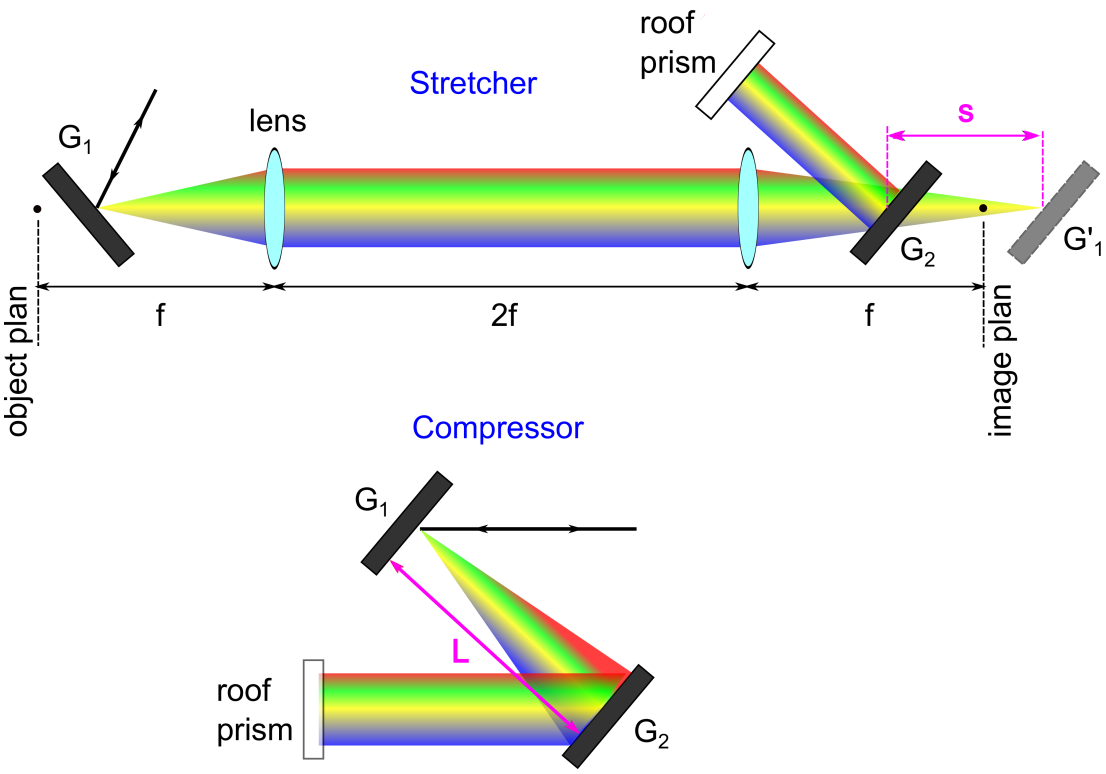

Figure 4.3: Pulse stretcher/compressor arrangement. In order to re-compress the laser pulse to its original duration, the distance between the gratings in the stretcher (S) and the compressor (L) must be the same.

4.1.2 Temporal characteristic of a Gaussian pulse

The amplitude of the electric field associated with a chirped Gaussian pulse, as shown in figure (4.4), is given by

$$\mathbf{E}(t) = E_0 \left(e^{-\Gamma t^2} e^{-i\omega_L t} \right), \tag{4.1}$$

with E_0 the E-field amplitude, ω_L the carrier frequency. The electric field oscillates at the angular frequency ω_L corresponding to the central wavelength of the pulse. I_L is given by

$$I_L(t) = I_0 e^{-2\Gamma t^2}, \tag{4.2}$$

where I_0 is the peak intensity. Γ is related to the intensity full-width at half maximum by $FWHM = \sqrt{2\ln 2}/\sqrt{\Gamma}$.

The intensity $I_L[\mathrm{W/cm^2}]$ of the laser pulse is defined as the laser pulse energy

(E_L) per second (the pulse duration τ_L) per unit area (the spot area defined by the radius referred as to w in the chapter)

$$I_L[W/cm^2] = \frac{E_L}{\tau_L(\pi w^2)}. \tag{4.3}$$

The local intensity, for a linearly polarized laser pulse, is related to the amplitude

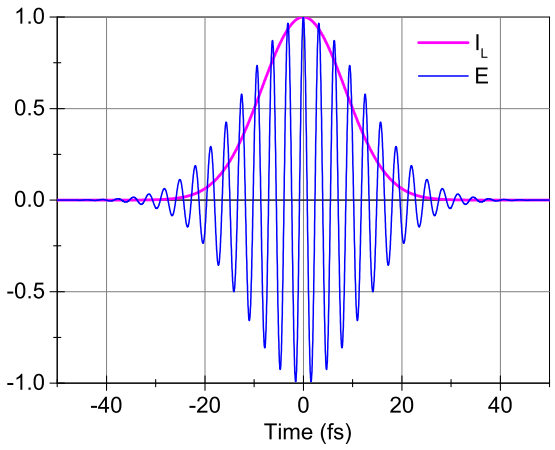

Figure 4.4: Intensity and Electric field of a $\sim$ 20 fs chirped laser pulse.

E of the electric field via $\frac{1}{2}c\epsilon_0|E(t)|^2$.The maximum of the normalized vector potential $a_0 \geq 1$ ($I_L \geq 10^{18}$ Wcm^{-2}) defines the relativistic regime thus accelerates electrons to relativistic velocities while oscillating in the laser field.

4.1.3 Focused Gaussian laser beam

Most high intensity experimental setups use focusing optics such as off axis parabolas to focus the laser pulse onto the target. This section discusses the beam properties after focusing [162].

A perfect Gaussian beam, where only the fundamental mode TEM$_{00}$ propagates, with a initial radius w can be focused to a minimal radius of

$$w_0 = \frac{\lambda_L f}{\pi w}, \tag{4.4}$$

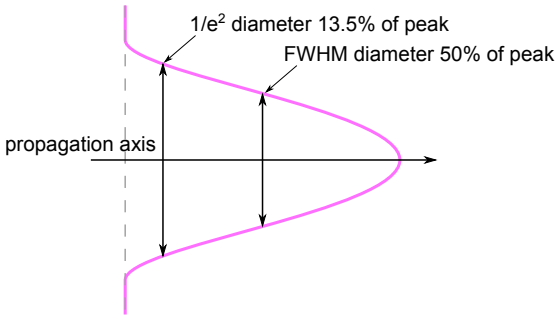

Figure 4.5: Gaussian beam profile [162].

with f the focal length of the focusing optics, λ_L the laser pulse wavelength and w_0 the waist of the laser beam ($I_L \frac{1}{e^2}$). The distance over which the beam remains focused with maximum intensity is defined by the Rayleigh length

$$z_R = \frac{\pi w_0^2}{\lambda_L}. \tag{4.5}$$

z_R is the distance over which the beam radius increases by $\sqrt{2}$. The propagation of a Gaussian beam is illustrated in figure (4.5) and (4.6).

The radius of the Gaussian beam at a given position z on the propagation axis, is given by

$$w(z) = w_0 \left[1 + \left(\frac{z}{z_R}\right)^2\right]^{1/2}. \tag{4.6}$$

Near the laser focus, the divergence angle is extremely small. Far from the focus the divergence angle approaches the asymptotic limit θ given by $\theta \cong \frac{w(z)}{z} = \frac{\lambda_L}{\pi w_0}$. This value is called the far field angular radius (half-angle divergence) of the Gaussian beam.

The spatial beam quality is defined by the M^2 parameter. As higher order modes propagate in the cavity (in addition to the TEM_{00}), the output laser beam spatial profile is usually multi-mode and does not propagate according to equation (4.6). A dimensionless beam propagation parameter has then been developed to determine the characteristics of real beam (i.e. taking into account all the TEM modes oscillating in the cavity) propagation and is given by $M^2 = \frac{w_0'.\theta'}{w_0.\theta}$, with w_0' and θ' the waist and far-field divergence of a real beam, respectively. A pure Gaussian beam is defined by $M^2 = 1$.

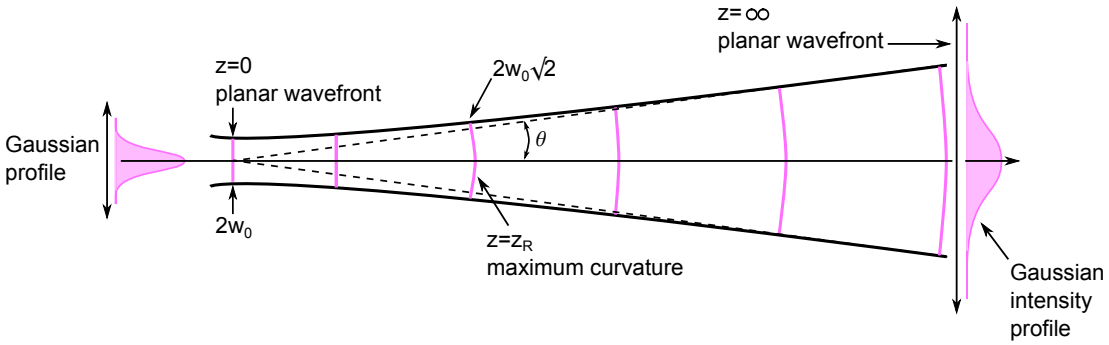

Figure 4.6: Propagation of a Gaussian beam [162]: The laser beam shows small divergence up to the Rayleigh length z_R, where the beam radius is increased by $\sqrt{2}$, then starts to diverge with respect to equation (4.6).

4.2 Diagnostics of fast electron transport in solids based on X-ray emission measurements

One of the primary diagnostics of fast electron transport in dense targets is spectrally and spatially resolved measurements of $K\alpha$ emission. The $K\alpha$ emission, from buried fluorescence layer, enables the fast electron beam size at a given depth in the solid, the background heating and the fast electron number, and the laser-to-electron conversion efficiency to be inferred.

4.2.1 $K\alpha$ emission

While propagating through the solid, the fast electrons lose energy to the background by collisions, which transfer kinetic energy via several mechanisms such as ionisation and excitation. $K\alpha$ emission results from the transition of an electron from L-shell to fill a vacancy left in the K-shell due to K-shell electron ionization by impact of fast electrons with energy higher than the ionization threshold of the K-shell. Thus the resultant vacancy in the inner K-shell can be filled by an electron from another shell, as can be seen in the figure (4.7). An X-ray photon or an 'Auger' electron is emitted during this electronic transition to the inner shell.

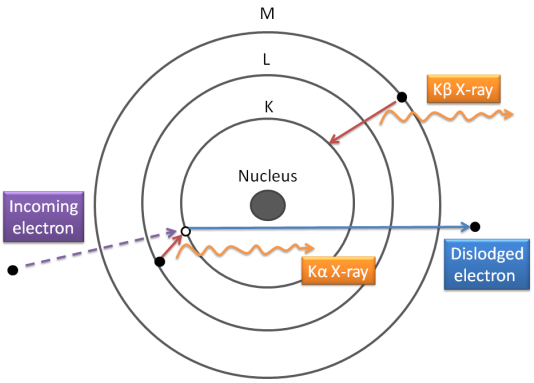

Figure 4.7: Cartoon of the K-Shell emission.

The probability that an electron of initial kinetic energy E_e ionises the K-shell depends on the K-shell ionization cross section σ_K [163]. As can be seen in figure (4.8), the Cu cross section presents a maximum around the ionisation potential at ~ 50 keV. This indicates that the Cu $K\alpha$ signal is highly sensitive to electrons in this range. At higher energies, the cross section decreases and increases again due to relativistic effects [163]. The fluorescence yield for a K-shell vacancy W_k [164]

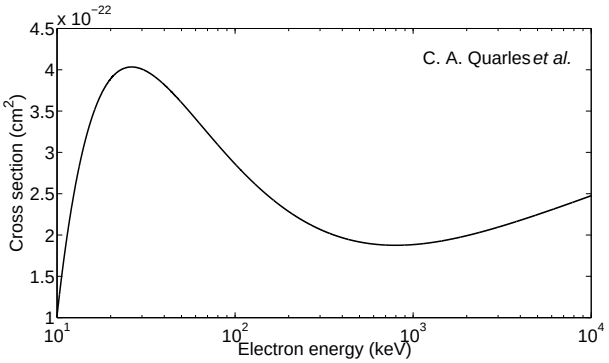

Figure 4.8: Differential cross section for K-Shell ionization of Cu [163] as function of electron energy.

is equal to $Z^4/(Z^4 + 1.12 \times 10^6)$, where Z is the atomic number. This represents the fraction of excited atoms that go through radiative decay (in competition with the Auger decay), which increases with increasing Z. The expected number of $K\alpha$ photons N_K (the $K\alpha$ yield) emitted by a layer of thickness dL is directly

proportional to the number of electrons and is given by

$$N_K = N_e(E_e)\sigma_K(E_e)W_K n_i dL \tag{4.7}$$

[41] , where $N_e(E_e)$ is the number of electrons at energy E_e and n_i is the number density of the fluorescent layer. The $K\alpha$ emission is considered isotropic and thus N_K is the total photon number into 4π steradians.
Finally, the discrete shift in the K-shell emission wavelength (depending on the ionisation state of the layer) from the multiply ionised fluorescent layer (the $K\alpha$ emission spectra) allows the layer temperature to be inferred by measuring the change in the $K\alpha$ line ratio. Numerical simulations with a collisional radiative code such as FLYCHK [165] are required to calculate from the measured spectra the heating of the ionized layer [166].

4.2.2 2D imaging crystal

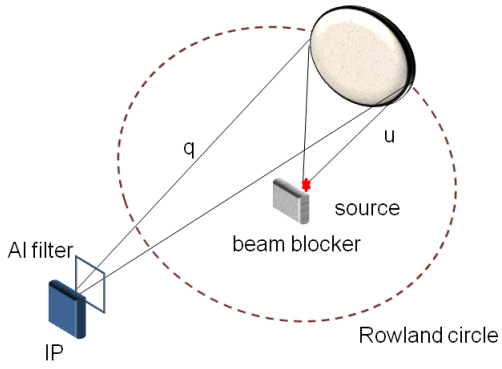

Figure 4.9: Cartoon showing spherically bent Bragg crystal.

Two-dimensionally spherically-bent Bragg crystals, such as quartz 100 [167] or quartz 101 [168], are routinely used to obtain monochromatic spatially resolved 2D images of X-rays emission, for example the images shown in figures (4.10), of

planar targets with buried fluorescent layers [14, 15]. High spatial resolutions of ~ 2 μm have been achievied using a quartz 101 crystal.

The system and alignment procedure are detailed in Koch *et al.* [155]: In order to image a specific wavelength λ_L the Bragg equation must be satisfied

$$n\lambda = 2d \sin\theta, \tag{4.8}$$

where θ is the grazing angle or Bragg angle of incidence, n is the order of reflection and d the interplanar spacing. The system magnification is equal to the ratio q/u where q is the distance from crystal to detector and u is the distance from crystal to source. The diagnostic arrangement is shown in figure (4.9).

The $K\alpha$ imager used in this work, to measure the Cu $K\alpha$ lateral extent, consists of a spherically bent Bragg crystal and FujiFilm BAS imaging plates [169, 170]. The crystal was composed of quartz 211 and had a 38 cm radius of curvature, 1.542 $\mathring{A}$ lattice spacing and a diameter of 22 mm. This required an incidence angle, with respect to the crystal normal, of 1.3° in order to satisfy the Bragg condition for second order diffraction for Cu $K\alpha$ emission at ∼8 keV. The magnification was 10. The spatial resolution at the source is of the order of ∼20 μm [171] (the IP grain size is equal to $\sim (25 \times 25)$ μm^2). The energy bandwidth ΔE was 8 eV, thus $K\alpha$ emission from line drift due to heating of the fluorescent layer may not be recorded. The crystal was covered with Mylar to protect from debris and a beam blocker was inserted between the target and the IP to avoid recording direct emission from the target. As already mentioned, the Cu K-shell ionization cross section by electron bombardment [172], presented in figure (4.7), shows a sharp peak at an electron energy of $\sim$ 40 keV then rapidly decays between $\sim$ 50 keV to $\sim$ 1 MeV and then finally increases slowly for higher energies. The electron angular broadening due to scattering in the solid target is more significant for the keV energy electrons compared to the MeV electrons. Because of the cross-section local maximum at electron energy of $\sim$ 50 keV, the experimentally measured 2D images of the Cu K_α could mainly provide the size of the 100s keV electrons.

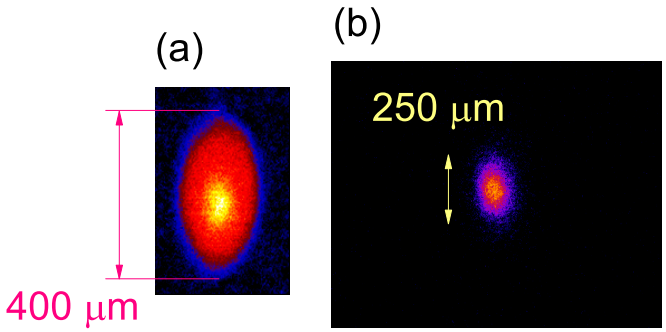

Figure 4.10: An example of 2D imaging of the Cu $K\alpha$ emission obtained from: (a) 20μm-thick Cu mass limited disk; (b) 100μmAl-5μmCu-1μmAl targets.

4.3 Proton diagnostic: RCF

Stacks of calibrated GafChromic ®Radiochromic films (RCF), preferentially sensitive to protons, are routinely used as diagnostics of the proton beam spatial intensity and energy distribution. RCF dosimetry films [173] of the types HD-810, HS and MD-55 are widely used for dose measurement of energetic photons, electrons and protons (spatial distribution and dose measurement) [149]. RCF

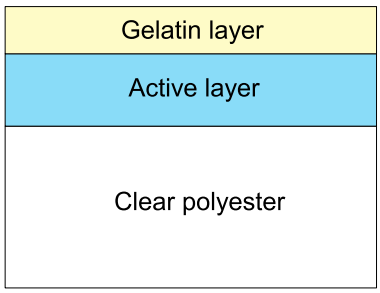

Figure 4.11: HD-810 film configuration. The gelatin layer is 0.75μm-thick, the active layer is 6.5μm-thick and the polyester is ∼97μm-thick.

are radiation-dose sensitive films consisting of an active layer that when exposed

to ionizing radiation, changes its optical density from transparent to different shades of blue depending on the amount of radiation (dose) absorbed by the film. The configuration of HD-810 is shown in figure (4.11). The standard sensitivity range, given by the manufacturer, is, for example, 10-400 Gy for the HD-810 (suitable for high doses) used in this work. RCF possess high spatial resolution due to the small $\sim (2 \times 2)$ μm^2 grain size of the sensitive layer. RCF needs to be handled and stored with care as it is light-sensitive as well as being susceptible to scratches that alter the film color. About 90% of the coloration takes place just after irradiation. After 24 hours it increases by 16% then stays constant for years if well stored.

Particles propagating in a plasma lose energy via collisions with the background electrons and ions. While electrons gradually lose their energy in the background plasma, ions deposit most of their energy at their stopping location (Bragg peak). The SRIM code package [174] provides the Bragg curve (energy loss of the particle/unit path length (stopping power of the propagation layer) as a function of the path length) of a specific propagation layer at a given initial ion energy. To measure the proton energy spectrum, a stack of alternating layers of RCF and filters is employed. The Bragg curve, and thereby the proton cutoff energy, is then calculated using the SRIM code. The protons cutoff energy increases with increasing stack depth. In order to extract the proton energy spectrum (i.e. to extract the dose absorbed by each RCF), the RCF needs to be scanned. The pixel value of the scanned RCF image, corresponding to an absorption value or optical density, need to be calibrated with known dose for the specific scanner used. In this work, stacked dosimetry film pieces (RCF HD-810) [149], positioned 5 cm from the rear of the target, are used to record the energy distribution and spatial beam profile of the emitted proton beam. The energy range covered by this diagnostic was 1.2 to 40 MeV.

4.4 Simulation tools

The modeling of the laser- overdense plasma interactions can be performed by a range of different types of code, as shown in figure (4.12). The appropriate choice of the numerical code depends on the phenomena of interest as well as the availability of computation resources:

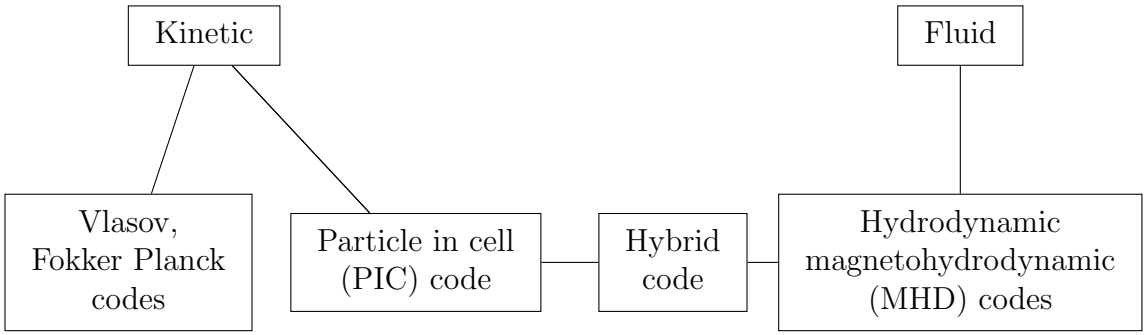

Figure 4.12: Numerical models of plasmas.

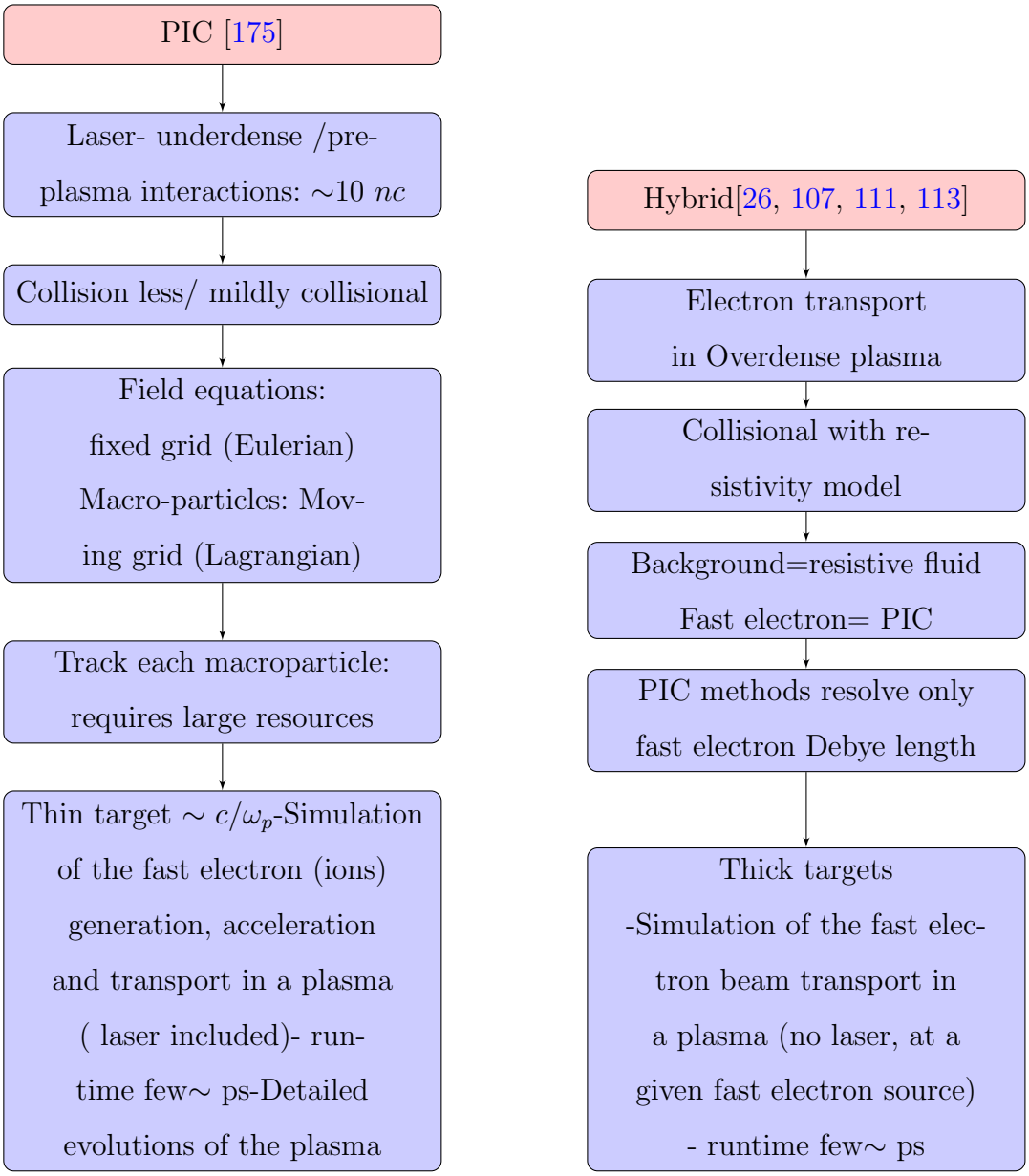
PIC [175]
Laser- underdense /pre-plasma interactions: ∼10 nc
Collision less/ mildly collisional
Field equations: fixed grid (Eulerian) Macro-particles: Moving grid (Lagrangian)
Track each macroparticle: requires large resources
Thin target ∼ c/ω_p-Simulation of the fast electron (ions) generation, acceleration and transport in a plasma (laser included)- runtime few∼ ps-Detailed evolutions of the plasma
Hybrid[26, 107, 111, 113]
Electron transport in Overdense plasma
Collisional with resistivity model
Background=resistive fluid Fast electron= PIC
PIC methods resolve only fast electron Debye length
Thick targets -Simulation of the fast electron beam transport in a plasma (no laser, at a given fast electron source) - runtime few∼ ps

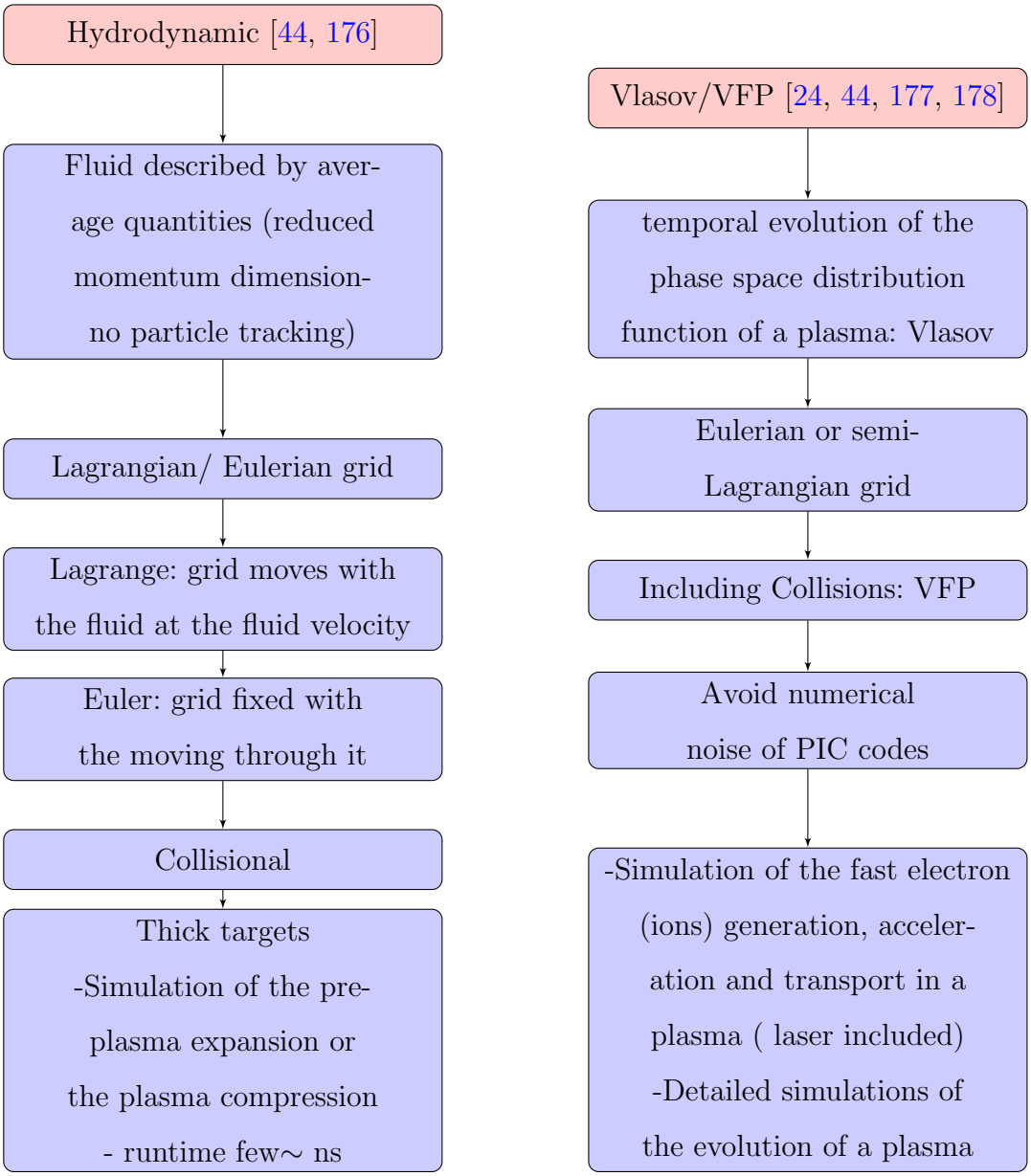

4.4.1 Vlasov-Fokker Planck

Vlasov or Vlasov-Fokker Planck codes are methods for solving the Vlasov equation that describes the evolution of the velocity/momentum distribution function of plasma electrons (and ions). The Vlasov-Fokker Planck equation is the Vlasov equation including a collision term composed of a drag part and a diffusion part. The plasma is well described by a 6 dimensional phase space distribution function

$(f(\mathbf{r}, \mathbf{v}, t))$ solution of the Vlasov equation. The Vlasov equation is

$$\frac{\partial f}{\partial t} + v.\nabla f + \frac{q}{m}(\mathbf{E} + \mathbf{v} \times \mathbf{B}).\frac{\partial f}{\partial \mathbf{v}} = 0. \tag{4.9}$$

E and **B** fields are calculated using Maxwell's equations. Vlasov codes provide a low noise detailed study of plasmas with a very high resolution of the phase space.

However, those codes require heavy computational resources to follow the particles along their trajectories in 6D phase space (3D spatial grids+3D velocity space grids) when solving the Vlasov equation. In addition, the large range between the maximum and minimum values of physical parameters, such as the electron energy range requires also heavy computational resources. However, as Vlasov codes directly solve the Vlasov partial differential equation, they avoid the noise generated using PIC methods.

4.4.2 Particle In Cell code

The Particle-in-Cell (PIC) method is a general numerical method that in cases of interest here solves the Vlasov collision-less kinetic equation of plasmas. Partial differential equations are reduced to ordinary differential equations and discretized. The plasma is described by a group of macro-particles, themselves representing a large number of real particles. They are tracked individually in a volume described by a fixed grid. The grid-cell width Δx where variations in space are resolved and the time step Δt, have to be chosen carefully to satisfy the Courant-Friedrichs-Lewy condition for convergence while solving partial differential equations. Input parameters describing the initial physical conditions such as the laser parameters, the background plasma parameters, the distribution function and the EM field also have to be provided. As an example, in OSIRIS code [179] the number of macro-particles/grid-cell is fixed but the number density/grid-cell can be varied meaning that the number of real particles that a macro-particle in a cell represents varies from one cell to another. When modeling laser-overdense

plasma interactions i.e. high plasma frequency ω_p, the distance between two grid points Δx should be smaller than the Debye length to avoid artificial heating of the plasma. The numerical heating is due to the non conservation of the plasma total energy (only the momenta are conserved) in PIC codes. In laser-underdense plasma interactions, the cell size should be a fraction of the laser wavelength λ_L, typically in OSIRIS $\Delta x = \lambda_L/20$. In 1D, Δt must be smaller than $\Delta x/c$.
As a particle can be anywhere within a cell, the charge of a particle is distributed over neighboring grid points. Then the charge density (ρ) and the current density ($\mathbf{J} = \rho \times \mathbf{v}$ with $\mathbf{v}$ the velocity) are evaluated on each grid point. Following from this, the electric and magnetic fields ($\mathbf{E}$, $\mathbf{B}$) are calculated on the grid-points using Maxwell equations ($\epsilon_0 \nabla \cdot \mathbf{E} = \rho$) and ($\nabla \times \mathbf{B} = \mu_0 \mathbf{J} + \frac{1}{c^2} \partial \mathbf{E}/\partial t$). The fields are projected onto the macro-particles facilitating the calculation of the force acting up on them. The macro-particles are then moved following the equations of motion $\frac{d\mathbf{p}}{dt} = -e(\mathbf{E} + \mathbf{v} \times \mathbf{B})$. Collision and collisional ionization processes are in general poorly implemented in PIC codes (via Monte Carlo method).
The drawbacks of the PIC method are the generation of statistical noise and the requirement for heavy computational resources.

4.4.3 Hydrodynamic

There exist different hydrodynamic methods that may be used to model a laser induced plasma starting with a single fluid approach, extended to a two-fluid description (electrons and one ion species).
The fluid consists of electrons while the ions are treated as an immobile, neutralizing background. The plasma is characterized mainly by macroscopic parameters such as the charge density, average velocity and temperature, which are functions of spatial coordinates and time.
Hydrodynamic codes are grid-based methods where the macroscopic parameters are evaluated on grid points. The grid can be static (Eulerian coordinates) or can move with the fluid (Lagrangian coordinates).
The plasma, treated as a fluid in local thermodynamic equilibrium (the time it

takes for a fluid particle to adjust to changes is short relative to the timescale of the flow), is described by general macroscopic hydrodynamic equations closed by an equations of state (giving the pressure and internal energy e_i at a given density and temperature) and transport coefficients (to include collisions).
The hydrodynamic equations, already described in chapter (2), are :

- The conservation of total mass (continuity equation)

$$\partial\rho_m/\partial t + \nabla.(\rho_m \mathbf{v}) = 0$$

  with ρ_m the mass density and $\mathbf{v}$ the velocity.

- The momentum conservation (Navier-Stokes equation)

$$\rho_m(\partial\mathbf{v}/\partial t + (\mathbf{v}.\nabla)(\mathbf{v})) = -\nabla p_p$$

  with p_p the pressure.

- The total energy density (including the internal heat energy) e_T

$$\partial\rho_m e_T/\partial t + \nabla.((\rho_m e_T + p_p)\mathbf{v}) = 0.$$

Then, after closing the system of equations enumerated above with an appropriate equation of state, the evolution of the fluid is obtained using the Navier-Stokes equation where collisions and external fields can be included.
The drawback of hydrodynamic codes, and any codes modeling a resistive plasma at low temperature, comes from the available plasma resistivity models, which are in general not well characterized at low temperature and thus can generate numerical artifacts.

4.4.4 Hybrid code

When modeling fast electron transport in dense plasma using hybrid codes, the fast electrons are represented by macro-particles of a *given* distribution function and are treated kinetically (FP or PIC methods) while the background plasma is treated as a cold resistive fluid. Therefore, hybrid codes provide detailed description of the fast electron evolution and the basic behavior of the background plasma without requiring massive computational resources. The background plasma temperature varies in time due to resistive heating and collisions with fast electrons. Consequently its resistivity varies leading to a variation of the fields acting on the fast electron beam. The main advantage of hybrid codes, although less precise than PIC methods, is that they run quickly and use less computational resources because they use larger spatial grids and time steps as compared to full PIC calculations.
The disadvantage of those codes is that the fast electron distribution need to be defined, therefore it requires several runs, using different initial electron source distributions, to allow a more accurate comparison with experimental results. Also, the background resistivity and specific heat capacity, which are not well known parameters in laser solid experiments, need to be specified.

Description of the simulation code ZEPHYROS

The 3D hybrid code ZEPHYROS, described in references [16, 110, 112] and similar to the one detailed in papers by Davies [107, 109], is used in this work to simulate fast electron beam propagation in Al and Au.
In references [107, 109], Davies describes a hybrid code, which is similar to ZEPHYROS, as follows: The code models the transport of a given fast electron distribution function in a uniform plasma. To differentiate between the fast electrons and the background electrons, the background particles are considered as a bulk and the fast electrons are treated particles. The fast electrons are described by a Fokker-Planck equation. Basically the trajectory of a macro-particle,

representing a specific number of fast electrons of the velocity distribution, is tracked (PIC method) subject to the self-generated fields in the background and to collisions with the background. The background electrons and ions are treated as fluids and are described in term of their current density and fields. The macroparticles move according to the relativistic equation of motion including both the Lorentz force exerted by the B-field and collisions with the background. The collisions are represented by a drag term $dp = -(D/2mv^2)\ln\Lambda_l dt$ which changes the momentum magnitude. In addition to the drag term, a random rotation term $d\theta = 1/p\sqrt{(ZD/v)\ln\Lambda_s}\Gamma(t)dt^{1/2}$ (Γ is calculated using Monte Carlo method) deflects the particle, with θ the random scattering angle, p the momentum, $D = n_b e^4/2\pi\epsilon_0^2$ and n_b the background density, e the electron charge, ϵ_0 the vacuum permittivity, m the electron mass, v the electron velocity, Z the atomic number, $\Gamma(t)$ the time varying random number and $\ln\Lambda_s$ [180] & $\ln\Lambda_l$[181] depend on the background. The response of the background is modeled by the return current density thus the self-generated E-field via Ohm's law. Using Ohm's law, the E-field is equal to $\eta\mathbf{J_b}$, with η the solid target resistivity and $\mathbf{J_b}$ the background current density (or return current). Using Ampere's law and neglecting the displacement current $\partial\mathbf{E}/\partial t$ the B-field is then $\nabla\times\mathbf{B} = \mu_0\mathbf{J}$, with $\mathbf{J}$ the net current and μ_0 the vacuum permeability. The current neutralization requires that $\mathbf{J_b} + \mathbf{J_f} = 0$, with $\mathbf{J_f}$ the hot electrons current density. Thus, the induced magnetic field, using Faraday's law, is then

$$\partial\mathbf{B}/\partial t = -\nabla\times\mathbf{E} = \nabla\eta\times\mathbf{J_f} + \eta\nabla\times\mathbf{J_f} - \nabla\times(\eta/\mu_0\nabla\times\mathbf{B}) \tag{4.10}$$

The gradients in the current density generate B-fields that increase these gradients and lead to beam pinching and filamentation. Gradients in target heating lead to gradients in resistivity and thus contribute to B-field evolution. When the resistivity increases with the temperature, the beam is pinched more strongly. By contrast when the resistivity decreases with temperature the fast electrons are pushed outwards. The last term on the right hand side of the equation (4.10) represents the magnetic diffusion (the B-field variation with the background) ne-

glected in the model. The main heating mechanisms for the background ($\partial T_b/\partial t$) are the Ohmic heating in addition to the collisions represented by the drag term on the fast electrons.

The self generated fields can be artificially suppressed. By suppression of the self-generated resistive B-fields in the simulation, the fast electrons will only interact with the background via the drag and the random rotation terms.

Chapter 5

Investigation of fast electron beam injection and divergence in solids

In this chapter, the divergence angle of the beam of fast electrons, generated in ultra-high intensity laser solid interactions, is experimentally investigated. The results are compared with 3D hybrid code simulations to distinguish between the fast electron beam transport angle, controlled by the self-generated, resistive, azimuthal B-field, and the injection angle, which is a function of the laser-solid interaction conditions. Measurements of TNSA-generated proton beams [8, 136] and 2D images of the Cu Kα emission [1, 2, 14, 15, 85] from a buried fluorescent layer are used as diagnostics of the fast electron beam transport.

The first section of this chapter presents discussion on the influence of resistive self-generated azimuthal magnetic fields on the fast electron beam transport, highlighting the difference between the fast electron beam injection angle and the effective total propagation angle. In the second section, the experimental set-up is introduced. Simulations and related analytical modeling are then compared to experiment. Finally, the proton experimental measurements for Al are compared to previous experimental results obtained for a higher-Z material Au and to results

obtained using Al under a defocused laser spot irradiation ($\sim 5.5 \times 10^{18}$ W/cm^2).

5.1 Generality on fast electron transport in solids

The transport of suprathermal electrons and consequently the beam divergence in an overdense background plasma is affected by collisionless processes involving self generated fields and by collisions, depending mainly on the background density and temperature.

Collisions are important in high-Z material, such as Au, as used in this work. Elastic collisions between the fast electrons and the ions or electrons in the background lead to the angular scattering of the fast electron beam. Inelastic collisions imply energy loss mechanisms that slow down the fast electron beam and heat the background, therefore changing the background resistivity and thus altering the self-generated resistive fields.

The collisionless processes come from the strong self-generated EM fields driven by the large fast electron current propagating in the solid. An electric field, that inhibits the beam propagation, is rapidly set up by the large current of fast electrons entering the solid due to charge separation. The fast electron beam with current above the Alfvén current limit can propagate though the solid background only in the presence of a cold return current provided by the target. This return current, induced by the electric field, compensates the lack of electrons at the target front surface caused by the laser ionization and maintains a local charge neutrality necessary for the beam propagation. According to Ampère's law, a magnetic field is then produced. It acts to pinch the fast electrons injected into the solid [23–25]. Bell *et al.* [24], using Fokker-Planck code simulation results coupled with analytical calculations, demonstrated that a non-strongly anisotropic fast electron source can be collimated into a beam propagating through the solid, by the azimuthal B-field, and a condition for the collimation to occur was derived. By numerically simulating the fast electron transport in thick plastic targets, with parameters corresponding to experiments made on Vulcan, Davies *et al.* [23] de-

picted a global picture of the effect of the self-generated fields on the fast electron beam. It is shown that, the electric field generated at the beginning of the electron acceleration in the solid, opposes to its propagation, leading to a strong heating of the background plasma. Rapidly an azimuthal magnetic field, that pinches the fast electron beam, is generated due the radial variation of the E-field. Then, the fall in the E-field strength, due to the strong heating that can lower the background resistivity, leads to a fall in the B-field strength that limits the beam pinching. Finally, the presence of a collisional return current, coupled with the change in the background resistivity that affects the self-generated fields, leads to beam-plasma instabilities, thus altering the electron beam transport/divergence.

Effect of target thickness on fast electron beam transport and on the resulting TNSA generated proton beam

The main fast electron beam transport diagnostic in this study is the target normal sheath acceleration (TNSA) generated proton beam. The sheath fields formed at the target vacuum boundaries, which give raise to ion acceleration, reflect most of the fast electrons leaving the solid and pulls them back into the target where they recirculate [182]. It has been demonstrated that the proton maximum energy depends on the target thickness [122, 182, 183] as it scales with the fast electron beam density, enhanced by the electron recirculation in foils. If we consider an electron bunch that is injected at relativistic velocity in a solid and experiences little energy loss, considering that the solid is a metal such as Al, the duration of the bunch will be $\sim \tau_L$. For thick targets, the electrons, injected into the solid at the beginning of the interaction and reinjected in the solid at the rear boundary, will spread away from the forward electrons injected later during the interaction, thus have small effect on the beam density. The laser pulse duration in this work is equal to $\sim 0.8 \pm 0.2$ ps, thus the effect of refluxing (i.e. recirculating) fast electrons on the beam density is minimized for ≥ 100 μm-thick targets used in this study. Hey *et al.* discussed the effect of the target thickness [183] in Au solid targets on the proton beam maximum energy and

laser-to-proton conversion efficiency. That study includes 2D hybrid simulations of proton acceleration and an experimental data set obtained on Au solid targets of thickness 5, 10, 15, 20, 100 and 250 μm at laser pulse intensity of 9×10^{19} W/cm^2 and duration of 0.6 ps. Hey *et al.* demonstrated that for sub 20μm-thick targets the laser-to-proton conversion efficiency remains constant and the hot electron collisional and Ohmic energy losses in the solid are comparable to the adiabatic electron-proton energy transfer. For thicker targets, collisional and Ohmic energy losses become predominant (i.e. energy loss to the background plasma) thus the laser-to-proton conversion efficiency decreases with increasing target thickness. Later in this chapter new results with Au targets will be discussed with reference to the results of Hey *et al.*.

5.1.1 Difference between the fast electron beam injection and transport angles

Various complex interlinked processes alter the fast electron beam transport, and thus the beam divergence, in solid targets. Due to the self-generated fields and the plasma-beam instabilities that develop after the beam injection, the measured fast electron beam transport angle will generally be different from the injected angular distribution.

Experimental campaigns have been performed to investigate the fast electron beam divergence angle (by measuring the effective beam transport angle) within metallic targets. Employing diagnostics based on measurements of optical and X-ray emission, Green *et al.* and Lancaster *et al.* found that the beam transport half-angle increases with intensity, from $\sim 17^\circ$ at 4×10^{19} W/cm^2 to $\sim 27^\circ$ at 5×10^{20} W/cm^2 (for picosecond laser pulses) [14, 15].

Recently, based on hybrid simulation results, Honrubia and Meyer-ter-Vehn [26] concluded that in order to reproduce these measured fast electron beam transport angles, a larger initial injection half-angle of $\sim 50^\circ$ is required. The realization that the initial divergence of the fast electrons might be large has led to theoretical and experimental studies of schemes to solve this problem and to produce collimated

or focused beams [110–114].

In this chapter the fast electron transport angles are investigated via simultaneous measurements of proton acceleration and $K\alpha$ fluorescence imaging. Then, the results from 3D hybrid simulations are used to infer the fast electron injection angle.

5.2 Experimental set-up

The experiment described in this chapter was carried out at the Rutherford Appleton Laboratory. Planar aluminium foils were irradiated using the p-polarized pulses from the Vulcan laser [184] with pulse energy on target, E_L=(125±25) J (corresponding to 50% of the total energy on target in the laser spot) in a pulse duration, $\tau_L = 0.8 \pm 0.2$ ps, at a wavelength, λ of 1.054 μm. The laser incident angle was 23° with respect to the laser axis. The beam was focused on the solid target, by an f/3 off-axis parabola, down to a laser spot diameter (FWHM) ϕ_L= 8 μm. The laser intensity contrast ratio (peak to amplified spontaneous emission pedestal) was higher than 10^9 at 1 ns and 10^8 at tens of picoseconds, prior to the peak of the pulse. Modeling of the generated preplasma showed limited hydrodynamic expansion before the arrival of the peak of the pulse. The main data set was obtained using planar 5 mm × 5 mm targets consisting of an Al front propagation layer of thickness, L, varied from 100- 500 μm, a 5 μm thick Cu fluorescent layer and a 1 μm thick Al rear surface layer i.e. Al-Cu-Al layered targets. The Al rear surface layer prevents fluorescence of the Cu due to the lateral spreading of the electron current on the target rear surface [185]. In addition, a limited number of shots obtained using a defocused laser irradiated spot were performed during the experimental campaign. Data scans for ϕ_L = 35 μm and 60 μm, were performed on planar layered targets using L =20 - 1000 μm thick Al, 5 μm thick Cu fluorescent layer and L_{rear} =500 μm thick CH. The CH layer minimizes refluxing of the fast electrons, enabling the measurement of the fast electron beam size in the Cu resulting from a single transit of the fast electrons.

A spherically bent Bragg crystal coupled with Fujifilm BAS imaging plates [155, 169], imaging the Kα emission from the target rear surface side, was used to make time-integrated measurements of 2D images of the Kα radiation emitted from the Cu layer. The magnification was 10. Stacked dosimetry film (RCF HD-810) [149], positioned 5 cm from the rear of the target, was used to measure spectral and spatial intensity distributions of the beam of protons from the rear surface, by fast electron-induced sheath field. The energy range covered by this diagnostic was 1.2 to 40 MeV.

A scan in thickness, under a laser spot diameter of 60 μm, was also performed using the same layered Al targets as the main data set, with L varied from 20- 1000 μm. An additional scan using planar gold targets, of thicknesses varying from $5 - 250$ μm obtained during a previous experimental campaign, enables a comparison with a high-Z material. The experimental set-up used for the Au results is introduced in Yuan *et al.* [186], using the same laser and a similar experimental set-up to the one presented in this paper. The experimental results obtained on Au and under defocused laser irradiated spot are presented later in this chapter for comparison with the main data set.

In the remainder of the chapter, the experimental scans performed on Al and Au at tight focus and Al under defocused irradiation will be referred as to Al-Cu-Al, Au and Al_{60}, respectively. The two scans using CH layer at the rear surface, will be referred as to Al-$CH_{\phi_L=35}$ and Al-$CH_{\phi_L=60}$.

5.3 Al-Cu-Al experiment results

The main experimental results of this investigation are presented in figure (5.1). Figure (5.1(a)) shows the lateral extent (half width at half maximum (HWHM), measured in the vertical direction) of the Cu Kα signal at two values of L. The thickest target for which a clear Kα signal was recorded was 250 μm, which limited the thickness range over which this diagnostic approach could be applied. The results are in good agreement with previous measurements of Kα fluorescence

from thinner Cu foils made with the same laser and very similar laser pulse parameters, as shown in figure (5.1(a)). An effective beam transport half-angle of $\sim 24°$ is inferred if a linear fit is applied to the data points.

Figure (5.1(b)) shows the measured maximum proton energy, E_{max}, as a function of L. A decrease in E_{max} with increasing L is measured. A good agreement is found with results from a previous experimental campaign made with the same laser and very similar laser pulse parameters on Al targets (Yuan *et al.* [186]), highlighting the reproducibility of the data scans.

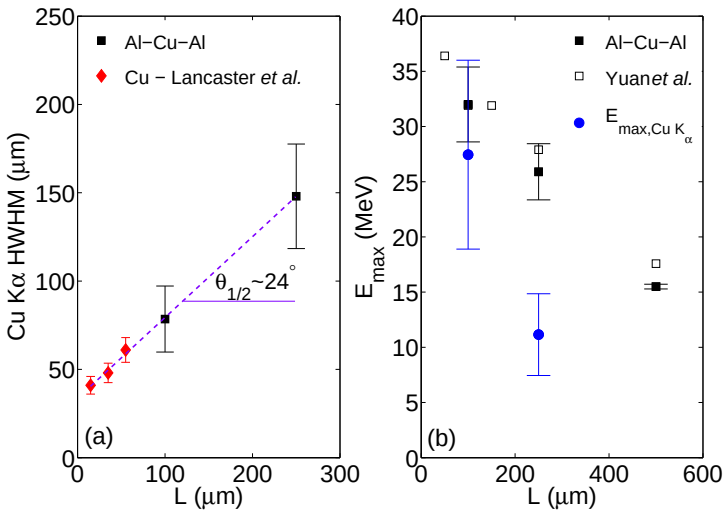

Figure 5.1: (a) Measured lateral extent of Cu Kα emission (HWHM) as a function of target thickness (front Al transport layer), L. Black symbols are data from the present experiment. Red symbols are measurements made with similar laser pulse parameters, reproduced from Lancaster *et al.* [14]; (b) Maximum proton energy, E_{max}, as a function of target thickness. Black symbols are data from the present experiment and black circles are measurements made with similar laser pulse parameters, reproduced from Yuan *et al.* [186]. Blue circles are theoretical estimates of E_{max}, calculated using a plasma expansion model with the measurements of the lateral extent of Cu Kα emission shown in (a) used to estimate the rear-surface fast electron density.

5.3.1 Preliminary discussion

The simultaneous measurement of Kα fluorescence imaging, providing the lateral extent of the electron beam close to the target rear surface, and the measurements of proton acceleration, resulting from the electron-induced sheath field at the rear surface, represents a significant development over our previous investigation of electron transport which employed proton acceleration only (Yuan *et al.* [186]), and enables the consistency of the two diagnostic approaches to be checked. To do this, the electron beam radius inferred from the Kα measurements is used to determine the fast electron density at the target rear surface for model calculations of proton acceleration.

In a simplified model approach, the fast electron density is assumed to be constant over the beam volume, and is estimated as $N_f/(\pi r_{rear}^2 c\tau_L))$, where r_{rear} is the target rear-surface electron beam radius, c is the speed of light and the number of fast electrons, N_f, is determined as $\eta_{L-e}E_L(J)/(e.T_f[eV])$, where η_{L-e} is the laser-to-fast electron energy conversion efficiency, e the elementary charge and $T_f[eV]$ is the fast electron beam temperature. These parameters are used, together with an estimated ion acceleration time, t_{acc}, to calculate an expected maximum proton energy by employing the Mora 1D isothermal plasma expansion formula [136] $E_{max}[eV] = 2T_f[eV]\left[\ln(t_p + (t_p^2+1)^{1/2})\right]^2$. The normalized acceleration time $t_p = \omega_{pi}t_{acc}/(2\exp(1))^{1/2}$, with the ion plasma frequency $\omega_{pi} = [(Z_i e^2 n_f)/(m_i\epsilon_0)]^{1/2}$, where m_i and Z_i are the proton mass and charge number respectively. The ponderomotive scaling [63] is assumed, giving a fixed T_f equal to 6 MeV, for a peak laser intensity equal to 4×10^{20} W/cm^2 and wavelength, λ_L, equal to 1.054 μm. The ion acceleration time is selected as the laser pulse duration, based on the principle that to first order this is set by the duration of the electron bunch arriving at the target rear side. The main unknown parameter is η_{L-e}, which is expected to be in the range 0.1-0.5 [84] for the laser intensity and other pulse parameters of this study - the wide range is due to it's sensitively to the laser intensity and the density scale length of the preformed plasma on the target front side [78, 187]. Moreover, recent PIC simulations reported by Scott *et*

al. [78] showed a significant increase of the p-polarized laser spot size, focused at an incident angle of 45° with respect to the target normal, near the target front surface due to the refraction of the laser through the preformed plasma. It was also found that reducing the angle of incidence reduces the laser spot size near the target front surface. The experimental results presented were obtained at a laser pulse contrast ratio of $\sim 10^9$ on a ns time scale, minimizing the preplasma density scalelength at the target front surface, and an incident angle smaller than the one used in [78]. Thus the electron source diameter is set equal to the laser vacuum focal spot diameter in this study in the hybrid simulations.

Figure (5.1(b)) shows the resulting calculated maximum proton energy for L=100 μm and 250 μm with η_{L-e}=0.5. The absolute values are not important as these depend on the selected η_{L-e} and the other unmeasured parameters, except to note that within the expected ranges of these parameters a good match can be found to the measured E_{max}, particularly in the case of the thinner target. However, it is found that the percentage decrease in the maximum proton energy calculated using the electron beam radii from the Kα fluorescence measurements, from L=100 μm to L=250 μm, is much larger than the measured decrease. This apparent inconsistency in the two diagnostic approaches may result from the simplified assumptions applied in the calculation or may arise due to the fact that Kα fluorescence can be induced by electrons with energies as low as 50 keV, and therefore the two diagnostics are probing the transport of electrons with different energy ranges.

Based on this first experimental analysis, using the proton maximum energy as a diagnostic of the fast electrons, the 3D hybrid code is used to simulate the experimental parameters to deduce n_f and t_{acc}.

5.4 3D hybrid code ZEPHYROS

This section presents the numerical simulations performed to infer the initial divergence (injection) and transport half-angles using the 3D hybrid code ZEPHY-

ROS, introduced in the methods chapter (4). The resulting electron density and other parameters obtained from the numerical simulations are used to calculate the maximum proton energies for comparison with experiment.

The numerical work of Davies [107] compares the energy lost by fast electrons for given fast electron energy distribution, in ultra high intensity laser ($I \sim 10^{18}$ W/cm^2)-Al and plastic (of thickness ~200 μm) targets interactions, inferred from numerical results using a hybrid Monte Carlo code in which self-generated resistive fields are first suppressed (i.e. the fast electrons only interact with the background via the drag and the random rotation terms) and then included. Even though the study by Davies is made at lower laser intensity than the study presented here, the code and the rest of the simulation parameters used in this work are similar to the hybrid and parameters described in [107], and so the conclusions of [107] can serve as a guideline to this numerical study.

The main conclusions of Davies work [107], using a similar hybrid code, relevant to this study are :

- The fast electron generation depends on many interlinked parameters, such as the background resistivity and the simulation boundary conditions. Therefore hybrid codes, using a *given* hot electron distribution function, can't model properly the fast electron generation mechanism.

- The fast electrons rapidly heat the background (by drawing a collisional return current) to high temperature, changing the background resistivity and thus affecting resistive B-fields and resistive transport instabilities.

- The E-field act to slow down the electrons as they lose their energy to the field (Ohmic stopping). The B-field deflects the electrons changing their trajectory. It affects more strongly the low energy electrons. It also reduces the penetration depth of the low energy electrons by increasing the curvature of their trajectory. On the contrary, it can increase the penetration depth of high energy electron by reducing their initial angle to the axis.

- Because the penetration depth of the low energy electrons is shortened due to the magnetic field deflecting or turning them around, only the high energy electrons can be sampled at large depths in the simulation box. Thus the apparent mean energy of the fast electrons is increased and the absorption decreased.

- By comparison of the B-field generated in Al and plastic targets, it was found that the B-field strength is higher in Al due to the resistivity of Al increasing with the background temperature. This leads to a separation between the forward fast electrons and the return currents propagating around the fast electron beam in a lower resistivity region. In plastic, the fall of the resistivity with increasing temperature lowers the B-field strength and thus the return current propagates close to the axis with the forward fast electron beam circling it. This effect leads to a hollowing within the fast electron beam, and therefore a 'ring-like' beam pattern.

- Finally, Davies shows, in agreement with the observations of Wharton [5], that the change in the atomic number Z of the target does not affect the laser-to-electron energy conversion efficiency, but does affect the beam mean energy when comparing CH and Al targets. By comparing the mean energy obtained with Cu and Al targets, Wharton [5] further shows that the electrons produced in Cu are the most penetrating, although Al and Cu spectra are equivalent within the measurement error bars.

Batani *el al.* [188] summarized, with parameters relevant to fast ignition, the collisional and collective fast electron beam propagation in different Z targets. By comparing the electron stopping power due to collisions to the Ohmic stopping scale length, it is found that when increasing Z from CH to Al to Au that the stopping power due to collision increases (since the stopping power increases with target Z and density) and the E-field inhibition decreases (as the E-field strength decreases with increasing target conductivity).

5.4.1 Simulation results for Al targets

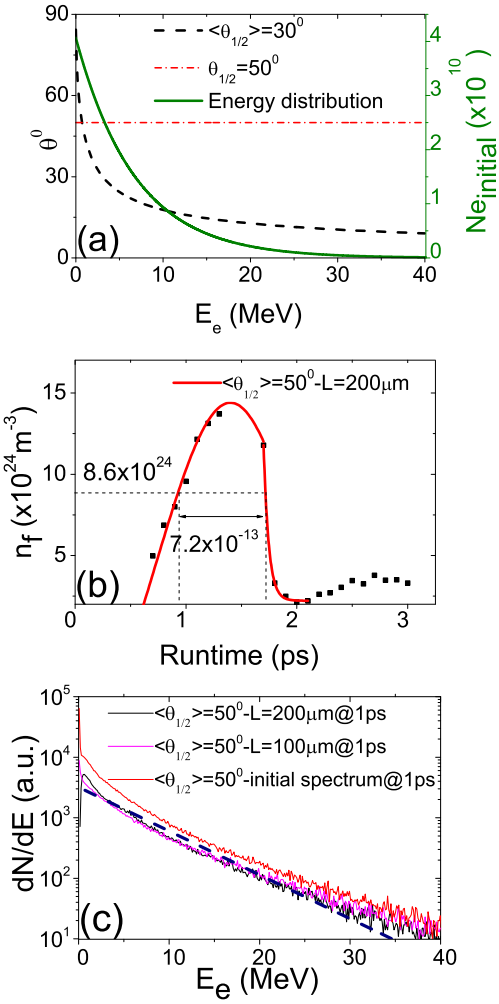

Figure 5.2: (a) Fast electron beam injection half-angle as a function of electron energy. The dashed black curve is the distribution function derived by Moore *et al.* [60], in which $\theta_{1/2} = \tan^{-1}[\alpha \times \sqrt{2/(\gamma - 1)}]$, where γ is the electron relativistic factor and with $\alpha = 1$ giving a mean half-angle $< \theta_{1/2} > \sim 30°$ in the example shown. The red line corresponds to electrons injected uniformly within a cone with half-angle equal to 50°. The green curve is the initial fast electron energy spectrum for a beam temperature of 6 MeV; (b) Example temporal evolution profile of the maximum fast electron density at the target rear side, extracted from a hybrid simulation of electron transport within a 200 μm-thick target, with $< \theta_{1/2} >= 50°$; (c) Fast electron energy spectra extracted from the hybrid simulations at the rear side of 100 μm and 200 μm-thick targets.

The simulations were performed using a 500 μm $\times$ 500 μm $\times$ L μm box with grid size equal to 2 μm $\times$ 2 μm $\times$ 2 μm. Few runs were made using a higher resolution equal to 1 μm $\times$ 1 μm $\times$ 1 μm to investigate fine-scale instabilities in the fast electron beam density profile and the self generated magnetic field. L is the target thickness, and a lower limit of 75 μm is set by the fact that significant fast electron refluxing effects are observed for simulations with thinner targets, which prevents accurate determination of the electron density at the target rear surface. The upper L limit is set by computational limitations.

In a typical set of simulations, runs were performed for L=75, 100, 150, 200 and 250 μm. The fast electron source input parameters which were fixed were chosen to match the experiment parameters. The beam temperature was set equal to $\sim$ 6 MeV (given by ponderomotive scaling [63]), and the electrons were injected into the solid over a pulse duration of 1 ps, in a focal spot (Gaussian transverse profile & top hat temporal profile) with radius equal to 4 μm. The two variable electron source parameters are η_{L-e} (and hence the number of fast electrons N_f) and the angle of injection.

The electron energy distribution, shown in figure (5.2(a)), is given by $N_f(E_e) = N_f exp(-E_e/T_f)$, where E_e is the electron energy and T_f is the initial electron beam temperature. The electrons were injected within a cone with mean injection half-angle $\theta_{1/2}$, in one of two angular-energy distribution functions shown in figure (5.2(a)). For most of the simulation runs the angular-energy injection distribution derived by Moore *et al.* [60] was used: $\theta_{1/2} = \tan^{-1}[\alpha \times \sqrt{2/(\gamma - 1)}]$, where γ is the electron relativistic factor and α is the factor used to vary $< \theta_{1/2} >$ (α=1 corresponds to the angle at which electrons are ejected from the laser focal spot by the ponderomotive force).

The fast electrons with energy E_e were injected within the cone of half-angle $\theta_{1/2}(E_e)$. For a limited number of simulation scans, the electrons were injected uniformly into a cone with a fixed injection half-angle of 50°, for comparison. The model of resistivity as a function of temperature for Al used in the code is the one used previously by Davies [107], based on a fit to the data reported by Milchberg *et al.*[48].

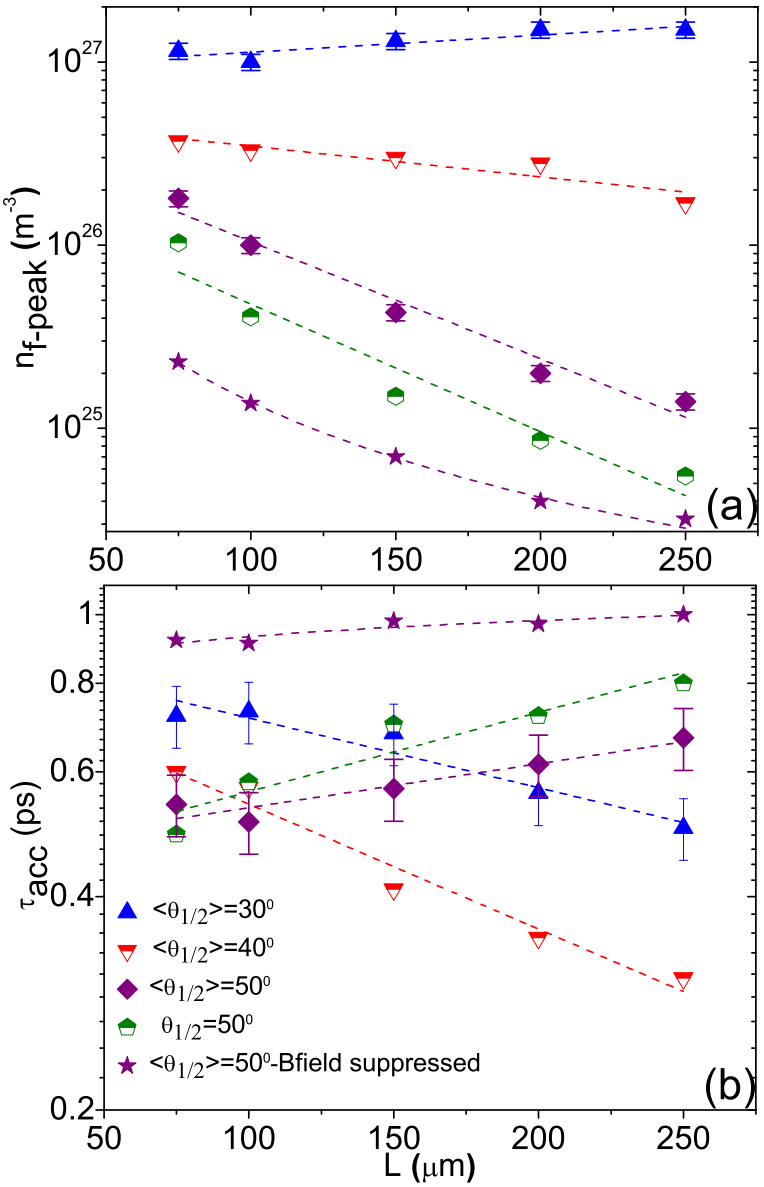

Figure 5.3: (a) Maximum fast electron density, time-integrated over the temporal peak, as a function of target thickness L, extracted from the hybrid simulations; (b) Corresponding 'ion acceleration time', as extracted from the temporal width of the density peak, as a function of L.

The initial background temperature was set at 1 eV, giving an initial Al resistivity of $\sim 1.9 \times 10^{-7}$ Ωm. The front and rear boundaries are reflective and side boundaries are open.

The fast electron density, n_f, and the ion acceleration time, t_{acc}, as required in application of the plasma expansion formula [136] to calculate E_{max}, were determined from the simulation results, as follows. The maximum fast electron density at the rear side of the target (typically on-axis) was plotted as a function of the simulation run time, as shown for the example in figure (5.2(b)). Typically the electron density builds up over about half a picosecond to a peak value and then drops quite rapidly as fast electrons are reflected back into the target. In thin targets a secondary smaller density peak is sometimes observed at a later point in time when the refluxing electron population returns to the rear side. A time-averaged value for n_f was measured over the width of the main peak in the density-time profile, hereafter referred to as n_{f-peak}, and the FWHM duration was used for t_{acc}.

In addition to n_{f-peak} and t_{acc}, the beam temperature, T_f, is a third variable in the plasma expansion calculation. For the range of simulation parameters modeled, we find that T_f at the target rear side is independent of target thickness and equal to the initial beam temperature.

Figure (5.2(c)) shows examples of the initial electron energy spectrum and the spectrum at the rear side of a L=100 μm and L=200 μm target. A fit of the form $\exp(-E_e/T_f)$ gives no measurable change in T_f, and hence this parameter was fixed at 6 MeV in the plasma expansion calculations that follow.

Role of injection angle and resistive magnetic fields in fast electron transport

A series of simulation runs were performed to investigate the sensitivity of fast electron transport to the injection angle at the source. $< \theta_{1/2} >$ was varied from 30° to 70° and the resulting n_{f-peak} and t_{acc} variations with L are determined. Example results are presented in figure (5.3). Generally, at a given L, n_{f-peak} de-

creases rapidly with increasing injection angle, which is expected due to increased lateral spreading of the electrons within the target.

For $< \theta_{1/2} >$=40° and above, n_{f-peak} decreases with increasing L, also due to increased lateral spreading as the electrons propagate further in the thicker targets. However, as the injection angle is decreased the resistive azimuthal B-field produced at the edge of the beam, and shown in the example 2D profiles in figure (5.4(a,b,c)), acts over a longer beam propagation length within the target, and in the case of $< \theta_{1/2} >$=30° acts to pinch or collimate the electrons, as can be seen in n_f 2D profiles shown in figure (5.4(d,e,f)), over the full simulation box.

The effect of the self-generated B-field is further investigated by performing comparative simulations with the field turned off in the code.

As shown in the example results in figure (5.6), even in the case of the relatively large $< \theta_{1/2} > \sim 50°$, the B-field strongly affects the electron density distribution within the beam and in particular the maximum electron density at a given depth in the target - note the logarithmic scale in electron density in figure (5.4).

n_{f-peak} at the target rear side is approximately an order of magnitude lower when the B-field is suppressed, irrespective of target thickness, as shown in figure (5.3(a)).

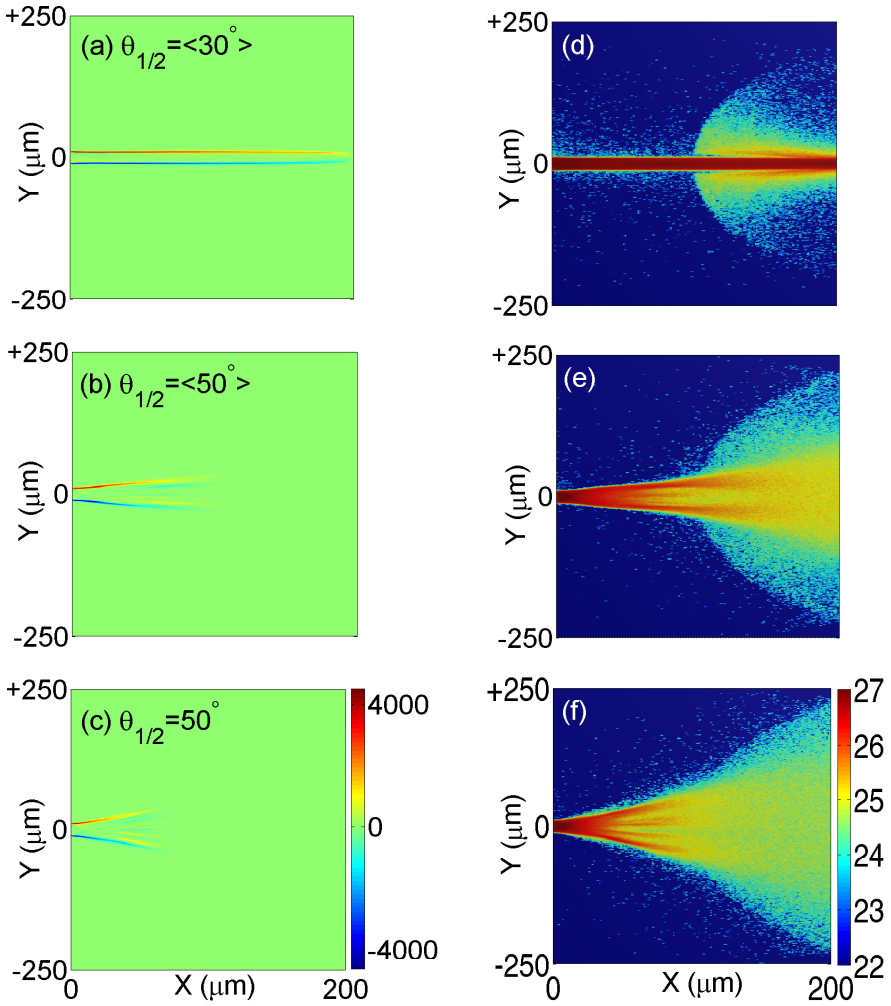

Figure 5.4: (a)-(b)-(c) False-colour 2D maps of the z-component of the self-generated resistive B-field (in units of Tesla); (d)-(e)-(f) False-colour 2D profiles of the fast electron beam density ($\log_{10}$ (m^{-3})): For a 200 μm-thick Al target and 1 ps runtime, at given injection half-angles specified in (a)-(b)-(c). The fast electrons are injected at position (0,0,0) and the beam propagates in the direction of the x-axis. The grid size for this set of simulations was equal to 1 μm $\times$ 1 μm $\times$ 1 μm.

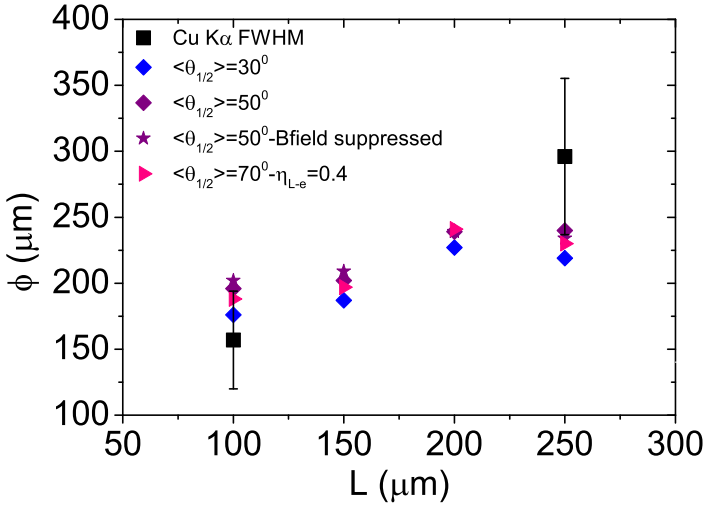

Figure 5.5: Fast electron beam diameter, ϕ, as a function of target thickness. Black squares correspond to the experimental data. Colored symbols correspond to the lateral extent of the electron beam as measured in the simulations for given injection parameters. Unless otherwise stated the B-field evolution is 'on' and η_{L-e}=0.2. The beam size is extracted from the simulation results before refluxing at the rear surface boundary at a runtime of 0.4 ps for $L = 100$ μm, 0.6 ps for $L = 150$ μm, 0.9 ps for $L = 200$ μm and 1 ps for the $L = 250$ μm.

Figure (5.5) compares the lateral extent of the fast electron beam distribution at the target rear side as determined from the simulation results, with the measured lateral extent of the Cu $K\alpha$ emission. In this comparison the overall envelope of the electron beam is considered, due to the variations in density that can result within it (figure (5.4) & (5.6)) and the fact that Cu $K\alpha$ fluorescence can be induced by relatively low energy electrons at the edges of the beam. Despite the large variations in n_{f-peak} resulting from the different injection angles and the effect of the B-field (figure 5.3(a)), at a given L the overall spatial extent of the beam is largely independent of these parameters. Therefore, although the results are in quite good agreement with the measurements for L=100 μm and 250 μm, no conclusion can be drawn regarding the electron beam injection from

this diagnostic.

Instead, below, the proton diagnostic measurements is used to extract this information. As shown in figure (5.3), the simulation results further reveal correlations between the peak electron density and the time duration over which it evolves (and therefore, in effect, the ion acceleration time).

Generally, and especially in the case of the thickest target, for low values of $< \theta_{1/2} >$ at which a high n_{f-peak} is achieved (due to the pinching effect of the B-field), the peak temporal width is small (i.e. fast rise and fall in density), whereas a lower peak density is associated with a 'wider' peak and hence larger t_{acc}. These correlations suggest that the resistive B-field not only affects the fast electron density distribution within the beam, but also the temporal evolution of the resulting sheath field.

For most of the simulation runs t_{acc} falls between 0.5 and 1.0 ps.

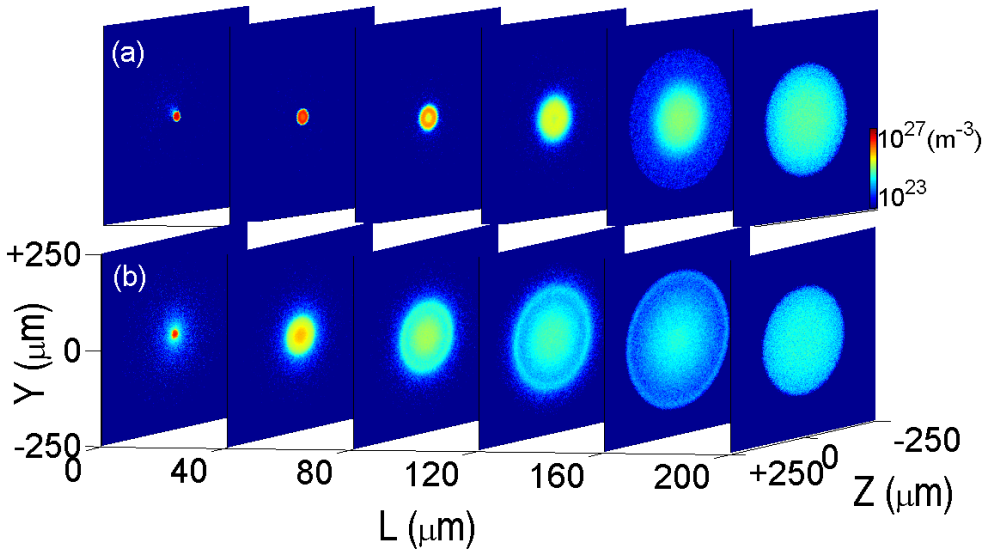

Figure 5.6: (a) False-colour 2D profiles (log scale) of the fast electron density distribution at given depths for a 200 μm-thick Al target for $< \theta_{1/2} > \sim 50°$ and 0.8 ps simulation time; (b) Same as (a), but with the B-field artificially suppressed.

Resulting calculated maximum proton energies

As discussed above, the values of n_{f-peak} and t_{acc} extracted from the simulation results are used as input parameters to the Mora plasma expansion model to obtain a theoretical maximum proton energy (E_{max}) for comparison to experiment. Application of this expansion formula requires that the fast electron density profile should be uniform in the plane normal to the proton motion. Although, as shown in our simulation results, the density distribution is non-uniform, the variation of the density in the region of the peak is small (of the order of a few percent) over a radius of the order of the Debye length, and hence the electron density can be considered to be locally uniform in the region where the fastest protons are produced. The calculated E_{max} for a range of simulation runs are presented in figure (5.7), together with the experimental results (from figure (5.1(b))). In figure (5.7(a)) the laser-to-electron energy conversion efficiency, η_{L-e}, is fixed at 0.2 and the injection angle, $< \theta_{1/2} >$, is varied. Due to the pinching effect of the B-field, the predicted proton maximum energies for the smaller injection angles is much larger than the measured E_{max}. This suggests that the electrons are injected into a cone with a relatively large angle at $\sim 50°$. Figure (5.7(b)) presents the case for which η_{L-e} is again fixed equal to 0.2 and the effects of suppressing the resistive B-field are shown. In the absence of the B-field the correct order of magnitude for E_{max} is obtained even for a relatively small $< \theta_{1/2} >$=30°, but the percentage decrease in E_{max} with increasing L is much larger than experiment. Due to the fact that η_{L-e} is an unknown variable parameter which changes the absolute value of the theoretical E_{max}, it is not the absolute values that should be compared, but rather the shape of the E_{max}-L profile. For the simulation results presented in figure (5.7(c)) both $< \theta_{1/2} >$ and η_{L-e} are varied to produce calculated proton maximum energies in the range of the experimental measurements (i.e. η_{L-e} is increased with $< \theta_{1/2} >$ to provide a better comparison to experiment). It is found that the closest fit to the measured E_{max}-L profile is found for the largest injection angle, $< \theta_{1/2} >$=70° and η_{L-e}=0.4.

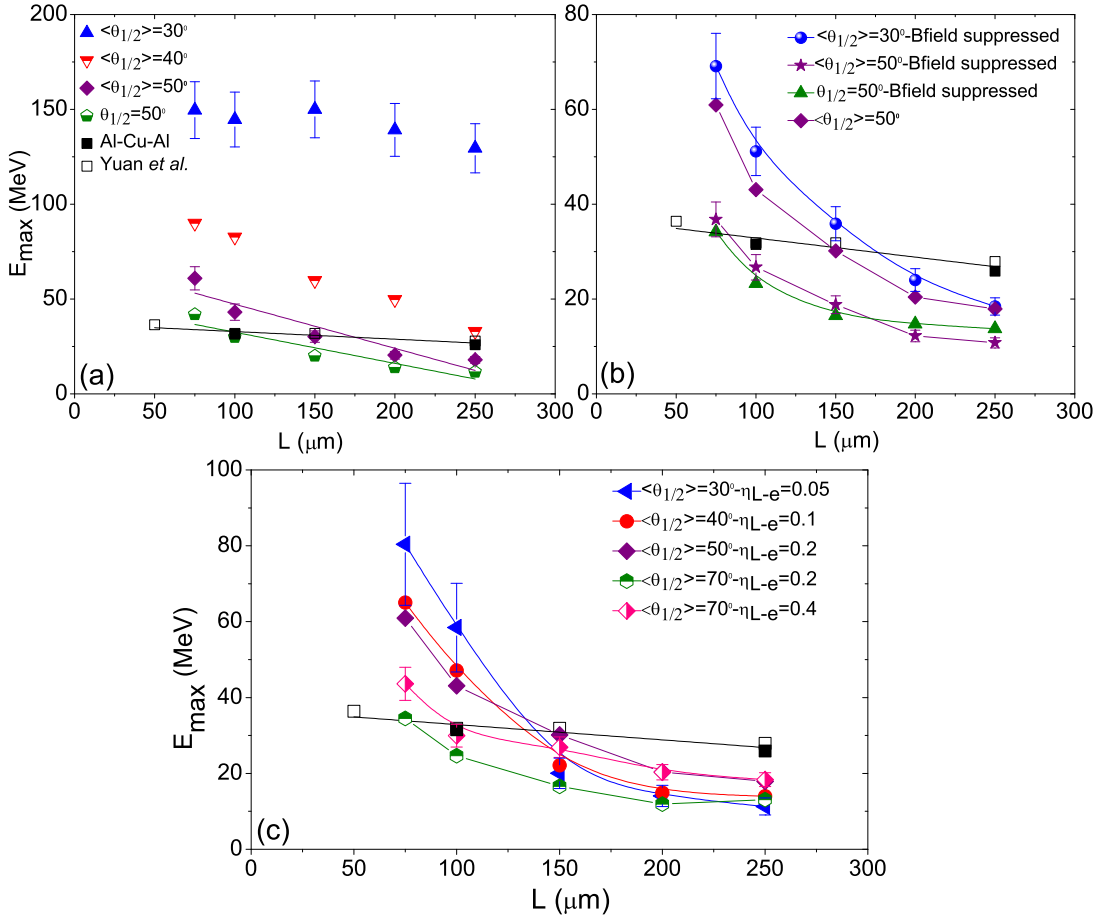

Figure 5.7: Maximum proton energy as a function of L. Black squares are the experiment data. Colored symbols are plasma expansion model calculations of E_{max} using electron densities and acceleration times deduced from the hybrid simulation results: (a) for fixed η_{L-e}=0.2 and given injection half-angles, $< \theta_{1/2} >$; (b) illustrating the effect of B-field suppression (for fixed η_{L-e}=0.2 and given $< \theta_{1/2} >$); (c) for given η_{L-e} and $< \theta_{1/2} >$.

5.4.2 Discussion

The Kα fluorescence measurements obtained using Al-Cu-Al layered targets, which are sensitive to the overall lateral extent of the electron beam, indicate that the effective transport half-angle is between 8° and 32° as defined by the degree of uncertainty in the measurements (best fit $\sim 24°$), and this is supported by the simulation results. The hybrid simulations in Al targets further reveal that the density profile within the beam is strongly affected by self-generated magnetic fields, which in turn are sensitive to the average injection angle of the electrons at the front side of the target. The numerical simulations show that the initial beam divergence is larger (half-angle between $\sim 50 - 70°$) than deduced from previous studies [14, 15].

5.5 Variation of target Z and laser spot size

Experimental results corresponding to Au and Al_{60} are presented in figure (5.8) & (5.9).

The Cu Kα FWHM shows only small variations, at a given L, between Al_{60} and the signal obtained for Al-$CH_{\phi_L=35}$ and Al-$CH_{\phi_L=60}$. A divergence half angle of $\sim 33° \pm 7°$ is inferred from a linear fit to the Cu Kα lateral extent for Al_{60}. Using the CH at the target rear surface, it was established that although refluxing can increase the total Cu $K\alpha$ yield, it has only a very small effect on the size of the $K\alpha$ image, in agreement with previous work reported by Quinn *et al.* [189]. The CH layer was not used for the main set of results because it strongly affects rear-surface proton acceleration and thus prevents the $K\alpha$ and proton emission diagnostic approaches being simultaneously applied.

The decrease in E_{max} with increasing L for Au, compared to Al, seems to be steeper for the same laser irradiance. It can also be noticed that the rate of change in E_{max} with increasing L for Al-Cu-Al seems to be quicker, when compared to Al_{60}.

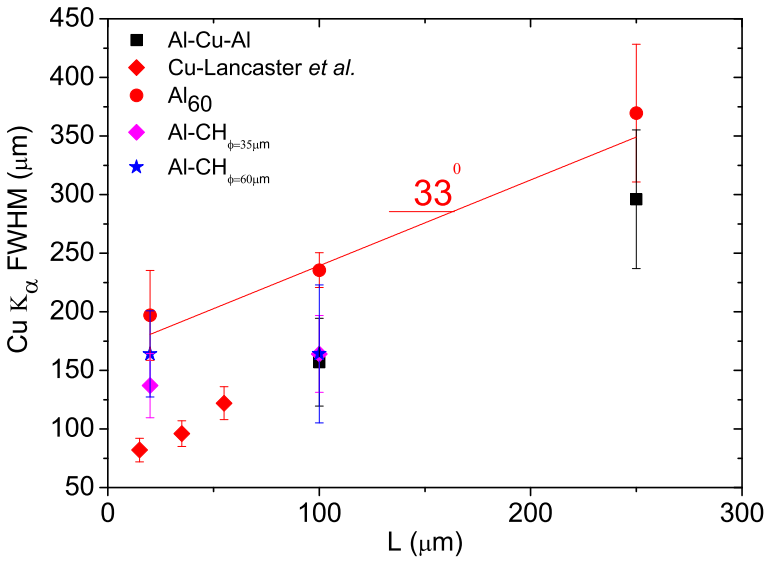

Figure 5.8: Measured lateral extent of Cu Kα emission (FWHM) as a function of target thickness.

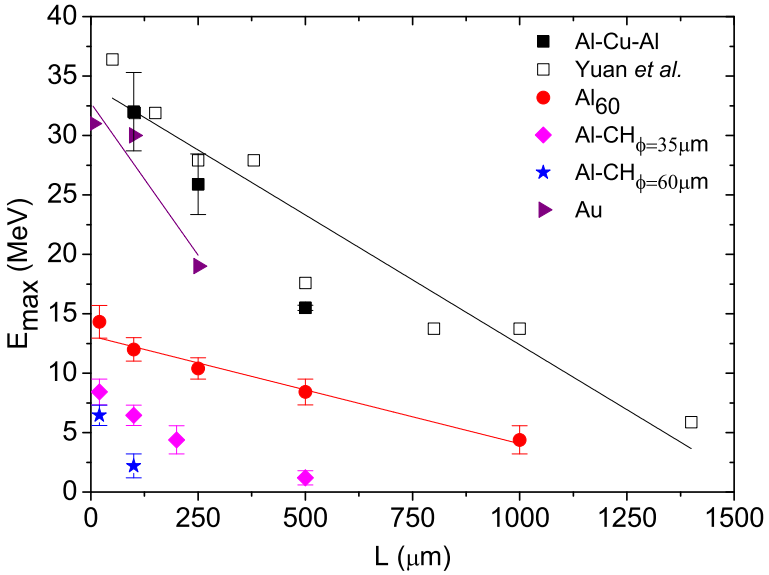

Figure 5.9: Maximum proton energy, E_{max}, as a function of target thickness.

5.5.1 Comparison of fast electron beam transport in Au and Al targets

Based on published work comparing electron transport in different Z material targets and thicknesses, discussed in subsections (5.1), and by comparing the collisional and radiative stopping power of electrons [93], the fast beam transport in Au is expected to be dominated by collisional processes, in particular for thick targets.

The results obtained using two simulation codes (Monte Carlo & hybrid codes) to model the beam transport in both Au and Al are presented below. The theoretical maximum proton energies achieved using the simulation outputs as input to Mora's plasma expansion model are then presented.

Numerical Simulations results

To model the scattering of the fast electron beam in Au and Al, a series of simulations using the GEANT4 Monte Carlo code [190] were performed. The runs, for a simulation box size varying from 20 to 1000 μm, were made on monoenergetic electrons of energy equal to 6 MeV for Al-Cu-Al and Au, using GEANT4- low energy electromagnetic physics: G4eMultipleScattering, G4eIonisation, G4eBremsstrahlung. The energy of fast electrons is set equal to 400 keV for the Al_{60} runs due to the reduced laser intensity. This set of runs is used to estimate the fast electron spatial distribution in Al and Au at a specific electron energy set equal to the fast electron mean beam energy of the energy distribution (6 MeV or 400 keV). Thus the spot size extracted at the simulation box rear boundary underestimates the beam size because the low energy electrons (experiencing more scattering in the solid) from the energy distribution are not modeled.

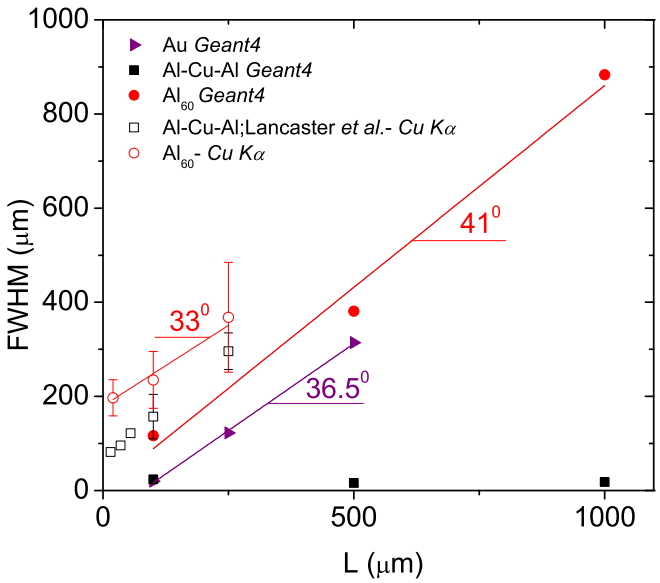

Figure 5.10: FWHM of the electrons distribution at the rear of the simulation box for the three experimental configurations as function of the simulation box length.

This first modeling shows a larger beam spreading in Au compared to Al-Cu-Al, as shown in figure (5.10). This is accounted for by the angular broadening [17] of the fast electron beam due to scattering in this higher Z target, which increases with the target thickness. The fast electrons in the Al_{60} case scatter more than for Al-Cu-Al because their mean temperature, scaling with the laser intensity, is lower as I_L is lower. Finally, the scattering does not affect the electron beam size in the Al case at best focus (T_f=6 MeV). Note that the electron spot size in the Al_{60} targets, extracted from Geant4 runs, is in general smaller at a specific L than the experimentally measured size of the Cu $K\alpha$ emission (∼100s keV electrons).

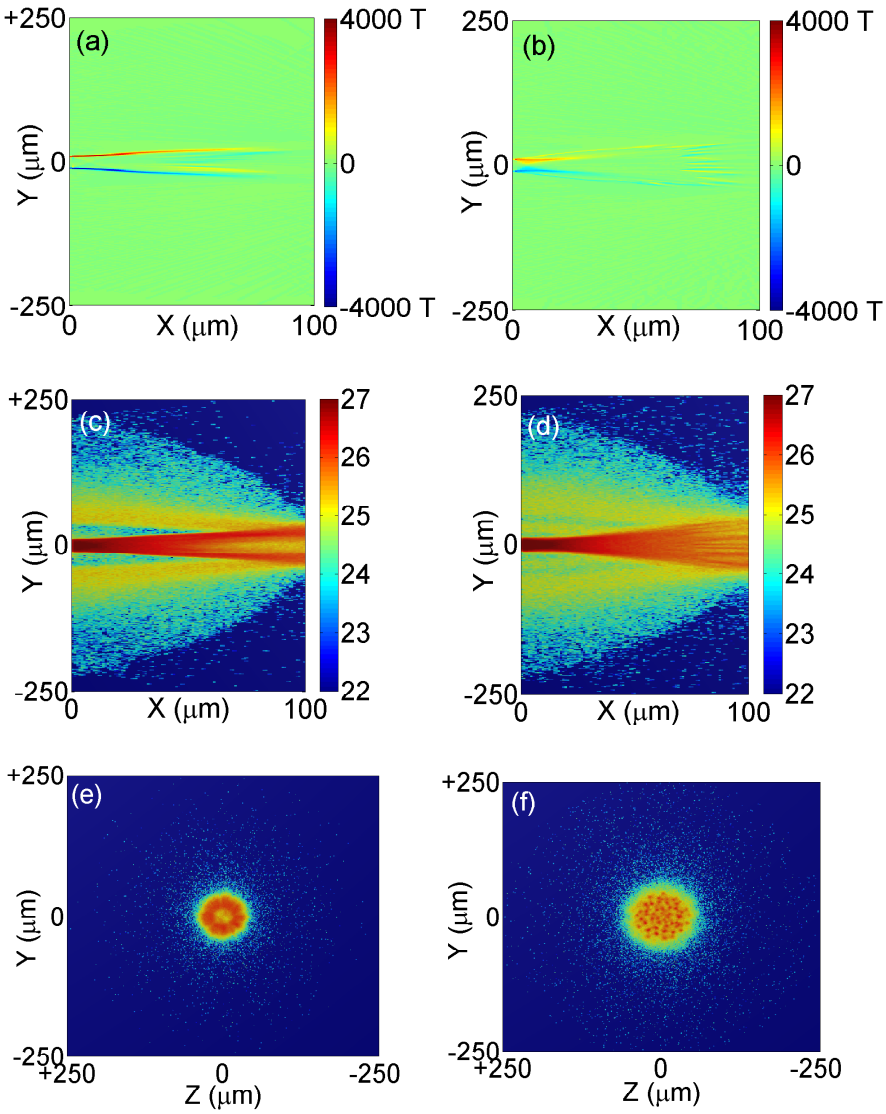

Figure 5.11: False-color 2D profiles of the z component of the B-field (a,b); the fast electron density distribution ($\log_{10}$ (m^{-3})) (c,d); the density distribution at the rear of the simulation box (z-y axis) (e,f); for 100 μm-thick Al (left) and Au targets (right). The example results shown are for a simulation time of 1 ps, $< \theta_{1/2} >$=50° and η_{L-e}=0.2 at 1 ps runtime. The Au resistivity curve published in Key [191] is employed.

As for Al-Cu-Al targets, hybrid-PIC simulations were performed in Au targets to model the beam transport, including self-generated fields. The simulation box thickness L was equal to 75, 100, 150, 200 and 250 μm. The Au resistivity curve shown in Key [191] was employed. The input parameters used in this set of runs were similar to the ones used for the Al-Cu-Al targets. Unless specified, the laser-to-electron energy conversion efficiency used in the hybrid runs was equal to 0.2. Example results obtained using the hybrid code to probe the effect of the fields on the beam propagation in Au, compared to Al, are shown in figure (5.11). The rear beam density and the acceleration time, deduced from the simulations, are presented in figure (5.12). n_{f-peak} in Au targets decreases with increasing L and t_{acc} fluctuates little around ~0.75 ps. Note that n_{f-peak} in Au targets, is lower than in Al targets for $L < 150$ μm and tend to converge for thicker targets. By comparing the beam spectrum obtained after 100 and 200 μm-long simulation box in Au targets, no clear change in the beam mean temperature is observed.

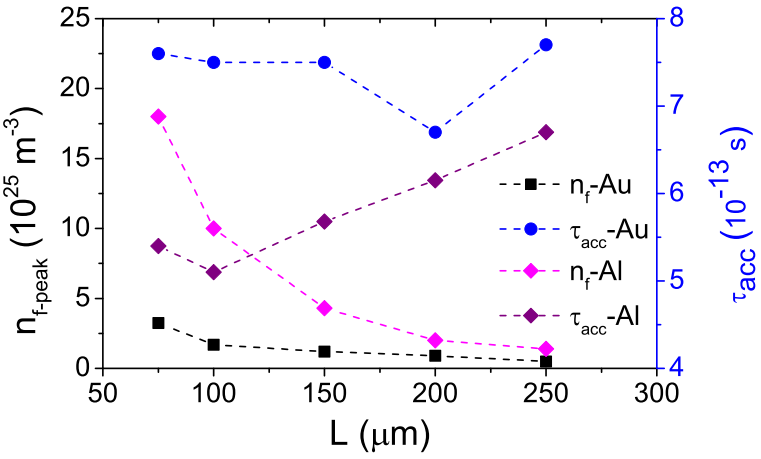

Figure 5.12: $n_{f,peak}$ and τ_{acc} deduced from ZEPHYROS (using the resistivity curve published in Key [191]) as function of L, in Au target, with $< \theta_{1/2} >$=50°. The results are compared to those obtained for Al target.

Numerical simulations could not be fully performed using a large electron source radius. This needs additional computational resources than available to

our group at the time of writing. However, scans in thickness were performed at a source radius equal to 8 and 16 μm for comparison to tight focus. Figure (5.13) compares the magnetic field and the corresponding fast electron density distribution for different spot size. As predicted by Bell *et al.* [24], the increase in the source size (thus, the decrease in the laser intensity) leads to a fall in the magnetic field strength, and, consequently to a fall in the rear beam density. The effect of the source spot size on the beam injection and propagation is also investigated in the next chapter.

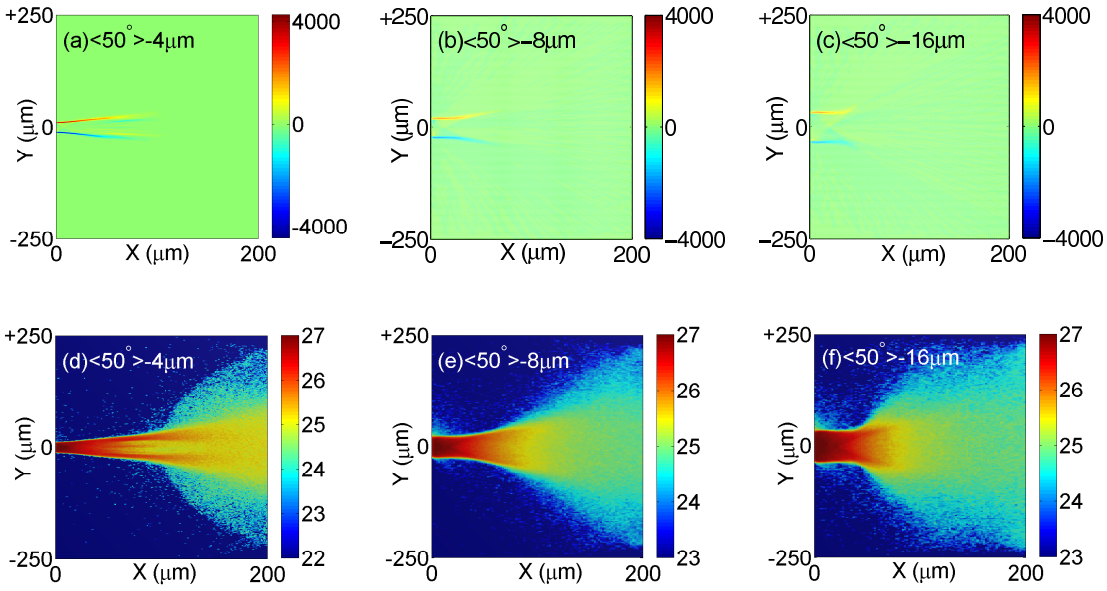

Figure 5.13: (a-c) False-color 2D profiles of the z-component of the self-generated resistive B-field (in units of Tesla);(d-f) Corresponding false-color 2D profiles of the fast electron beam density ($\log_{10}$ (m^{-3})). The plots are for a 200 μm-thick Al target and 1 ps runtime, at given injection half-angles and source spot radius specified in the legend.

Resulting E_{max} from analytical model

To begin with, the Cu $K\alpha$ emission spot radius (r_{rear}) and the Mora's isothermal model are used to predict the proton maximum energy, shown in figure (5.14), for comparison with Al_{60} experimental results, as the $K\alpha$ emission diagnostics have not been used during the experimental campaign using Au targets. The mean temperature is kept equal to its initial value. A good match is found for Al_{60} using η_{L-e}=0.5 and τ_{acc}=5 ps.

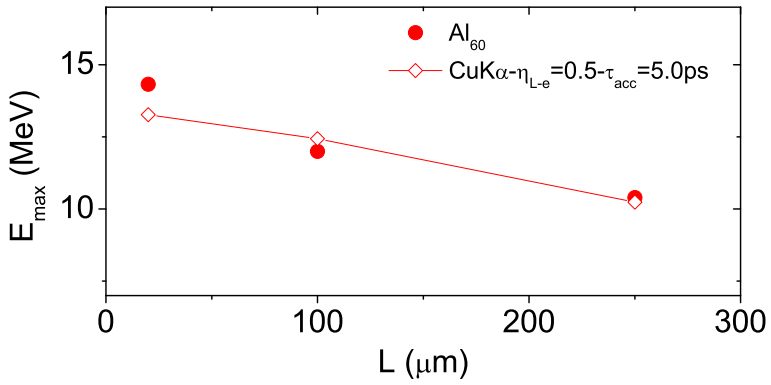

Figure 5.14: E_{max} as a function of L using the X-ray lateral extent measurements to infer the fast electron rear density used as input parameter in the Mora's isothermal model.

The value for τ_{acc} suggests that even by increasing η_{L-e} to 0.5 the accelerating field should last much longer than the laser pulse duration (i.e. the isothermal plasma expansion should be maintained for a duration much longer than τ_L) in order to reproduce the experimental E_{max} at a peak laser intensity of $\sim 5.5 \times 10^{18}$ W/cm^2.

Resulting E_{max} from Numerical simulations

The fast electron peak density and the ion acceleration time, extracted from the hybrid simulations of beam transport in solid Au targets, are used as input to the isothermal model to enable a calculation of E_{max}. Figure (5.15) shows the E_{max} obtained using the parameters determined from the ZEPHYROS simulations in Au targets (using the resistivity curve of Key [191]). As for Al targets, a large injection half angle is required to obtain an E_{max} trend close to the experiment. Note that similar E_{max} trends are obtained for $< \theta_{1/2} >$=50°, with and without including the B-field. Furthermore, as can be observed in figure (5.11(e-f)), close beam diameters are obtained in Au and Al, at the rear of the simulation box. Therefore, no clear conclusion can be drawn from the numerical simulations regarding the beam scattering.

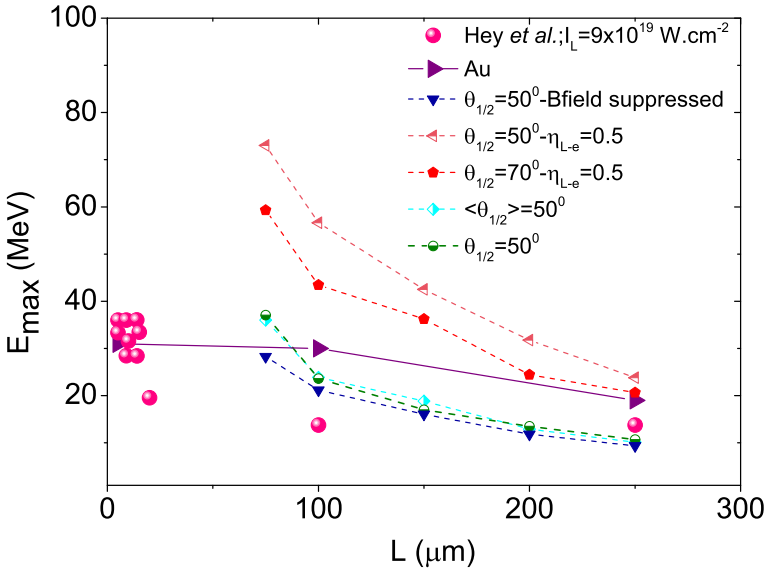

Figure 5.15: E_{max} as a function of L using the numerical simulation results from ZEPHYROS, in Au targets, to determine electron density and acceleration time as inputs in the Mora's isothermal model.

The proton maximum energy obtained in sub 20 μm-thick Au targets presented in this work at laser intensity equal to $\sim 4 \times 10^{20}$ W.cm^{-2} is comparable to the values published in Hey *et al.* [183], obtained in sub 20 μm-thick Au targets and at intensity $\sim 9 \times 10^{19}$ W.cm^{-2}. Hey *et al.* observed a constant proton cutoff energy around 35 MeV for sub 20 μm-thick targets, a similar plateau is observed in Au targets up to 100 μm-thick targets.

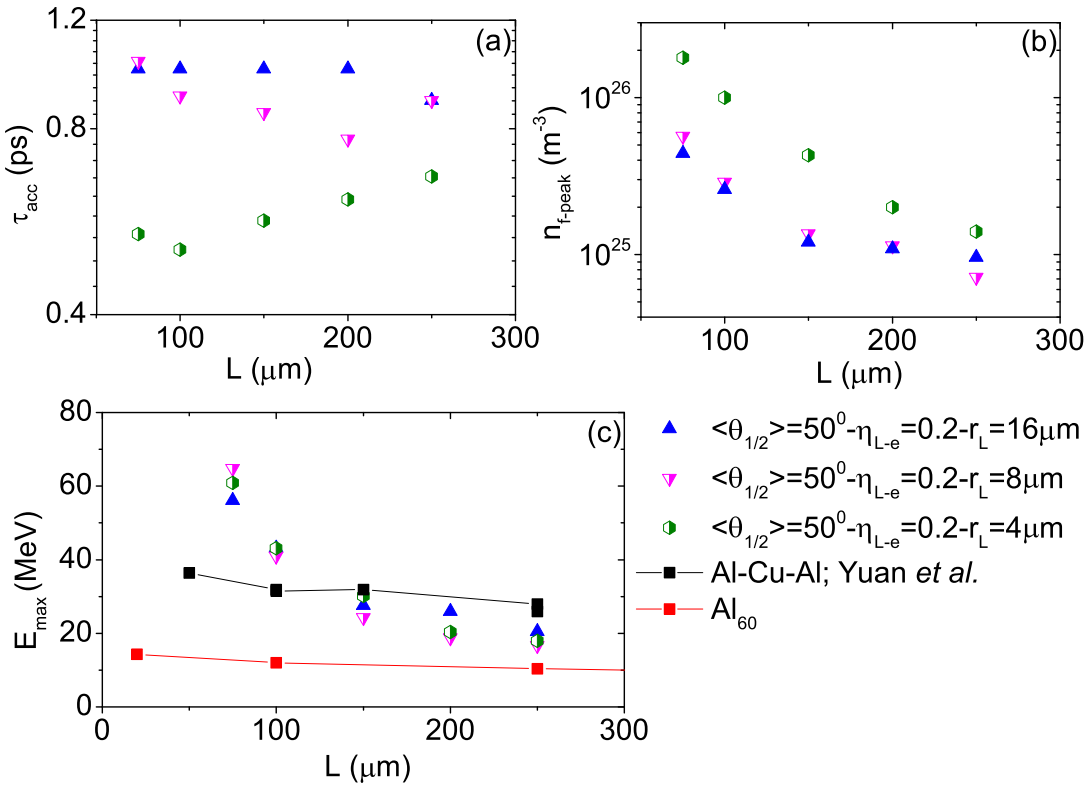

Figure 5.16: (a) The ion acceleration time (temporal width of the electron density peak) ; (b) the electron density peak; and (c) the maximum proton energy, all as a function of target thickness in Al targets.

The numerical results, obtained at larger spot size are presented in figure (5.16). The source sizes used in those simulations are smaller than Al_{60} spot size, however the numerical results enable to infer E_{max} trend obtained generally with source sizes bigger than the optimum tight focus. A similar maximum proton

energy trend with L is obtained for the three numerical scans. As the rear density decreases and the ion acceleration time increases at large spot size, no clear conclusion can be drawn from those numerical simulations.

5.6 Summary & future work

The injection and transport divergence properties of a high current beam of energetic electrons in Al and Au targets irradiated by ultraintense, picosecond laser pulses is investigated using simultaneous measurements of Kα fluorescence imaging (for Al-Cu-Al targets) and proton acceleration, and a programme of Geant4 and 3D hybrid-PIC simulations.

A comparison of the measured maximum proton energies with plasma expansion calculations, performed using parameters extracted from the hybrid simulations in Al and Au solid targets, indicates that the injected beam divergence at the source is significantly larger (half-angle between $50 - 70°$) than inferred from previous studies performed with similar laser and target parameters. Those results support the predictions by Honrubia and Meyer-ter-Vehn [26] and the recent study by Solodov *et al.* [128] that suggest that the fast electron initial divergence angles are actually quite large. This indicates that strategies for controlling fast electron beam collimation are therefore likely to be important for Fast Ignition.

Moreover, Geant4 simulations used to estimate the effect of collisional processes on the fast electron beam propagation, show that the angular broadening of the fast electron beam in the Au target, due to scattering, is significantly larger when compared to the Al target. Consequently, the fast electron beam density at the rear of the simulation box is slightly lower in Au targets. The difference in the fast electron beam density can explain the lower experimental proton maximum energies obtained in high Z material.

Future work would include numerical simulations for larger spot sizes to enable a better comparison with the experimental results. The choice of the resistivity curve model can be a critical parameter to accurately model the beam resis-

tive transport in overdense medium. A comparison between different resistivity models would also complete this work.

Chapter 6

Influence of laser irradiated spot size on fast electron generation and transport, and proton acceleration

The influence of irradiated spot size on laser energy coupling to electrons, and subsequently to protons, in the interaction of intense laser pulses with foil targets is investigated experimentally in this chapter. Proton acceleration is characterized for laser intensities ranging from 2×10^{18} - 6×10^{20} W/cm^2, by (1) variation of the laser energy for a fixed irradiated spot size, and (2) by variation of the spot size for a fixed energy.

6.1 Effect of the laser spot diameter on the fast electrons

In the TNSA mechanism, a large population of hot (relativistic) electrons generated at the focus of the high power laser pulse is injected into the target and

propagates through it, forming a sheath with a ∼TV/m field at the rear surface, resulting in ionization and ion acceleration. The need to optimize and control the properties of the resulting high energy ion beam has motivated numerous studies on the influence of laser pulse parameters on ion acceleration - see for example Ref.[138, 139, 192]. Despite the significant progress made, the functional dependencies of TNSA-ion beam parameters on the laser irradiation conditions are still far from fully understood. Recent investigations employing large laser irradiated spots (defocused irradiation), for example, suggest that the laser irradiated spot size may play an important and previously unexplored role in defining the properties of beams of laser-accelerated protons (beyond simply being a parameter in defining the laser intensity) [193–195].

In this chapter, the sensitivity of the maximum proton energy, E_{max}, to the laser irradiated spot size is investigated for picosecond laser pulses.

6.2 Experimental set-up

The experiment was performed using the Vulcan laser. The laser pulse energy (on target), E_L, was varied in the range 3-150 J and the laser spot radius, r_L, was varied in the range 4-40 μm. The p-polarized laser beam was focused, at an incident angle θ_L, of 23° (with respect to target normal), using an f/3 off-axis parabolic mirror (OAP). A limited number of data shots were taken with $\theta_L = 7°$ and 48° to test the effect of incident angle on E_{max}. The planar targets were 2 mm × 2 mm and consisted of a layer of 100 μm Al (interaction and propagation layer), a 5 μm Cu fluorescent layer and a 1 μm Al rear surface layer. The laser pulse contrast ratio was 10^9 on a ns time scale, minimizing the ASE-generated preplasma at the target front surface.

Kα X-ray emission from the Cu fluorescent layer was imaged using a spherically bent Bragg crystal with a FujiFilm BAS image plate detector. This provided a time-integrated measurement of the spatial extent of the hot electron distribution near the target rear surface[169]. The magnification was set to 10.

The proton beam spatial-intensity distribution and spectrum were measured using stacked dosimetry film (RCF), positioned 5 cm from the rear of the target. The stacks covered an energy range from 1.2-40 MeV.

The laser pulse intensity was varied in two separate scans. In the first, referred to hereafter as the *energy scan*, E_L was varied from 3 to 150 J at a fixed laser spot radius r_L ~4 μm (Half Width at Half Maximum in the plane of the laser beam). In the second scan, referred to as the *focus scan*, r_L was varied from 4 to 40 μm, by defocusing (moving the OAP along the propagation axis), at fixed $E_L = 150$J.

6.3 Experimental results

Figure (6.1) shows the experimental results for both scans. E_{max} and η_{L-p}, increasing with the laser intensity, are higher in the case of the focus scan compared to the energy scan at a given laser intensity (except at the highest intensity, corresponding to the smallest spot size at best focus).

Measurements of the lateral extent of the Kα source, shown in figure (6.1(c)), near the target rear surface show small variations with the laser intensity. The hot electron beam divergence half-angle θ, deduced from the Kα lateral extent for both scans, is shown in figure (6.1(d)). θ shows also small variation with I_L, with an average value of θ is 42°(Standard deviation 4°).

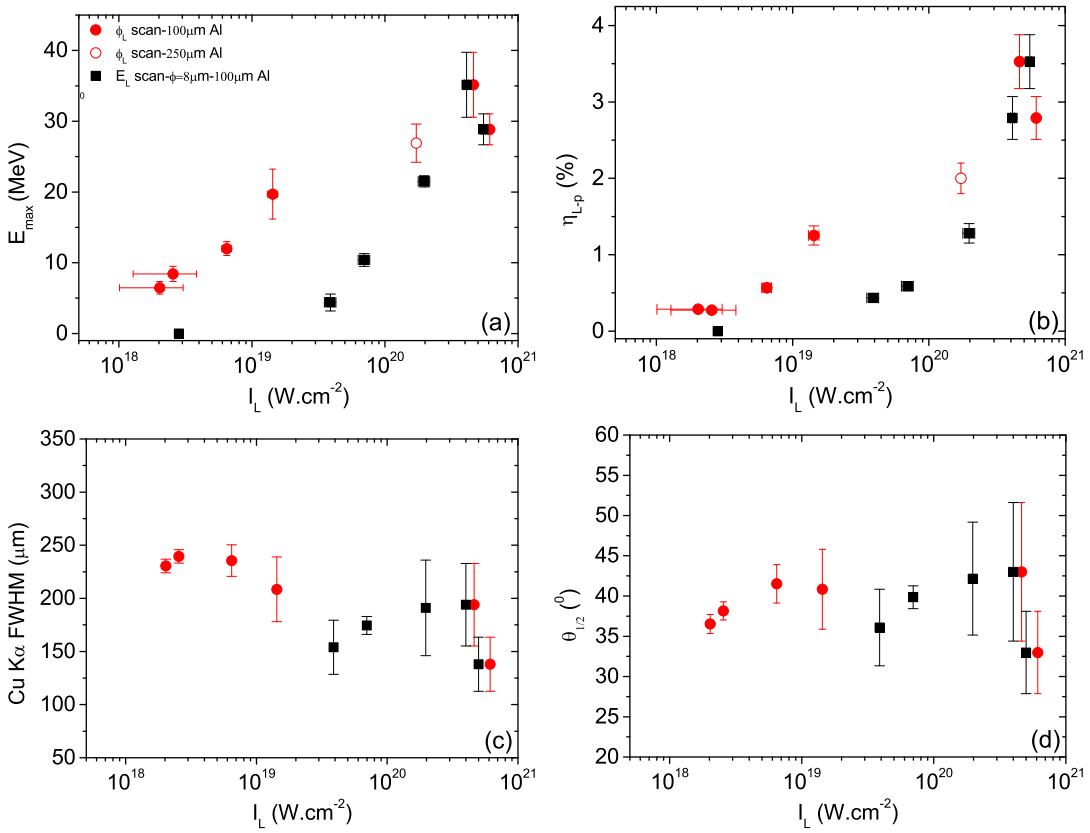

Figure 6.1: (a) Measured maximum proton energy as a function of laser intensity, by variation of laser energy for fixed irradiated spot ('E_L scan') and by variation of irradiated spot size for fixed energy ('ϕ_L scan'), at given angles; (b) The Laser-to-proton energy conversion efficiency as a function of laser intensity for both scans; (c) The Cu Kα lateral extent as a function of laser intensity for both scans; (d) The hot electron beam divergence half-angle, based on the Cu Kα emission, as a function of laser intensity for both scans.

6.4 Discussion & comparison with published data

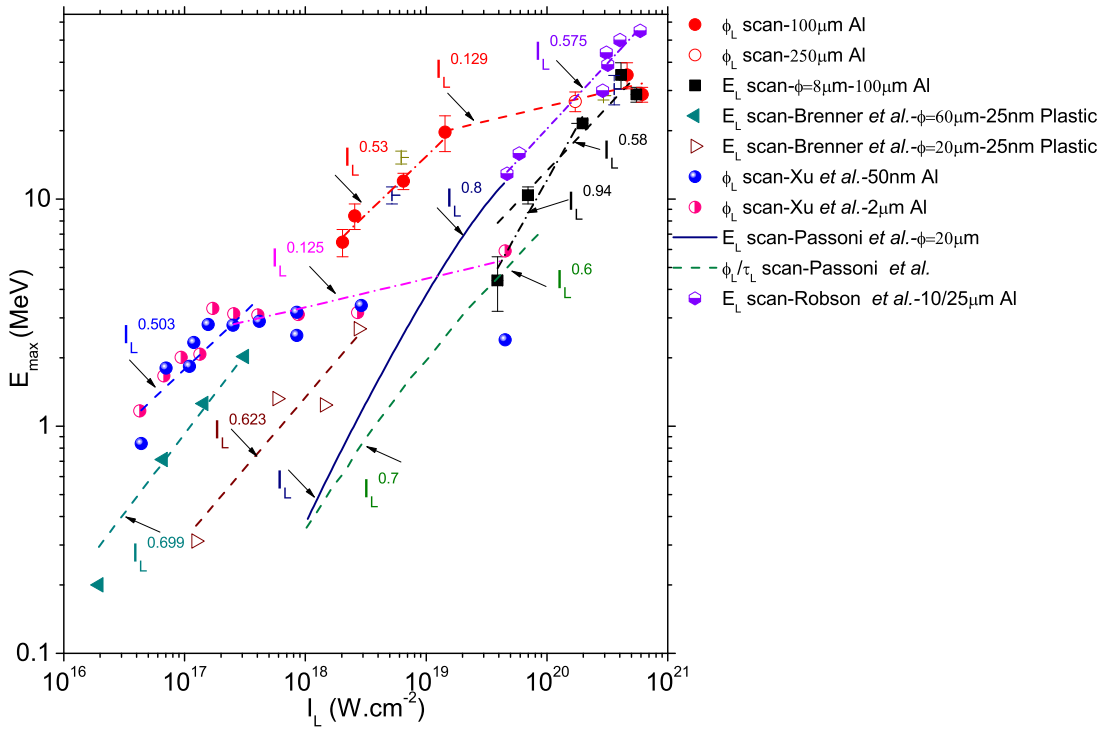

Figure 6.2: Maximum proton energy as a function of laser intensity. The results were obtained over a wide range of laser parameters and target materials. Experimental proton energies are also reported in [10].

Figure (6.2) presents a summary of published experimental data, obtained by an energy scan or focus scan. Most of the targets are $\leq$ tens of μm-thick targets, except for this experimental work made using 100μm-thick targets. Depending on the selected points, E_{max} scales with $I_L^{\sim 0.6}$ in most of the results obtained at large laser spot size. Note that a plateau ('saturation' in the maximum proton energy) can be seen for the focus scan and in the experimental results of Xu *et al.* (also by laser spot size variation), resulting in a scaling of E_{max} with $I_L^{\sim 0.13}$. As already mentioned, the maximum proton energy and the number of protons accelerated

(i.e. the laser-to-proton energy conversion efficiency) is higher at a given intensity for the focus scan, compared to the energy scan. This observation is consistent with the results of Green *et al.*[193] and Xu *et al.*[196], that the number of low energy protons increases with laser irradiated spot size. Xu *et al.* experimentally and from 2D PIC simulations, reported a change in the fast electron spectrum when varying the laser spot size. Under defocused laser irradiations, the number of low and moderate energy electrons is increased. They deduced that the enhancement of the low and moderate energy protons, in a defocused geometry, is due to the large number of electrons that induce a sheath field over a large area on the target rear surface. Green *et al.*[193] confirmed that the highest maximum proton energy is obtained at the highest laser intensity. A significant increase in the 'low' energy proton flux is also achieved under defocused laser irradiations. Green *et al.* deduced, from 1D PIC simulations, that the enhanced spectral flux can be explained by a larger accelerating sheath field, due to an increased laser spot, and the changes in the proton emission, due to the reduction of the laser intensity. A difference in the ion flux was noticed, for a given laser spot size, by displacing the focusing parabola toward or away from the target.

In the present work, the rear fast electron beam diameter inferred from the measured Cu Kα FWHM, varies little when comparing both scans, at a given laser intensity. Based on this diagnostic, no clear change in the fast electron beam diameter with the laser spot size can be seen. Note both [193, 196] used sub 10s of μm-thick foils, which might explain the geometrical changes of the sheath field at large focal spot size, in comparison to the present investigation with work on 100 μm-thick foil and r_L up to $\sim 40\mu$m.

6.5 Analytical model

To explain the measured trends in E_{max}, a simple model of ballistic hot electron transport through the target is adopted and the Mora 1D isothermal plasma expansion formulae [136] used to provide a theoretical E_{max} for given hot electron

beam properties at the target rear surface.

E_{max} is mainly determined by three input variables: kT_f , t_{acc} and n_f. kT_f is given by the ponderomotive scaling [63], and thus by I_L. A finite $t_{acc} = 1.3\tau_L$ [138] is assumed. The differences in E_{max} between the two scans are given by differences in n_f. n_f can be expressed as $n_f = n_{front} \times F(\theta, r_L, L)$, where n_{front} is the hot electron beam density at the source (laser focus) and $F(\theta, r_L, L)$ is a transport factor which is a function of θ, r_L and L, the target thickness. F represents the effects of the fast electron beam injection and the transport mechanism on the on-axis beam density at the target rear surface. The transport is assumed to be ballistic in this study. The hot electron beam density at the source is given by: $n_{front} = \eta_{L-e}E_L/(kT_f\pi r_L^2 c\tau_L)$, where η_{L-e} is the laser to electron energy conversion efficiency and c is the speed of light. Varying the laser incident angle, at a given laser intensity, did not significantly change either E_{max} or the Kα source size, at either tight focus or under defocus irradiation, as shown in figure (6.1). Thus justifying the choice of a fixed η_{L-e}, which is set at 0.2, consistent with the work of Nilson *et al.* [85] for similar laser and target parameters.

The method used is similar to previous proton acceleration scaling studies [138], in which the hot electron beam is considered to arise from a laminar source. This is hereafter referred to as model A. The hot electrons are accelerated over the laser pulse duration and propagate ballistically through the target with a fixed divergence half-angle θ, as shown in figure (6.1(d)) (where $\theta = 42°$). The rear sheath profile is a top hat function where the electrons are spread evenly over the laser pulse duration ($c\tau_L$), with radius (HWHM) $r_S = r_L + L\tan\theta$. In this model, the transport factor is $F(\theta, r_L, L) = [r_L/(r_L + L\tan\theta)]^2$, giving a flat hot electron rear density profile. Using this approach, n_f is calculated as a function of the laser pulse intensity for the two parameter scans, and the results are presented in figure (6.3(c)). An average half-angle, $\theta = 42°$, is used in these calculations, as inferred from the Kα measurements. Figure (6.4) shows that the calculated values for E_{max} are lower than the measured ones for both scans.

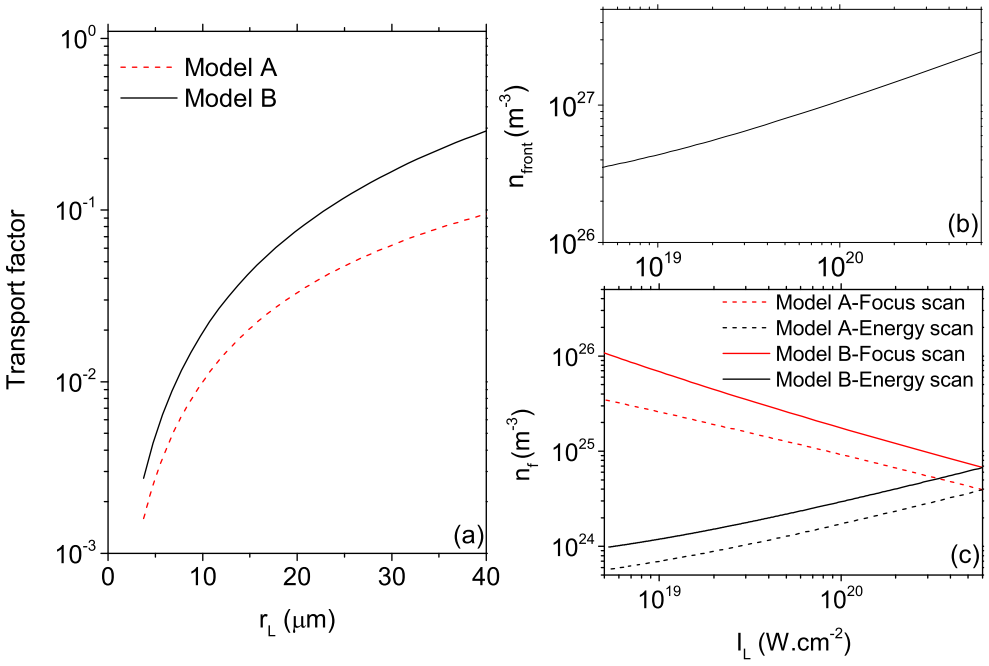

Figure 6.3: (a) Transport factor, F, for the two models, as a function of laser spot radius; (b) Maximum hot electron density at source as a function of laser intensity; (c) Calculated maximum hot electron density on-axis at the target rear surface for the two different models and parameter scans.

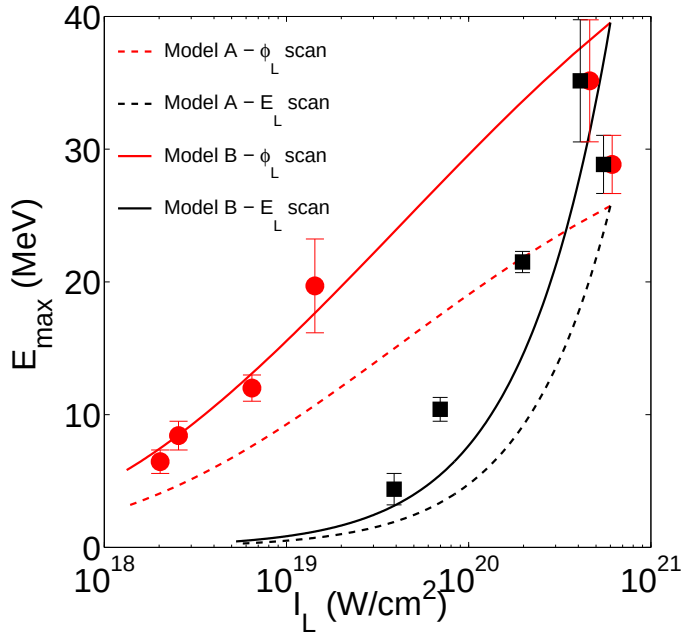

Figure 6.4: Model result maximum proton energy as a function of laser intensity.

Another approach to calculate n_f (referred to hereafter as model B) is to consider the hot electrons as arising from a diffuse source, as illustrated schematically in figure (6.5), which can be described as a summation of elements [197], each of which injects electrons into the target with the same divergence half-angle $\theta = 42°$. The hot electrons are transported ballistically within the target, as with model A. The on-axis transport factor in this approach is $F_0(\theta, r_L, L) = \ln(1 + r_L^2/L^2)/\left(2(1 - cos\theta)\right)$, for $\theta > \arctan(r_L/L)$. F_0 is derived by integrating the electron flux contribution from each element of the source at the target front side, to obtain the flux on-axis at the rear side. It is assumed that the total front side flux is uniformly distributed over the laser focal spot area (of radius r_L) and that the flux within the cone of half angle θ is uniform, but the different geometrical path lengths from each source element to the on-axis point of interest is taken into account. Model B is detailed in the next subsection.

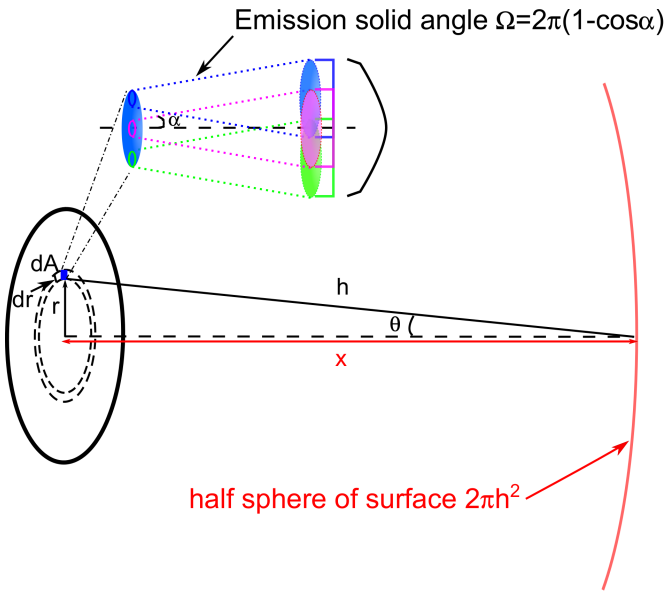

Figure 6.5: Cartoon representing the 1D diffuse source model.

Diffuse model calculation:

The irradiance dI produced by a small element of area dA, from a diffuse source at a point on axis is given by $dI = \frac{I_0 dA}{2\pi h^2}$, where $2\pi h^2$ is the surface of the half sphere at the detection point, and I_0 is the irradiance of the element dA. If the source is circular, the integration of the irradiance from the entire source:

$$I = I_0 \int_0^{2\pi} \int_0^R \frac{r d\theta dr}{2\pi(r^2 + x^2)}$$

leads to

$$I = \frac{I_0}{2} \left(\ln \left[R^2 + x^2 \right] - \ln(x^2) \right)$$

$$I = \frac{I_0}{2} \ln \left[1 + \frac{R^2}{x^2} \right]$$

From analogy, the same arguments apply to a particle flux. A semi-isotropic point source of particles gives

$$d\Gamma = \frac{\Gamma_0 dA}{2\pi h^2},$$

where $d\Gamma$ is the particle flux contribution from the element dA, and Γ_0 is the source flux. The total flux at the detection point is expressed as

$$\Gamma = \frac{\Gamma_0}{2} \ln \left[1 + \frac{R^2}{x^2} \right]$$

The particle flux from the source is given by $\Gamma_0 = n_{front} c$, where n_{front} is the front density of the fast electrons, and c is the speed of light. It results

$$n_f = \frac{n_{front}}{2} \ln \left[1 + \frac{R^2}{x^2} \right]$$

Incorporating the half divergence angle α and assuming $\alpha > \arctan(R/x)$(condition for the two extreme element of the source to overlap at the detection point on axis), the particle flux contribution from an element dA becomes

$$d\Gamma = \frac{\Gamma_0 dA}{2\pi(1 - \cos\alpha) h^2},$$

where $2\pi(1-\cos\alpha)h^2$ is the surface defined by the emission solid angle (The particle flux is no more semi-isotropic). This yields for the rear density expression:

$$n_f = \frac{n_{front}}{2(1-\cos\alpha)} \ln\left[1+\frac{R^2}{x^2}\right]$$

Analytical model results

Application of model B has the effect of changing the hot electron density distribution at the target rear surface to a parabolic-like profile, in agreement with the conclusions of Romagnani *et al.* [145] and Brambrink *et al.* [146]. Thus the on-axis density is enhanced compared to the equivalent uniform injection distribution (model A), leading to higher maximum proton energies. As shown in figure (6.4), the diffuse source model reproduces the trend observed experimentally for both scans. A parabolic-like density profile will produce a proton beam divergence similar to that measured experimentally [144]. Although a uniform density is implicit in the 1D Mora expansion model, the use of this model is appropriate even in the case of model B as the variation in n_f is small in the region of the peak density. For example, n_f is reduced by only 3% at 20μm from the central axis, a distance much larger than the Debye length, resulting in a reduction in E_{max} by 2%. In model B, since θ and L are constant, the transport factor F varies only with r_L. In the energy scan, F is therefore constant and n_{front} increases with I_L, as shown in figure (6.3(b)), so that n_f and therefore the maximum proton energy vary rapidly with I_L, as shown in figure (6.3(c)) and figure (6.4), respectively. By contrast, in the focus scan, F increases with r_L (figure (6.3(a))), and therefore decreasing intensity. Even though n_{front} decreases at the same rate as it does in the energy scan, n_f increases with decreasing intensity, as shown in figure (6.3(c)), due to the increase in F and constant E_L. The reduction in kT with intensity means that the maximum proton energy still decreases, but at a much slower rate than in the energy scan.

6.6 Numerical simulations

It is shown in chapter 5, that the fast electron beam divergence is controlled by self-generated resistive fields and collisions with the background plasma in high Z targets. The self-generated azimuthal magnetic field [24, 25, 108, 111, 178], that pinches the fast electron beam while propagating through the overdense plasma, can be approximated by $\partial B/\partial t = \eta J_f/r_f$. The analytical modeling and Fokker-Planck simulations of Bell *et al.* [24] demonstrated that, even when the initial beam is not strongly anisotropic, the fast electron source can be collimated into a beam. Collimation occurs if $[r_f/r_g > \alpha_{1/2}^2]$ (r_g the Larmor radius), i.e. the magnetic field is strong enough to bend the fast electron through the angle ($\alpha_{1/2}$) in a distance equal to ($r_f/\alpha_{1/2}$) in which the beam radius doubles. Bell *et al.* also show that the collimation is less favorable at high initial divergence angle of the fast electron source, laser power, and fast electron temperature.

In this experimental work the fast electron source size, assumed equal to the laser spot size, is increased by a factor of ten. The B-field strength is then expected to fall with increasing fast electron beam size.

The effect of the laser spot size on the fast electron beam collimation is investigated using ZEPHYROS code. The simulations were performed using a 500 μm $\times$ 500 μm $\times$ 100 μm box with a resolution equal to 2 μm $\times$ 2 μm $\times$ 2 μm. The fast electron source input parameters were chosen to match the experiment parameters. $T_f[eV]$ is given by the ponderomotive scaling [63] at laser intensity matching the experiment. η_{L-e} (determining the number of fast electrons), unless specified, is equal to 0.2. The fast electron energy distribution is of the form of $N_f(E_e) = N_f exp(-E_e/T_f)$, and the angular-energy injection distribution is derived by Moore *et al.* [60]. The model of resistivity as a function of temperature for Al is the one used by Davies [107], based on a fit to the data published in Milchberg *et al.* [48]. The initial background temperature was set at 1 eV. The front and rear boundaries are reflective and side boundaries are open. The electrons were injected into the solid over a pulse duration of 1 ps, in a focal spot

(Gaussian transverse profile & top hat temporal profile) with radius varied between simulations: equal to 4, 15, 30 and 40 μm (for the energy scan, the source radius is kept equal to 4 μm).

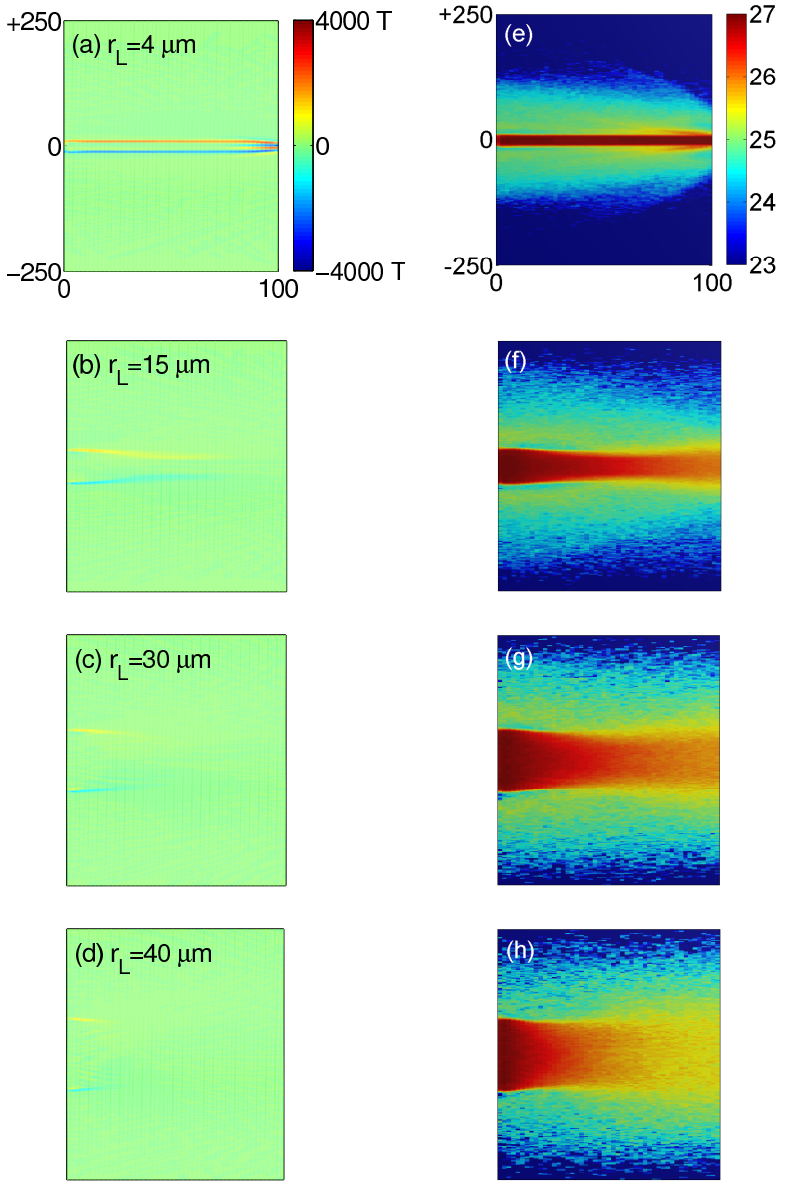

Figure 6.6: (a-d) False-color 2D maps of the z-component of the self-generated resistive B-field (in units of Tesla); (e-h) Corresponding false-color 2D profiles of the fast electron beam density ($\log_{10}$ (m^{-3})) ; extracted at a runtime equal to 1 ps for $< \theta_{1/2} >= 30°$.

As can be observed in figure (6.6), a clear decrease in the magnetic field strength is found by increasing the fast electron source size (and thus reducing the laser intensity). A comparison of the B-field and the density distribution profiles, for $r_L = 4\ \mu m$, $\eta_{L-e} = 0.2$ and $< \theta_{1/2} >= 50°$ and for different peak laser intensity, is shown in figure (6.7). A decrease in the laser intensity (i.e. the decrease in the fast electron number and temperature) as expected leads to a drop of the B-field strength and thereby the beam density.

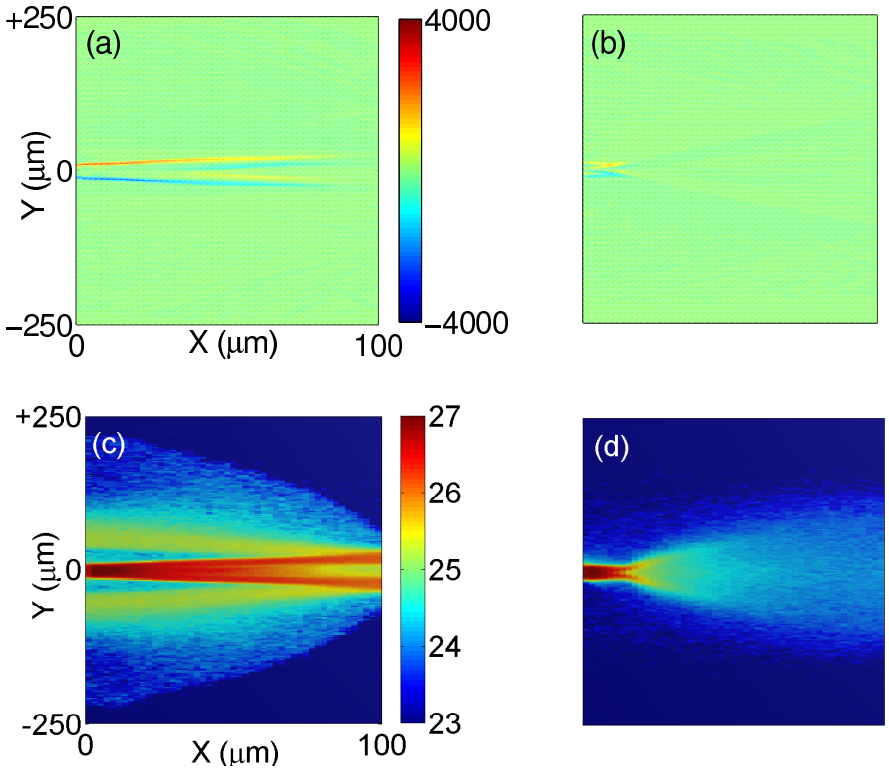

Figure 6.7: (a-b) False-color 2D maps of the z-component of the self-generated resistive B-field (in units of Tesla); (c-d) False-color 2D profiles of the fast electron beam density ($\log_{10}\ (m^{-3})$) ; extracted at a runtime equal to 1 ps for $< \theta_{1/2} >= 50°$, $r_L = 4\ \mu m$ and $\eta_{L-e} = 0.2$. The laser intensity is 6×10^{20} W.cm^{-2} for (a) and (c). The laser intensity is 3×10^{18} W.cm^{-2} for (b) and (d).

Resulting E_{max}

n_f, shown in figure (6.8), and t_{acc} are extracted from the numerical simulations and used as input to Mora's plasma expansion formula [136], as done in the previous chapter. E_{max}, determined from the simulation results, is then compared to experimental results.

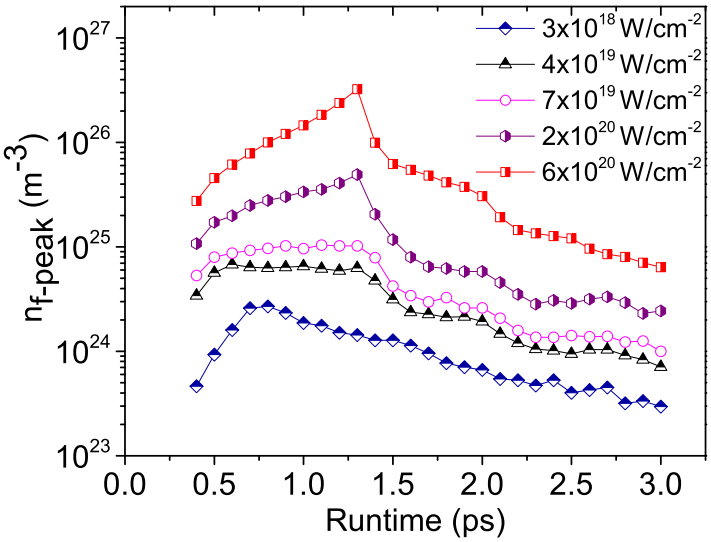

Figure 6.8: Temporal evolution of the rear peak density for different laser intensities, for parameters corresponding to the energy scan.

By choosing the parameters $\eta_{L-e} = 0.2$ and $< \theta_{1/2} >= 50°$ as input parameters into to numerical simulations, as shown in figure (6.9), the E_{max} experimental trend is well reproduced for the energy scan.

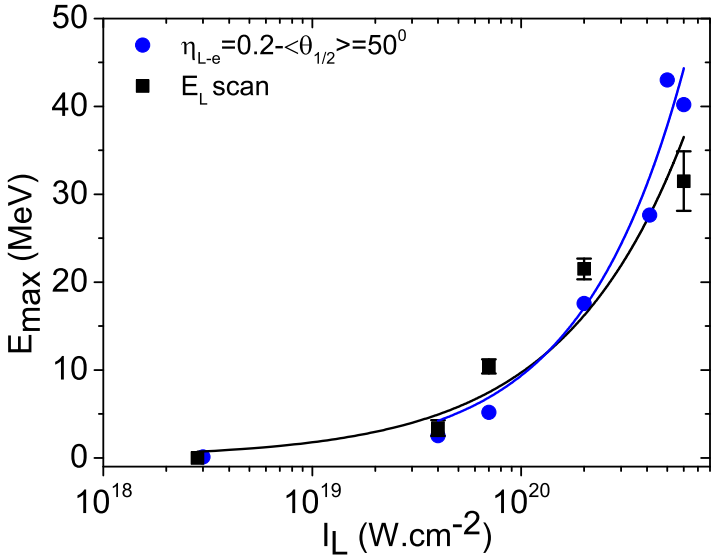

Figure 6.9: Proton maximum energy deduced from plasma expansion model using the numerical simulation outputs, for parameters corresponding to the energy scan. Note that the peak experimental E_{max} shown in this graph corresponds to the mean value of the experimental results obtained at the same intensity.

Figure (6.10) presents results deduced from numerical simulations, coupled with Mora's plasma expansion model, for parameters corresponding to the focus scan. The ion acceleration time, deduced from the numerical runs, is found to be of the order of the laser pulse duration when the laser pulse radius is increased. No single η_{L-e} and $< \theta_{1/2} >$ combination accurately reproduces the E_{max} trend with I_L obtained by laser spot variation. In general, the fast electron beam injection half-angle need to be reduced, when increasing the source spot size, in order to obtain a close trend to the proton maximum energy.

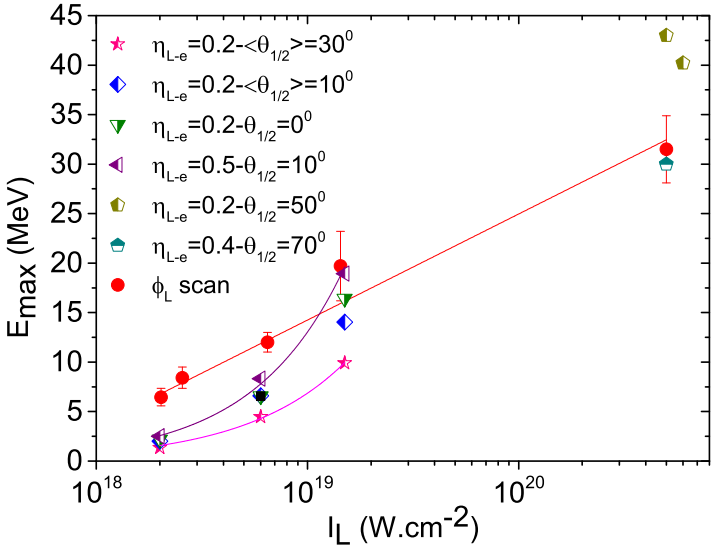

Figure 6.10: Proton maximum energy deduced from from plasma expansion model using the numerical simulation outputs, for parameters corresponding to the focus scan.

6.7 Summary & future work

This work highlights the importance of the laser spot size in changing the fast electron beam properties and consequently the TNSA-generated ion characteristics.

While the highest maximum proton energy is obtained at the highest laser intensity, higher proton energies are obtained, under defocused laser spot, compared to tight focus for a given laser pulse intensity. A slower decrease in the measured maximum proton energy as a function of decreasing intensity is observed in the focus scan, compared to the energy scan at best focus. The laser-to-proton energy conversion efficiency is increased in the focus scan at a given I_L, compared to the energy scan. This cannot be accounted for only by differences in the laser pulse energy alone, which set the laser-generated fast electron number. An enhancement of the low energy protons is also obtained under defocused laser

irradiations, as observed in [193, 196]. Xu *et al.* [196] deduced that the increase in the low energy protons, enhancing the proton yield, results from an increase in the laser-generated 'moderated' energy electrons under optimized defocused laser irradiations. Green *et al.*, using 50 nm to 6 μm-thick Al foils for laser intensity up to 2×10^{19} W.cm^{-2}, concluded that the change in the proton spectra results from geometrical changes due to a large focal spot size, and from the reduction of the laser intensity. A scaling of E_{max} with $I_L^{\sim 0.6}$ is found, for most of the experimental results obtained at large laser spot size. A plateau is observed for the focus scan and in the experimental results of Xu *et al.* (also by laser spot size variation), resulting in a scaling of E_{max} with $I_L^{\sim 0.13}$.

An analytical model based on a diffuse source geometry is introduced in this chapter, which, for the parameters of the experiment reported provides a better approximation of hot electron beam injection and propagation.

A next step would be numerical investigations, via PIC simulations, of the laser energy absorption, the resulting fast electron distribution function and injection angle under defocused laser irradiations. The outputs of the PIC simulations, can then be used as input parameters to hybrid code simulations in order to investigate the fast electron beam transport in hundreds of microns solids, to deduce the properties of accelerated ions.

Chapter 7

Laser-to-fast electron energy conversion efficiency: Effect of preplasma conditions

In this chapter, the laser-to-fast electron energy conversion efficiency, η_{L-e}, is investigated over a wide range of experimental conditions. 2D images of the Cu K_α emission and the TNSA-generated proton beam are used as diagnostics for the fast electrons. As in the previous chapters, 1D plasma expansion model and 3D numerical simulations using a hybrid code are employed to model the fast electron beam transport in the solid.

In the first section, simultaneous measurements of the Cu K_α emission and the proton acceleration, obtained by changing the laser pulse intensity and contrast ratio, are reported. The main data sets were obtained using the Phelix laser at GSI and the Vulcan laser at the RAL. Published experimental results and numerical simulations are included in this work. The second section presents a simple 1D model, including results from both diagnostics of the fast electron beam, enabling the laser-to-fast electron energy conversion efficiency to be inferred. In the final section, numerical simulation results of the fast electron beam transport using a hybrid code coupled with a 1D plasma expansion model predict the maximum

proton energy variation with the laser intensity, at a specific η_{L-e}, for comparison to the experiments.

7.1 Experimental set-up

The experimental data presented in this chapter were obtained during two different experimental campaigns. The main differences in the laser system were the laser pulse contrast ratio and energy, the angle of incidence on target θ_L and polarization. The laser pulse contrast ratio varied from 10^4 to 10^6 on a nanosecond timescale for the *s*-polarized Phelix laser. The laser pulses were focused on the target at an angle of $\theta_L = 45^\circ$ to the target normal. The *p*-polarized Vulcan laser pulses were focused onto the target at an angle of $\theta_L = 23^\circ$ with an ultra high contrast ratio of 10^9 on a nanosecond timescale. Both laser system main parameters are summarized in table (7.1).

Table 7.1: Phelix laser & Vulcan laser main parameters.

	Vulcan laser	Phelix laser
$\lambda_L(\mu m)$	1.054	1.054
$\tau_L(ps)$	0.8± 0.2	0.5±0.1
Spot size (at best focus μm)	$\phi_L \sim 8$	$30 \times 13(\phi_L = 13)$
Peak E_L (on target J)	$\sim$ 125± 25	$\sim$ 80
Peak I_L(W/cm^2)	6×10^{20}	2×10^{19}
$\theta_L(^\circ)$	23	45
Contrast ratio	$\sim 10^{9-10}$ - ns scale[a]	10^{4-6} - ns scale[b]
ASE intensity (W/cm^2)	$\sim 10^{10-11}$	$\sim 10^{12-15}$
Polarization	*p*-polarized	*s*-polarized

[a] CLF annual report 2009/2010.
[b] V. Bagnoud, EMMI workshop, May 14-15, 2009 Moscow, Russia.

Concerning the target, circular($\phi = 4$ mm) 20 μm-thick Cu(55%)/Ni(45%) alloy targets were used during the Phelix experimental campaign, and planar (5 mm

x 5 mm) layered Al- Cu- Al targets were used during the Vulcan experimental campaign. The Al propagation layer was varied in thickness from 20 to 250 μm, the fluorescent Cu layer was 5 μm-thick and a 1 μm-thick Al layer was included to avoid fluorescence of the Cu due to the lateral spreading of the electrons on the target rear surface [185].
The experimental scan referred to as 'Phelix-10^6' was obtained with a pulse contrast ratio of 10^6 and the scaling in intensity was achieved by varying the laser energy from $\sim$ 6 to 74 J at best focus. The scan referred to as 'Phelix-10^4' was obtained with a pulse contrast ratio of 10^4 , the scaling in intensity was achieved by varying the laser energy from $\sim$ 5 to 55 J at best focus. The scaling in intensity, for the experimental scan referred to as 'Vulcan-10^9, was achieved by varying the laser energy from $\sim$ 17 to 150 J at best focus. A limited number of laser shots were taken under different laser spot sizes or incident angles on target. The conditions under which each shot was obtained are specified in the text.

The diagnostics, used during the Vulcan laser experimental campaign, to record the data presented in this chapter, were a spherically bent Bragg crystal coupled with FujiFilm BAS image plate detector [155, 169] for the X-ray emission and dosimetry film (RCF HD-810) stacks [149] to measure the proton beam. The spherically bent Bragg crystal, viewing from the target rear surface side, was used to make time-integrated 2D measurements of the K_α fluorescence of the Cu layer. The magnification of the imaging system was 10. To measure the spatial-intensity distribution of the beam of protons accelerated from the target rear surface *via* the TNSA mechanism, dosimetry film stacks were used. The RCF stack was positioned 5 cm from the rear of the target. The film layers act as filters and the proton beam spectrum can be deconvolved in energy steps which depend on the number and thickness of the films used. The stacks used in this experiment enable the proton energy spectrum to be measured in the range 1.2 to 40 MeV.

In the Phelix laser experimental campaign, an RCF stack viewing the target rear surface was used as diagnostic of the TNSA-generated proton beam. The RCF stack, positioned at 6.5 cm from the target rear surface, surrounded the

target, forming an arc of 230° in the horizontal plane. The stacks enable the proton energy spectrum to be measured in the range 2.2 to $\sim$ 22 MeV. The experimental set-up is described in Gray *et al.* [198].

Measurement of the K-shell emission, from a buried fluorescent layer, has been widely used to infer the fast electron beam diameter and divergence angle, by measuring the recorded 2D image lateral extent of the X-ray source at a given depth in the solid [1, 2, 14, 15, 42, 85, 155]. The TNSA-generated proton beam [8] scaling with the fast electron beam density [136] enables the fast electron beam source size and indirectly η_{L-e} to be inferred [1, 2, 186, 189].

7.2 Experimental results & discussion

The experimental results obtained on both campaigns and $K\alpha$ lateral extent results from previous published work, are shown in figure (7.1, 7.2, 7.3 & 7.4). The $K\alpha$ lateral extent obtained on the Vulcan laser, shown in figure (7.1), shows small variations with the laser intensity. Figure (7.2) presents published $K\alpha$ lateral extent obtained over a wide range of experimental conditions. No clear tendency can be directly seen from these data sets, the lateral extent seems to increase slightly with increasing target thickness, laser focal spot size and intensity. The results obtained on 20 μm-thick targets, that can be related to one of the main data set obtained on 20 μm-thick alloy targets, are summarized in table (7.2).

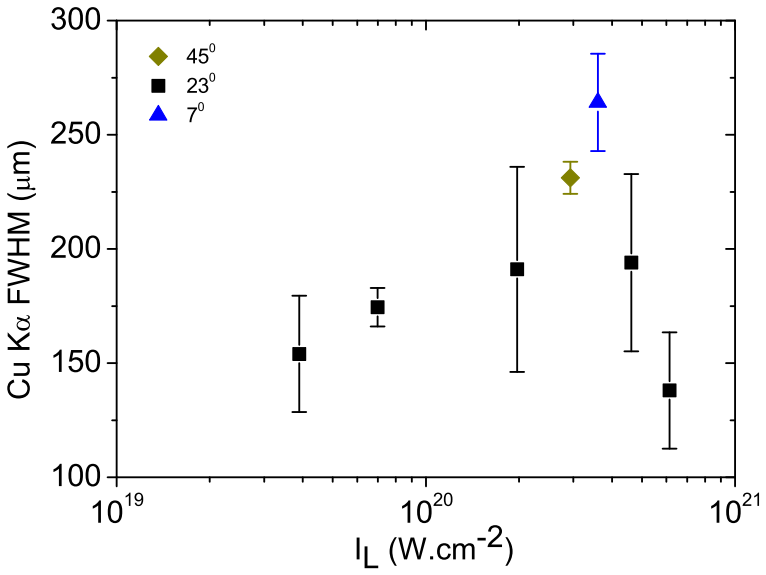

Figure 7.1: The Cu $K\alpha$ lateral extent (FWHM) as a function of the laser intensity obtained on the Vulcan laser. The targets were 100Al-5Cu-1Al. The laser pulse contrast ratio was 10^9 therefore little preplasma was generated at the target front surface before interaction with the peak intensity of the laser pulse.

Table 7.2: Published $K\alpha$ emission FWHM obtained on 20 μm-thick targets; [78] (1) correspond to a small preplasma density scale length (e^-/cm^3): $1.530 \times 10^{25}(10-x)^{-3.0}$, (2) intermediate scale length (e^-/cm^3): $7.095 \times 10^{24}(14-x)^{-2.7}$ and (3) long scale length (e^-/cm^3): $5.805 \times 10^{24}(20-x)^{-2.4}$.

Reference	ϕ_L (μm)	$\tau_L(ps)$	Peak I_L (W/cm^2)	Target composition	$K\alpha$ FWHM (μm)
[15]	7	5	4×10^{19}	Ti ,Cu, Al-Cu-Al	61
[15]	50	5	1.5×10^{19}	Ti ,Cu,Al-Cu-Al	103
[14]	7	0.5	5×10^{20}	Cu	85
[78] (1)	12	0.8	2×10^{19}	CH-Al-Cu-Al	134
[78] (2)	12	0.8	2×10^{19}	CH-Al-Cu-Al	122
[78] (3)	12	0.8	2×10^{19}	CH-Al-Cu-Al	111

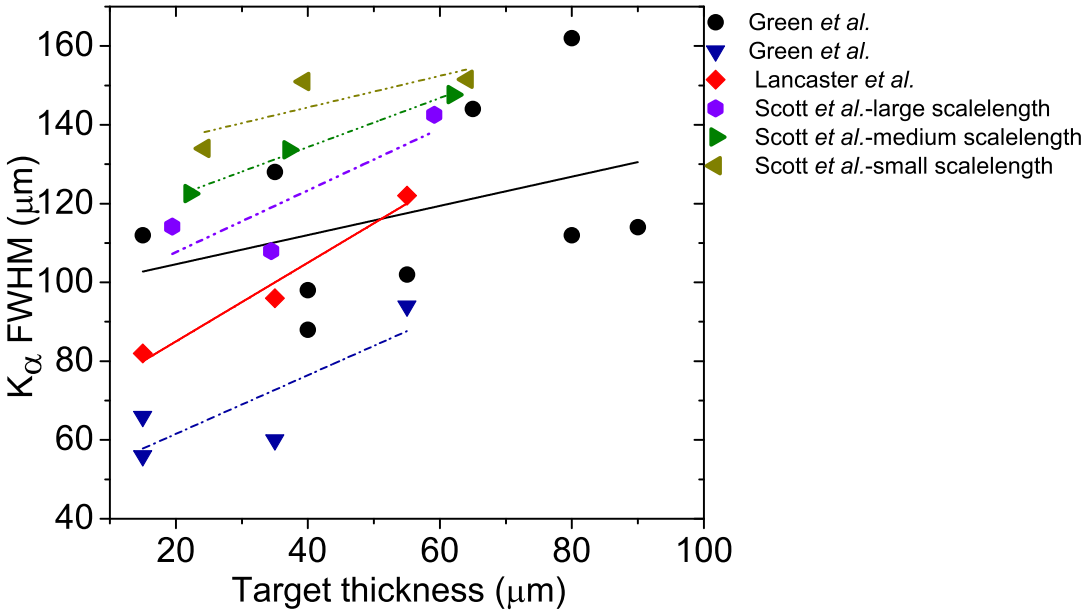

Figure 7.2: $K\alpha$ lateral extent (FWHM), from the previous published work, as function of the laser intensity. The experimental results of Green *et al.* [15], represented by triangles, were obtained on the Vulcan laser, at a pulse duration of 5 ps, a laser spot diameter of 7 μm and an intensity of 4×10^{19} $W.cm^{-2}$. The experimental results of Green, represented by circles, were obtained at a laser spot diameter of 50 μm and an intensity of 1.5×10^{19} $W.cm^{-2}$. The targets used were 25-100 μm-thick Ti and Cu or layered targets (Al-25Cu-Al). The experimental results of Lancaster *et al.* [14] were obtained on the Vulcan laser, at a pulse duration of ~0.5 ps, a laser spot diameter of 7 μm and intensity of 5×10^{20} $W.cm^{-2}$. The targets used were 5-75 μm-thick Cu. The experimental results (mean values) of Scott *et al.* [78] were obtained on the Pico 2000 laser, at a pulse duration of ~0.8 ps, a laser spot diameter of 12 μm and intensity of 2×10^{19} $W.cm^{-2}$. The targets were layered CH-Al-Cu-Al targets.Three distinct preplasma scale lengths were generated at the target front surface.

By contrast, the proton maximum energy E_{max}, shown in figure (7.3 & 7.4), presents a strong dependency on I_L and the preplasmas conditions.

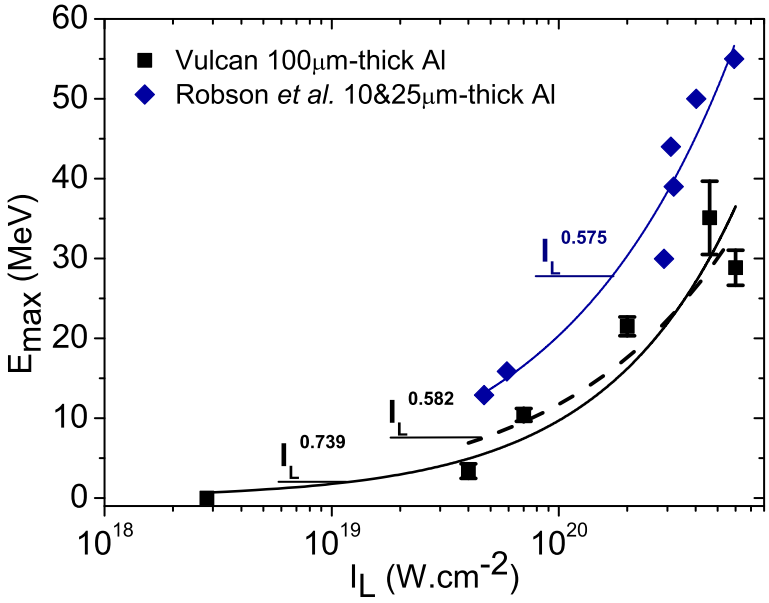

Figure 7.3: Proton maximum energy as a function of the laser intensity obtained using the Vulcan laser.

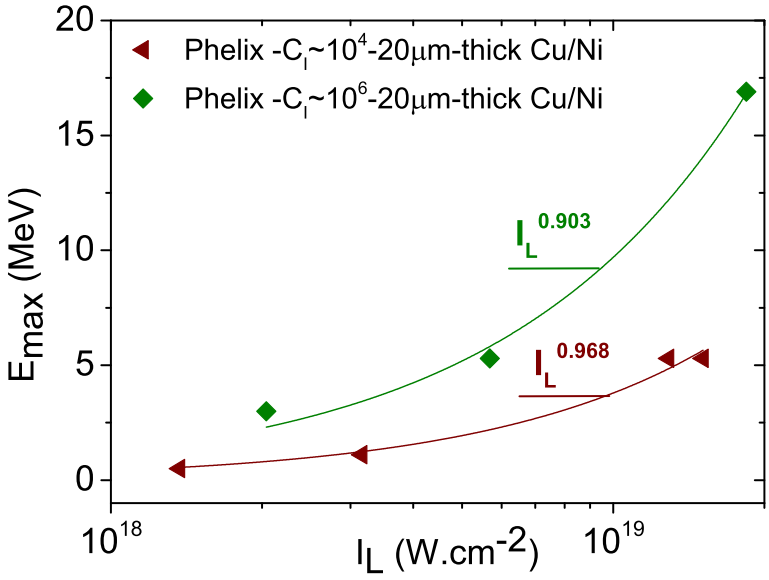

Figure 7.4: Proton maximum energy as a function of the laser intensity obtained using the Phelix laser.

A power fit to the laser intensity scans made by laser energy variation shows two distinct scalings for the proton maximum energy with the laser intensity. In both scans made on the Phelix laser, where the intensity on target and the pulse contrast ratio are lower than on the Vulcan laser, E_{max} scales with $I_L^{\sim 0.9}$ similar to the scaling presented in Passoni *et al.* [195]. For the scan performed on the Vulcan laser, E_{max} scales with $I_L^{\sim 0.6-0.7}$ consistent with the experimental scaling with $I_L^{\sim 0.6}$ previously published in Robson *et al.* [192] using the same laser but using 10 & 25 μm-thick Al targets and laser pulse durations from 1 to 8 ps. The effect of the preplasma scale length on the fast electrons, generated during the interaction of the main laser pulse with the preplasma/solid front surface, is discussed in the next subsection.

7.2.1 Effect of the preplasma on the fast electrons and consequently on the TNSA-generated proton beam

Previous theoretical and experimental studies [18, 20, 78–83, 199], using the laser main pulse ASE or a controlled second laser pulse to change the properties of the preformed plasma at the target front surface, show the importance of the preplasma on the characteristics of the accelerated electron beam and consequently on the TNSA-generated proton beam. As an example, for a laser system such as the Phelix laser, which until a recent upgrade, provided a laser intensity of 1×10^{19} W/cm^2 with an intensity contrast ratio of 10^4 on a nanosecond time scale, the prepulse intensity is of the order of $\sim 10^{15}$ W/cm^2 which produces a significant preplasma expansion on the target front surface. The energy contained in the ASE/prepulse and its duration with respect to the peak of the laser pulse set the density scale length of the preformed plasma. Depending on the preplasma scale length, the interaction of the main laser pulse with a preplasma causes the laser pulse to self focus [200], to break into filaments [201] and to lose parts of its energy through stimulated Raman scattering [44]. Those processes alter the generation and transport of the fast electron beam and therefore the ion beam

characteristics.

The work of Cai *et al.* [18], using 1D radiation hydrodynamic and 2D PIC simulations, investigates fast electron generation in high intensity laser-matter interactions. The 2D PIC simulations of a linearly polarized laser pulse ($I_L = 1.37 \times 10^{20}$ W/cm^2 and $\tau_L = 2$ ps), interacting at normal incidence with gold targets, were performed for a 1 nanosecond ASE at $I_{ASE} = 10^{11} - 10^{12}$ W/cm^2. It was shown that the absorbed laser energy increases with increasing preplasma density scale length. A change in the fast electron energy distribution, as shown in figure (7.5), was also observed with increasing preplasma scale length.

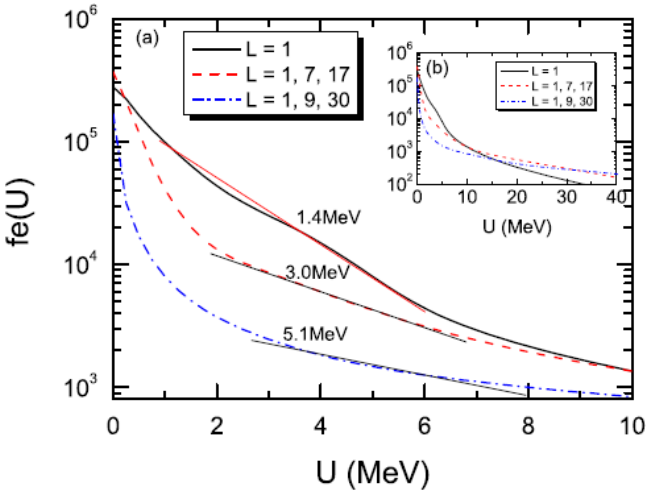

Figure 7.5: The time integrated spectrum of electrons with different preplasma density scale length, reproduced from [18]. Solid black line represents a 'small', dashed red line represents a 'medium' and dashed blue line represents a 'long' density scale length.

For small density scale length, a single temperature energy distribution seems to fit the integrated spectrum for electrons of energies < 10 MeV. At larger preplasma scale length, the spectra tend to a two temperature distribution functions. The fast electron beam temperature for a small preplasma density scale length was found to be consistent with the scaling derived in Haines *et al.* [77]:

$T_f(keV) = 511 \times [\sqrt{(1+\sqrt{2}a_0} - 1]$, where a_0 is the laser amplitude. Thus the main acceleration mechanism is the ponderomotive acceleration $J \times B$. For a middle plasma density scale length, the PIC simulations showed that several acceleration mechanisms such as vacuum heating [71], resonant absorption [202] and $J \times B$, contribute to the acceleration of the electrons. Thus, the fast electron beam temperature inferred from the energy distribution was higher than for the small preplasma scale length. For long plasma density scale length the laser beam can lose most of its energy in the underdense preplasma thus the fast electrons can be accelerated through acceleration mechanisms specific to laser underdense plasma interactions [203, 204], increasing the fast electron beam temperature when compared to a small or middle density scale length. However, laser plasma instabilities start to appear, as demonstrated in [83], altering the fast electron beam properties. Finally, Cai *et al.* argued that the drop in the Ag K_α emission observed in [205], when a large preplasma is present, can be due to the decrease in the fast electron number as the K_α emission is proportional to the electron number rather than a change in the laser-to-electron energy conversion efficiency.

The work of Mishra *et al.* [206], using 1D PIC simulation, investigates the fast electron generation in high intensity laser-matter interactions. Part of the 1D PIC simulations were performed for a linearly polarized laser pulse interacting at normal incidence with a steep density gradient. It was shown that the electrostatic potential, created by the laser pulse pressure at the target front surface, traps the blow-off electrons, forming a sheath $\sim 3\times$ thicker than the skin depth c/ω_p, with ω_p the plasma frequency. The fast electrons accelerated in the skin depth by the evanescent wave are classified in two 'categories': the 'non oscillating' electrons accelerated by to the non 'oscillating' part (due to the laser pulse intensity gradient) of the longitudinal ponderomotive force pushing the electrons in the solid and the electrons oscillating at twice the laser frequency ω_L. The 'non oscillating' electrons have lower energies than the 'oscillating' electrons. By changing the laser polarization from linear to circular, the laser total energy absorption is found unchanged, at a specific target density ($> 100n_c$). Therefore, the genera-

tion of ' non oscillating electrons' is dominant for high density targets ($> 100n_c$), as no 'oscillating' electrons are generated with circularly polarized laser pulses. It was observed that the absorption increases with increasing laser pulse amplitude or when the laser pulse is focused obliquely onto the target (as other absorption mechanisms may contribute). The absorption also decreases with increasing target density. Finally, the set of simulations made including an initial preplasma with a scale length of 2 μm, show that the laser energy absorption is more efficient during the early time of the laser preplasma interaction near the critical density and then drops when the laser interacts with the solid density. It was also found that the fast electron beam temperature, extracted from the energy spectrum, scales with the ponderomotive scaling.

The recent work of Scott *et al.* [78] presents an experimental and numerical study of the fast electrons energy transport in laser-solid interactions [CH(5 μm)-Al(10,20,50 μm)-Cu(10 μm)-Al(1 μm)] with a controlled preplasma generated by the laser's ASE. The laser pulse energy and intensity were equal to 40 J and 2×10^{19} W/cm^2. The ASE energy contrast ratio was in the range of $3 \times 10^{-3} - 1 \times 10^{-2}$, giving a total energy in the ASE varying from $120 - 400$ mJ, in a duration ranging from $1.1 - 4.3$ ns. The different density scale lengths are defined in table (7.2). From PIC simulations, it is inferred that for a large preplasma density scale length the accelerated fast electrons are divided in two populations. Fast electrons accelerated via the $J \times B$ mechanism within the preplasma generated by the prepulse, show a lower beam divergence and a higher temperature compared to these accelerated at the critical density n_c. It was also found that increasing the density scale length, by changing the energy and the duration of the laser ASE, increases the number, energy and temperature of the fast electron accelerated within the coronal plasma. Vlasov-Fokker-Planck modeling of the experimental data shows that the fast electron beam, accelerated in the preplasma, induces a magnetic field within the solid that pinches the fast electron beam accelerated at the critical density surface. PIC simulation results show that, for all three density scalelengths, the total laser-to-fast electron energy conversion efficiency is invariant. The HWHM of the Cu K_α emission is slightly reduced with increasing

density scale length and the divergence half angle is $25 \pm 7°$ (linear fit to the mean values) for all three density scalelengths. Small increase of the emission HWHM is observed with increasing target thickness. However the HWHM of the pyrometric experimental data shows a net reduction of the thermal emission size with increasing plasma density scale length. Finally, the fast electrons source size, observed in the PIC modeling (and extrapolation of the Cu K_α emission & pyrometry data), is much greater then the vacuum laser spot size due to the refraction, at a large incident angle of 45°, of the *p*-polarized laser spot in the preplasma. By reducing the laser incident angle, the fast electron source size can be reduced as the laser refraction can be prevented (at normal incidence).

The work of McKenna *et al.* [83], performed using the Vulcan laser at an intensity of 3×10^{20} W/cm^2, shows an enhanced proton maximum energy by increasing the preplasma density scale length, using a secondary low energy long duration laser pulse ($0.5 - 5 \times 10^{12}$ W/cm^2 in a pulse duration of 6 ns, giving an ASE energy $5 - 50$ J). It was demonstrated that for a density scale length of 30 to 60 μm, the laser pulse self focus in the preplasma, increasing its intensity at the critical density surface hence enhancing the proton maximum energy when compared to a sharp density gradient. By increasing the preplasma density scale length (>100 μm), it was found that the laser pulse breaks into filaments during the propagation in the underdense preplasma region. Thus the laser intensity at the critical density surface is reduced, reducing the maximum proton energy.

PIC simulations of Ovchinnikov *et al.* [20], for $I_L \sim 10^{18}$-10^{21} W/cm^2, show that the fast-electron divergence angle increases almost linearly with the preplasma scale length for a fixed laser intensity. The laser intensity affects little the beam divergence for a fixed preplasma scale length.

In summary, Scott *et al.* [78] observed that the total energy absorbed into fast electrons was unchanged by the density scale length. Based on time-resolved K_α spectroscopy experimental measurements, shown in figure (7.6), Nilson *et al.* [42, 43, 85] infer a conversion efficiency, η_{L-e}=0.2, over the intensity range $I_L =$

$10^{18} - 10^{21}$ W/cm^2. The experimental results were obtained, using copper targets, on the Vulcan laser and the Multi-Terawatt laser system at the Laboratory for Laser Energetics.

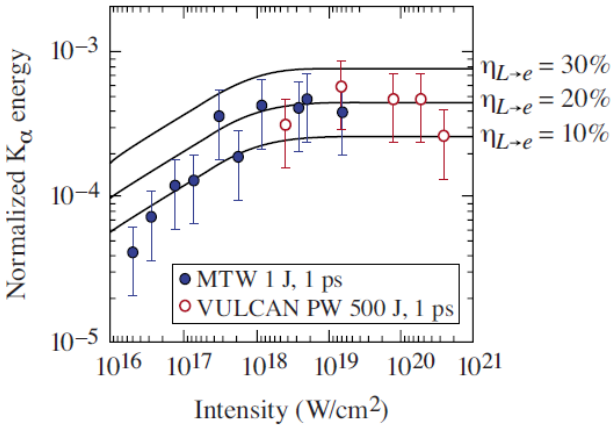

Figure 7.6: Kα energy, normalized to the laser energy, as a function of laser intensity. The figure is reproduced from [42].

However, the work of Ma *et al.* [80] using cone targets, show that η_{L-e} is dependent on the preplasma condition. Furthermore, a significant change in the laser plasma absorption and the fast electron energy distribution with the preplasma scale length is observed in the work of Cai *et al.* [18]. Finally, the simulation results of Mishra *et al.* demonstrate that the laser energy absorption increases with the laser amplitude and is mainly absorbed within the preplasma near the critical density and then drops at the solid target front surface. Thus the preplasma scale length (especially for a middle/long scale length) should affect the laser energy absorption, the hot electrons spectra, and the TNSA generated proton beam.
Concerning the fast electron beam temperature, the $J \times B$ acceleration mechanism is the main mechanism observed for all preplasma scale lengths in the PIC modeling of Scott *et al.* and Mishra *et al.*. However, in the work of Cai *et al.* the $J \times B$ acceleration mechanism is the main mechanism for a small preplasma scale length and several acceleration mechanisms are responsible for the fast electron acceleration in presence of medium/long preplasma scale length.
The difference in the proton maximum energy, as observed in McKenna *et al.*,

can be explained by the effect of a long density scale length preplasma on the laser pulse propagation (self focusing, filamentation) and consequently on the fast electron beam (source size, temperature).

Evaluation of the preplasma density scale length from the laser intensity contrast ratio

The preplasma density scale length, for both experimental campaign described in this chapter, is deduced from the intensity contrast ratio C_I as due to a number of experimental factors a direct measurement was not performed during the experimental campaigns. The ASE intensity on a nanosecond scale (τ_{ASE}), shown in table (7.1), is calculated as follows: $I_{ASE} = I_L/C_I$ W/cm^2. Then, the ASE characteristics allow the preplasma density scale length, and consequently its effect on the laser pulse propagation, and fast electron and the ion generation to be inferred:

$\rightarrow$ **'Vulcan-**10^9**'**: The intensity and energy contained in the ASE on a nanosecond scale is too low to create a significant preplasma and a small preplasma density scale length is generated at the target front surface. A preplasma density scale length of the order of a few microns is found in the region of the critical density, for $I_{ASE} \sim 5 \times 10^{11}$ W/cm^2 (on a nanosecond timescale) interacting at normal incidence with Al targets, by fitting the density gradient by the function of the form of $n_e \propto \exp -x/L_n$, where L_n is the density scale length. The preplasma density profile at the front surface was calculated by the 2D hydrodynamic code POLLUX [207]. The CPA beam rapidly ionizes the solid without significant ablation and interacts with an almost steep electron density. For a linearly polarized laser beam, the longitudinal ponderomotive force can be divided into two parts: a non oscillating part due to the laser envelope that pushes the plasma density profile inward and a $2\omega_L$ oscillating part that heats and accelerates the fast electrons at the critical density, where ω_L is the laser frequency [73]. When the laser interacts with an overdense plasma with steep density gradient, as observed in the 1D

PIC simulation results of Mishra *et al.*, the oscillating part of the ponderomotive force is minimized. The non-oscillating part of the longitudinal ponderomotive force leads to an acceleration mechanism similar to the vacuum heating. The fast electron beam temperature is expected to be lower when compared, at the same laser intensity, to the case where the oscillating term is enhanced, modifying the fast electron beam energy spectra when compared to an intermediate preplasma scale length. In this study, E_{max} scales with $\sim I_L^{0.6-0.7}$. As E_{max} scales with the fast electron temperature T_f, the scaling of T_f with $\sim I_L^{0.6-0.7}$ is close to the ponderomotive scaling [63] with $\sim (I_L \lambda_L^2)^{0.5}$.

→ **'Phelix-10^6'**: The CPA beam interacts with an intermediate preplasma density scale length. A preplasma density scale length of the order of a tens microns is found in the region of the critical density, for $I_{ASE} \sim 2 \times 10^{13}$ W/cm^2 (on a nanosecond timescale) interacting at normal incidence with Cu targets. The fast electrons in this case are accelerated through multiple acceleration mechanisms, resulting in a scaling of $E_{max} \sim I_L^{0.9}$.

→ **'Phelix-10^4'**: The ASE intensity, reaching $\sim 10^{15}$ W/cm^2 (therefore the preplasma expansion could not be modeled by the hydrodynamic code), is high enough to generates a significant preplasma density scale length affecting η_{L-e} and altering the main laser beam propagation. Therefore, based on the conclusion of McKenna *et al.* and Cai *et al.*, the decrease in the proton maximum energy, compared to the proton maximum energy obtained during 'Phelix-10^6', can be explained by the development of laser plasma instabilities, such as filamentation in the dense preplasma. The same scaling than for 'Phelix-10^6' data set, of $E_{max} \sim I_L^{0.9}$ with I_L is found for this data set.

The experimental data were obtained on different laser facilities and experimental conditions. The diagnostics used in the work probe the fast electron beam size and density at the target rear surface after being altered by the interaction and self-generated fields in the propagation layer. Thus, simulations of the fast beam transport in a solid are performed, for a given fast electron source (i.e. at a given η_{L-e}), using a Hybrid-PIC code. Then, the proton maximum energy is inferred from the Mora's 1D plasma expansion model [136] using the fast electron

beam peak density and acceleration time extracted from the Hybrid-PIC results as input parameters. The comparison between the proton maximum energy trend obtained from the simulations and the experimental results enables η_{L-e} to be inferred. Furthermore, the two main scans were obtained using 20 μm-thick Al or Cu/Ni alloy targets and 100 μm-thick Al targets. The work of [122, 182, 183], also discussed in chapter (5), highlighted the importance of electron recirculation on the TNSA-generated protons. The use of 100 μm-thick targets with a laser pulse energy of 0.8 ps minimizes the recirculation within the solid. On the contrary, fast electron recirculation can be important inside 20 μm-thick targets. Therefore, the two scans are presented separately and the effect of the fast electron beam transport and thus recirculation in sub 100 μm targets is investigated using a Hybrid-PIC simulations by changing the boundary condition at the rear simulation box (open or reflective boundary).

In the next section the effect of the laser ASE on η_{L-e} is inferred from the experimental measurements obtained with both fast electrons diagnostics using a simple 1D analytical model.

7.3 Determination of the laser-to-fast electron energy conversion efficiency

As a first step, a simple analytical model is developed to link the experimental results obtained with both Cu Kα and proton diagnostics in order to deduce η_{L-e}. The Mora's [136] 1D analytical model predicts the proton maximum energy as function of the laser intensity. The fast electron beam temperature in this model is given by the ponderomotive scaling [63]. The effective ion acceleration time t_{acc} is of the order of the laser pulse duration [138]. Finally, the fast electron beam density n_f is equal to $N_f/(\pi r_{rear}^2 c\tau_L))$, where r_{rear} is the target rear-surface electron beam radius and N_f the number of fast electrons equal to $\eta_{L-e}E_L[J]/(e \cdot T_f[eV])$. r_{rear} is set equal to the $K\alpha$ emission HWHM. The only free parameter left as input to model is η_{L-e}.

As already mentioned, Nilson *et al.* [42, 43, 85] infer an η_{L-e}=0.2, over the intensity range $I_L = 10^{18} - 10^{21}$ W/cm^2.

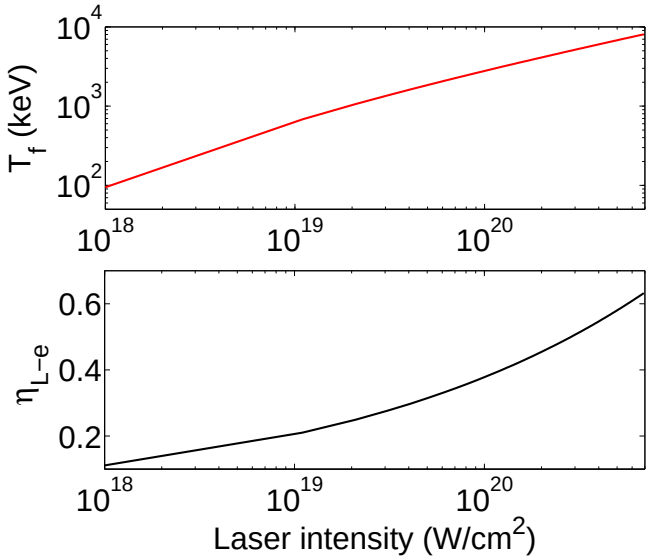

Figure 7.7: Laser-to-electron energy conversion energy published in [84] as function of the laser intensity; T_f as function of the laser intensity deduced from the ponderomotive scaling.

By contrast, the review paper made by Davies [84] on the laser absorption by overdense plasmas highlights a scaling of the fast electron absorption with the laser intensity, shown in figure (7.7), given by:

$$f_{abs} = \left[I_L\lambda_L^2/4.3\times10^{21}(Wcm^{-2}\mu m^2)\right]^{0.2661}$$

This scaling comes from a fit made over wide a range of experimental data under different interaction conditions, including data obtained at pulse contrast ratio between 10^3 and 10^8.

7.3.1 100 μm-thick targets

Figure (7.8) shows model results obtained using a fixed η_{L-e} and the $K\alpha$ lateral extent shown in figure (7.1), to estimate the fast electron beam density. Diamond symbols represent the calculated maximum proton energy at given η_{L-e} and ion acceleration time specified in the figure.

As can be seen in figure (7.8), by allowing both η_{L-e} and τ_{acc} to vary (as free parameters not experimentally measured) there are various different combinations which provide a good fit to the measured data.

Model results using the $\eta_{L-e}(I_L)$ scaling with intensity presented in [84] are also shown in the same figure. The fast electron beam density is calculated using the $K\alpha$ lateral extent. The values of $\eta_{L-e}(I_L)$ obtained using the scaling published in [84] are within the range $\sim 0.2-0.4$. $\eta_{L-e}(I_L)$ coupled with $\tau_{acc} = 1.6$ ps provide a theoretical E_{max} trend in good agreement with the experiments.

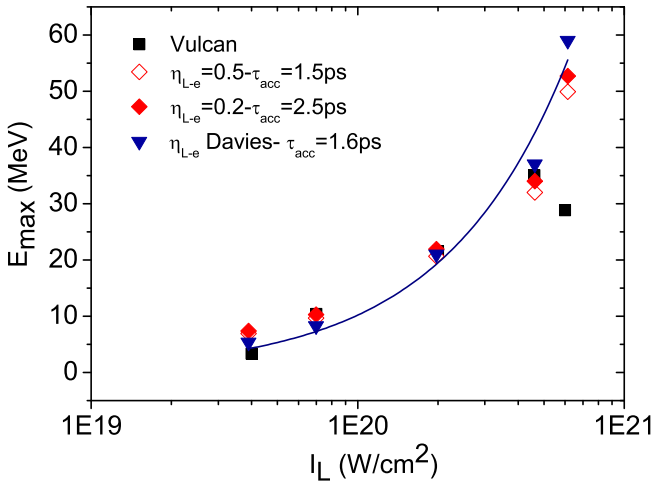

Figure 7.8: Proton maximum energy as a function of the laser intensity using the Vulcan laser. The diamond symbols represent model results obtained for a fixed η_{L-e} and τ_{acc} using the $K\alpha$ lateral extent, shown in figure (7.1), to estimate the fast electron beam density. Triangles are model results using $\eta_{L-e} = [I_L\lambda_L^2/4.3\times10^{21}(Wcm^{-2}\mu m^2)]^{0.2661}$, presented in Davies [84].

7.3.2 20 μm-thick targets

As images of the $K\alpha$ emission were not measured during the Phelix laser experimental campaign, the analytical model is only applied on the published work of Robson *et al.* [192] using measurements of the $K\alpha$ emission, summarized in table (7.2), performed on the same laser and close experimental conditions.

During the interaction of picosecond laser pulses with thin targets, previous publications [122, 182, 183] have shown that fast electron recirculation leads to an enhancement of the proton maximum energy. Mora's isothermal model does not take into account the finite size of the target (and the electron recirculation) however the work of Perego *et al.* [139], comparing different TNSA acceleration analytical models, shows that Mora's isothermal model provides a trend with the laser intensity close to experiments over a wide range of experimental conditions.

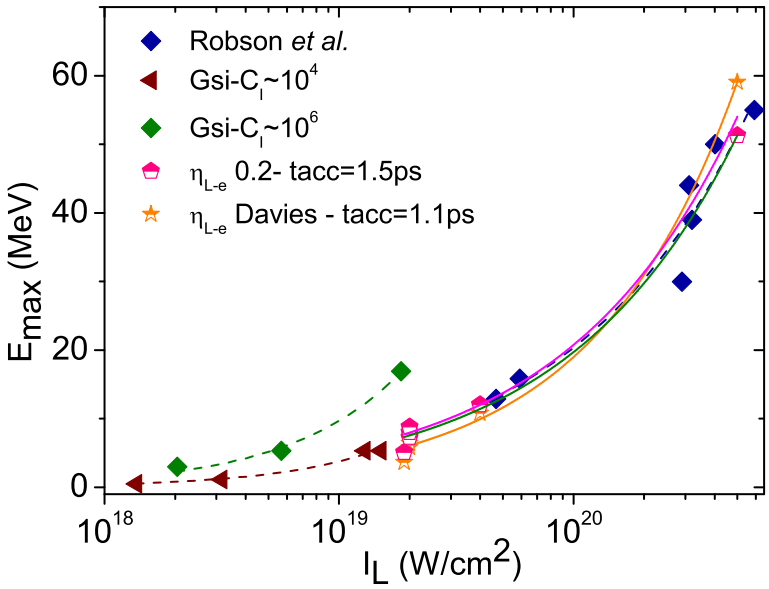

Figure 7.9: Proton maximum energy as a function of the laser intensity. The diamond and triangles symbols represent model results obtained for a fixed η_{L-e} and τ_{acc} using the $K\alpha$ lateral extent summarized in table (7.2), to estimate the fast electron beam density.

The proton maximum energy measured on the Phelix laser scales with $\sim I_L^{0.9}$ indicating that a combination of different mechanisms is responsible for the hot electron acceleration. The work of Cai *et al.* [18] and Mishra *et al.* [206] also observed a change in the fast electron energy distribution, from a single to a two temperature energy distribution function, for middle density scale length. However, the scaling in $\sim I_L^{0.6}$ found in Robson *et al.*, shows a domination of the ponderomotive acceleration. Therefore, the fast electron beam mean temperature used as input in the isothermal expansion model is deduced from the ponderomotive scaling.
Figure (7.9) presents the predicted E_{max}. As for 100 μm-thick targets, several combinations of η_{L-e} and τ_{acc} are found in order to obtain an E_{max} trend close to the experimental E_{max}. For example, an ion acceleration time of the order of the laser pulse duration and an $\eta_{L-e} \sim 0.2$ reproduce the experimental trend published in Robson *et al.* [192].

As a first conclusion from this simple model predicting the maximum proton energy for experimental results obtained with high laser pulse contrast ratio, a conversion efficiency between ~ 0.2 and 0.5, coupled with an ion acceleration time ranging from ~ 1 to 2.5 ps, reproduce the experimental results. Using the η_{L-e} scaling with I_L (ranging from $\sim 0.2-0.4$) of Davies [84] as input to Mora's isothermal model provides an E_{max} trend with I_L close to experiments, when coupled with an ion acceleration time ranging from ~ 1 to 1.6 ps. Further investigations are performed in the next section with hybrid-PIC simulations.

7.4 Hybrid simulation results

The 3D hybrid code ZEPHYROS is used to simulate fast electron beam transport in solids. The fast electron beam density and an acceleration time deduced from simulations at a given η_{L-e}, as discussed in chapter (5), are used as inputs to the Mora's 1D model in order to obtain an E_{max} trend close to that observed in the experiments. This enables, as for the analytical model presented above, to

approximate η_{L-e} indirectly and to compare with the analytical model.

In both sets of simulations the parameters used are as follows: A 500 μm $\times$ 500 μm $\times$ L μm box with grid size equal to 2 μm $\times$ 2 μm $\times$ 2 μm. The beam temperature is given by the ponderomotive scaling [63] (thus the laser intensity), and the electrons are injected into the solid over a pulse duration of 1 ps, in a focal spot (Gaussian transverse profile & top hat temporal profile) with radius equal to 4 μm. The laser intensity, setting T_f, is chosen to match the experimental conditions. The electron energy distribution is given by $N_f(E_e) = N_f exp(-E_e/T_f[eV])$. The angular-energy injection distribution, derived by Moore *et al.* [60], is: $\theta_{1/2} = \tan^{-1}[\alpha \times \sqrt{2/(\gamma-1)}]$. Then, the fast electrons with energy (E_e) are injected within the cone of half-angle $\theta_{1/2}(E_e)$. The electron source diameter is set equal to the laser vacuum focal spot diameter. The initial background temperature is set at 1 eV.

7.4.1 Simulations of fast electron transport in 100 μm-thick Al targets

For the runs made at L =100 μm, the front and rear boundaries are reflective and side boundaries are open. The Al resistivity curve used is the one employed by Davies [107].

By setting η_{L-e}=0.2 and injecting the fast electrons within a large cone of mean half angle equal to 50^0, an E_{max} trend, presented in figure (7.10), close to that measured experimentally is obtained.

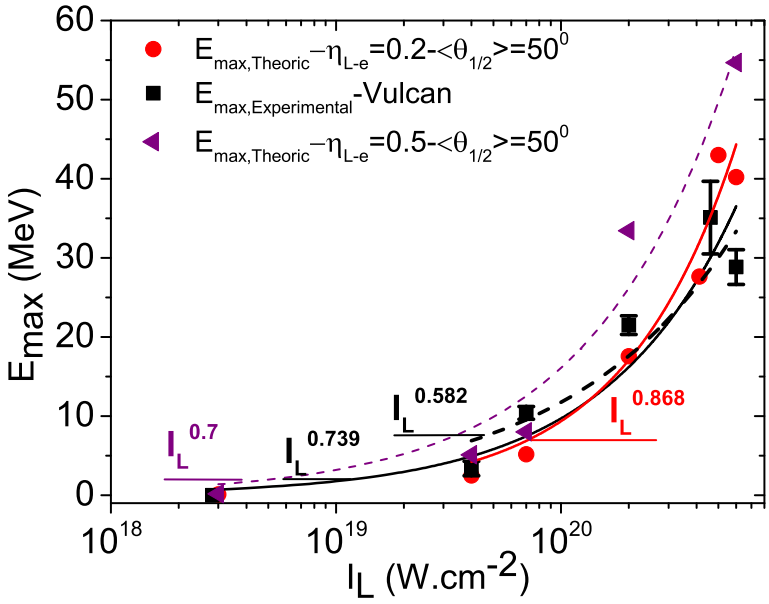

Figure 7.10: E_{max} deduced from the simulation outputs as function of the laser intensity.

7.4.2 Simulations of fast electron transport in 20 μm-thick targets

The runs are made at L =20 and 25 μm. The front boundary is reflective, the rear boundary is open or reflective and the side boundaries are open. Unless specified, the results shown in this section are obtained using η_{L-e}=0.2 and $< \theta_{1/2} >= 50^0$. The Hybrid-PIC code models the collisional and resistive beam transport in a Al and Cu targets. As a Cu/Ni alloy material is not implemented in the code, the experimental results obtained on Cu/Ni alloy targets are compared with the numerical results obtained in Cu targets using Lee More resistivity model [49].

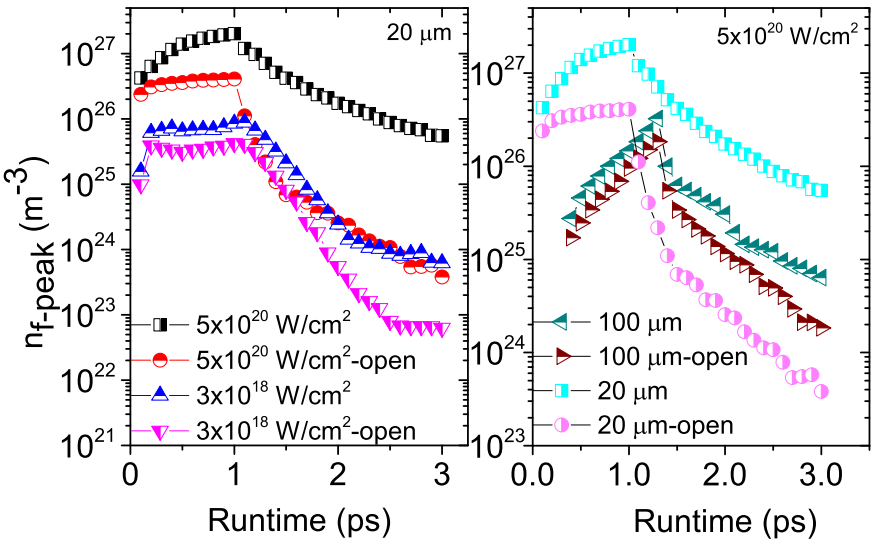

Figure 7.11: Comparison of the peak fast electron rear-side density obtained in Al targets for an open (labeled 'open') or reflective x-axis rear boundary, as function of the simulation runtime. The temporal evolution is compared at different laser intensity.

The effect of the fast electron beam recirculation, in Al targets, on the density at the simulation rear boundary is investigated by changing the x-axis rear boundary from a reflective to an open boundary. The temporal evolution of the peak density for both boundary conditions is shown in figure (7.11). For 100 μm-thick targets the beam recirculation does not affect the density at the target rear boundary as the fast electrons recirculate once in the background plasma and spread out from the propagation axis. In 20 μm-thick targets, the effect of recirculation is clearly seen especially for the run made at a laser intensity of $5\times\ 10^{20}$ W.cm^{-2} and at a runtime later than 1 ps when the 'laser' is off. The recirculation enhances by 2 order of magnitude the beam peak density at the target rear surface. At laser intensity of $3\times\ 10^{18}$ W.cm^{-2}, the fast electron beam is less collimated as the B-field strength is lower (due to the lower energy and hence fast electron current density) than for the run made at higher laser intensities, thus the fast electrons spread out from the propagation axis and the beam recirculation has little effect upon the density at the rear boundary.

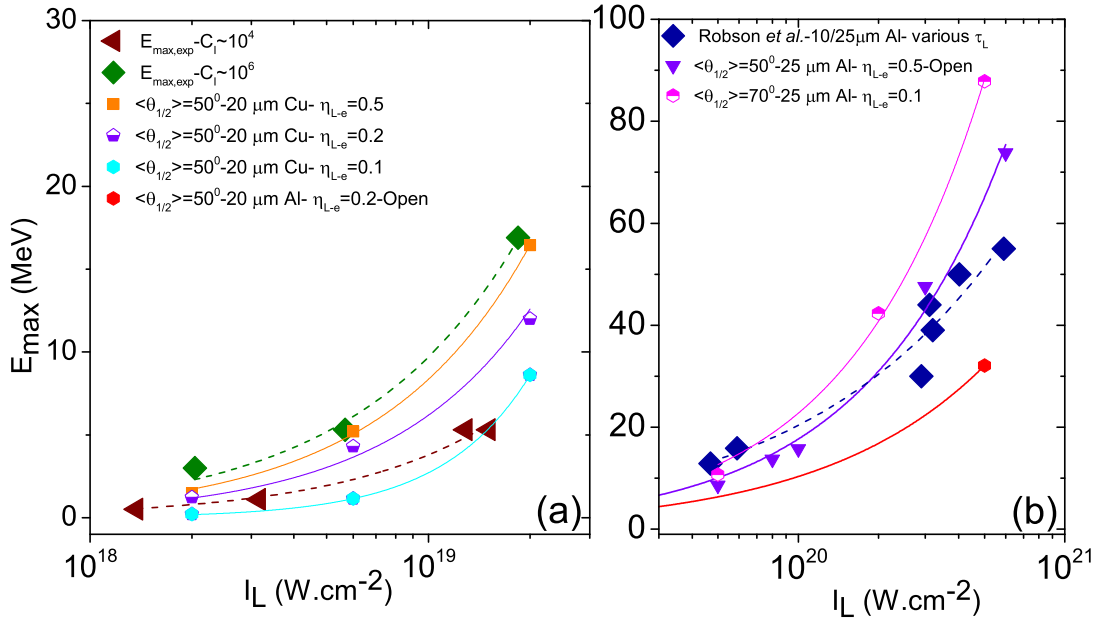

Figure 7.12: E_{max} deduced from the simulation outputs as a function of the laser intensity.

The numerical results shown in figure (7.12(a)) are obtained using input parameters relevant to the Phelix laser. As can be seen, η_{L-e} need to be increased for a intermediate preplasma density scale length when compared to a larger scale length, at a given injection half-angle, in order to reproduce the maximum proton energy trend measured experimentally. Figure (7.12(b)) shows the numerical results obtained, at a given fast electron distribution function, for input parameters relevant to the Vulcan laser. A close E_{max} trend to the experimental results of Robson *et al.* is found for an injection half-angle of $< \theta_{1/2} > \sim 70°$ and an $\eta_{L-e} \sim 0.1$, similar to the laser-to-electron energy conversion efficiency inferred by [41, 121]. However, as mentioned previously, there might be several combinations of $< \theta_{1/2} >$ and η_{L-e} which could provide a close trend to experiments. Furthermore, the preplasma density scale length can also change the injection angle [20]. Therefore, a future work would be to measure experimentally one or both of those parameters.

Note that the presence of a middle/large preplasma density scale length (of the order of a tens of microns) expanding at the target front surface, can lead to an enlargement of the fast electron source size. The fast electron absorption mechanisms and thus the fast electron energy distribution can also vary under different laser-preplasma interaction conditions. Furthermore, the recirculation of fast electrons also affects the proton maximum energy. As those effects have not been investigated for the 20 μm-thick targets, the relative changes in η_{L-e} values, between the 3 experimental sets deduced from both analytical and numerical models, are only compared.

7.5 Summary & future work

The work presents an experimental investigation, using two diagnostics of the fast electron beam size and density simultaneously coupled with 1D analytical models and numerical results from a hybrid-PIC code, of the laser-to-fast electron energy conversion efficiency. It is found that the laser-to-fast electron energy conversion efficiency is strongly sensitive to the laser-solid interaction conditions (by variation of the laser pulse contrast ratio).

Mishra *et al.* [206] observed an increase in the absorption with an increase in the laser amplitude, therefore a higher η_{L-e} can be expected for the results obtained on the Vulcan laser as compared to the Phelix laser. Based on the work of Cai *et al.* [18] and Mishra *et al.* [206], in the presence of preformed plasma the laser absorption is enhanced. Thus, for example, the contrast ratio on Phelix laser, being high enough to generate a preplasma at the target front surface and depending on the preplasma density scale length as shown in McKenna *et al.* [83], the laser energy absorption should be improved relative to that can be achieved when the laser pulse interacts with a steep density gradient. However, at long preplasma expansion, laser plasma instabilities dominate, altering the laser energy coupling to hot electrons, explaining the fall in η_{L-e} at a given laser intensity. The increase in the proton maximum energy, when the contrast was enhanced from 10^4 to 10^6,

suggests that η_{L-e} is also improved for a contrast ratio of 10^6.

It can be noticed that the scaling of the proton maximum energy with the laser intensity varies with the laser pulse intensity and contrast ratio. For a laser contrast ratio ranging from 10^4 to 10^6, E_{max} scales with $I_L^{\sim 0.9}$. For a higher contrast ratio of 10^9 (and higher laser intensities) E_{max} scales with $I_L^{\sim 0.6}$. The difference in E_{max} scaling may indicate a change in the fast electron acceleration mechanism with the preplasma scale length, as E_{max} is proportional to the fast electron temperature (the scaling of the temperature with the laser intensity is set by the acceleration mechanism). Additional PIC simulations of the interaction of the laser with different preplasma scale lengths would complete this analysis by extracting the characteristics (energy distribution, angular distribution etc...) of the fast electrons injected in the overdense background plasma at the critical density. The required detailed PIC simulations are beyond the scope of this project and the computational resources available, but will form the basis of future work.

This work highlights the importance of the laser contrast ratio and the laser generated preplasma expanding at the target front surface, on certain aspects of hot electron beam production. A future work could include measuring, the laser-to-hot electron energy conversion efficiency, the fast electron beam divergence and the scaling of the fast electron temperature with a controlled preformed plasma scale length. As observed in the numerical simulations published in [18, 78, 206], the fast electron energy distribution, varies from an apparent single temperature to two temperature distribution function and is highly sensitive to the preformed plasma as the absorption and acceleration mechanisms are strongly dependent on the laser- preformed plasma/solid interaction. Control of the preformed plasma may enable the fast electron beam properties to be tailored to application.

In laser short preplasma scale length interaction, the fast electron spectrum presents an average temperature of few MeVs, favorable for the fast ignition concept. By increasing the preformed plasma scale length, the number of electrons generated within the coronal plasma increases (However, the beam divergence also increases [20]). In addition, the fast electron beam temperature is enhanced by the contribution of several absorption/acceleration mechanisms to the elec-

trons acceleration (especially when the laser impinges obliquely on the target). Consequently, the secondary X-ray emission and the characteristics of the TNSA-generated proton beam can be optimized by a controlled laser-preplasma interaction.

Chapter 8

Conclusion & outlook

This work, motivated by the fast ignition approach to ICF and laser-driven ion acceleration, reports on the investigation of the properties and the control of fast electron beams generated in UHI laser-solid interactions. The generation and control of fast electrons, which has been an active area of research in plasma physics for more than a decade, is far from being entirely understood. A major experimental difficulty is that there is no direct measurement of the fast electron beam traveling through a solid. Therefore indirect diagnostics are employed which increases the uncertainty associated with the observations. However, the intensive experimental and theoretical research activities carried out on laser-plasma interactions provides much useful information on the laser-generated fast electron beam. For example, the main acceleration mechanisms of fast electron have been identified, enabling the fast electron beam temperature to be inferred. The beam spatial distribution, spectrum, injection efficiency and transport are all still topics of active investigation. In addition to the experimental challenge of controlling the fast electron beam, new diagnostics and improvements to the drive laser have enabled some positive developments. For example, better control of laser prepulse has enabled some optimisation of coupling to the solid target to be achieved. On the diagnostics front, in addition to more conventional x-ray diagnostics, TNSA ion beam based diagnostics have enabled new types of measurements to be made that increase our understanding of the structure and

propagation of the electron beam in the target. Furthermore, a major advance in computing power enables the use of computationally demanding numerical models, such as multidimensional kinetic models. Kinetic, fluid and hybrid codes, can provide information on, for example, the effect of self-generated field on the fast electron beam and also on beam-plasma instabilities. However, even if numerical simulations are a key tool for the understanding of many phenomena in overdense plasma, the use of only 1 or 2 spatial dimensions (due to limitations on computational resources), the assumptions used, the reduced spatial and/or temporal scales employed relative to the real targets, and the presence of numerical noise can make interpretation of the results of such simulations difficult. Therefore, it is essential to benchmark numerical results with experiments. This thesis presents experimental investigations of laser-generated fast electrons in solids, based on X-ray and ions diagnostics, combined with numerical simulations:

→ In chapter 5, a new approach is employed to investigate the fast electron beam injection and divergence angles in 100-500 μm-thick Al targets. Simultaneous measurements of the TNSA-generated proton beam and X-ray emission from a Cu buried layer are used as diagnostics for the fast electron beam size at the target rear surface. The laser pulse contrast ratio was higher than 10^9 on a nanosecond time scale. The fast electron beam injection angle is inferred from hybrid-PIC simulations via series of runs made at a given beam injection half-angle and target thickness. Hybrid simulations showed that the half-angle of $\sim 27^\circ$ corresponding to the effective beam *transport* angle inferred from the X-ray diagnostic, corresponds to an effective electron beam divergence angle, which is determined by the magnitude of self-generated fields. The measured proton cutoff energy trend, *i.e.* the fact that E_{max} decreases with increasing target thickness, is reproduced when *injection* half-angles of $\sim 50^\circ$ ($\eta_{L-e} \sim 0.2$) and $\sim 70^\circ$ ($\eta_{L-e} \sim 0.4$) are used.
Finally, the main data set is compared with results obtained with Au targets at tight focus, and, with Al targets at a laser defocused spot size equal to 60 μm. The transport half-angle for a large laser spot, inferred from the Cu $K\alpha$ lateral extent, is equal to $\sim 33^\circ$, which is of the same order as that inferred with the

beam in tight focus. The proton maximum energy, with the peak energy achieved at tight focus in thin Al targets, decreases more rapidly in Au as compared to Al. Geant4 simulations show important scattering in Au target, increasing with the simulation box thickness. This leads to a quick drop in the fast electron beam density and, consequently, the proton maximum energy also decreases with the beam density when the propagation layer thickness is increased. As for Al targets, hybrid simulations coupled with plasma expansion calculations show that large injection half-angles, between $\sim 50°$ and $\sim 70°$ ($\eta_{L-e} \sim 0.2 - 0.5$), are required in order to match the experimental maximum proton energy. No clear changes in the proton maximum energy trend are observed from the runs made at larger source radius. Further work on this topic includes simulations with much larger laser spot sizes, of the order of the sizes achieved experimentally. This requires more computation resources than available for the present study.

→ In chapter 6, the effect of the laser spot size on the fast electron beam, and consequently on the TNSA-generated protons, is reported. Two scans were performed, at a given laser intensity, by varying the laser energy (3-150 J) for a fixed irradiated spot size (8 μm) and by varying the spot size (8-80 μm) for a fixed energy (150 J). The TNSA-generated proton beam and X-ray emission from a Cu buried layer are used as diagnostics for the fast electron beam size at the target rear surface. Measurements of the lateral extent of the Cu Kα show small variations, at a given laser intensity, for both scans. This indicates that, after propagating in 100 μm-thick Al targets, the overall envelope of the fast electron beam (including keV energy electrons) is not strongly affected by the source size. Therefore, no conclusion can be made concerning a possible enlargement of the rear sheath field diameter for defocused laser irradiation.
The peak maximum proton energy is achieved at the highest laser intensity. However, at a given intensity, the maximum proton energy and the laser-to-proton energy conversion efficiency are measured to be generally higher under defocused laser irradiation and laser energy equal to 150 J, when compared to tight focus and lower laser energies. It was also observed that the number of 'low' energy protons is enhanced under defocused laser irradiation. The proton maximum energy

is proportional to $I_L^{\sim 0.6}$, for the experimental results presented in this thesis and for the published results, obtained by variation of the laser pulse spot size. An E_{max} plateau is observed for the focus scan, with E_{max} scaling with $I_L^{\sim 0.13}$. The enhanced proton maximum energy, under defocused laser irradiation, is explained in terms of geometrical changes of the accelerating sheath field in addition to the increased laser energy. The formation of a parabolic-like sheath distribution, is in turn explained by the use of a new fast electron source model, in which the fast electrons are injected from a diffuse source model.

→ In chapter 7, the effect of the ASE-generated preplasma on the laser energy coupling to fast electrons is investigated over a wide range of parameters. The measurement are made over a wide range of laser pulse contrast ratios, from 10^4 to 10^9 (ASE level on a nanosecond timescales). Therefore, a short, intermediate and long preplasma density scale length is generated at the target front surface. It is found that the proton maximum energy is enhanced, at a given laser intensity, for a pulse contrast ratio of C_I=10^6 when compared to a pulse contrast ratio of 10^4. This can be explained by the generation of a longer preplasma density scale length. Therefore laser pulse propagation instabilities appear in the underdense plasma region and the laser beam breaks into filaments before reaching the critical surface. The highest E_{max} is obtained at the highest laser intensity. However, the E_{max} trend seems to be enhanced for the data set obtained in presence of a intermediate preplasma density scale length (C_I=10^6). Furthermore, the E_{max} results obtained for 100 μm-thick Al targets are compared to those obtained for 20 μm-thick Al targets at similar experimental conditions. It was also found that a higher maximum energy is achieved when thinner targets are employed.
Numerical simulations in Al, using a hybrid code, enable the laser-to-electron energy conversion efficiency to be inferred, for a fixed fast electron injection angle, for the experimental results obtained for Al targets. The experimental results obtained on Cu/Ni alloy targets are compared with the numerical runs using Al (lower Z) and Au (higher Z) targets. The use of an injection half-angle of $\sim 50^\circ$ and an η_{L-e}=0.2 reproduces the experimental E_{max} for 100 μm-thick Al targets. As for the 20 μm-thick Al targets, the fast electron beam recirculation

enhances the proton maximum energy, when compared to the 100 μm-thick Al targets at a given laser intensity. It was found that employing a wider injection half-angle of $\sim 70^{\circ}$ and an η_{L-e}=0.1 provided a closer match to the trend seen in the experimental data. As expected, a much lower η_{L-e}, at a given injection half-angle, is required to obtain the E_{max} trend in presence of a long preplasma density scale length when compared to the results obtained in presence of a intermediate density scale length. However, it is noted that there is more than one solution to the unmeasured free parameters, energy conversion to fast electrons and the fast electron injection angle, to fit the experimental results. Therefore, further investigation should focus on employing additional diagnostics to help determine this parameters.

The role of the different parameters defining the laser-solid interaction, for example the influence of the preplasma on the fast electron beam spectra or divergence, is an area of active investigation. The self-generated fields, altering the beam propagation in the overdense plasma, can also potentially be controlled. For example, by an appropriate choice of the target structure or via two collinear laser pulses, the first pulse generating and acceleration in the solid a 'first population of electrons' that in turn generates fields in the overdense plasma capable of guiding the main fast electron beam generated by the second pulse [208].
The investigations presented in this thesis confirm some of the latest results reported by other authors in this field and address some open questions related to the generation and control of fast electrons. The work reported demonstrates that:
(1) an optimized preplasma density scale length leads to an enhancement of the laser energy coupling into fast electrons (and therefore also to protons),
(2) the laser spot size influences the fast electron beam injection angle and transport, by altering the self-generated field strength at the source. A change in the fast electrons and TNSA-generated ions energy spectrum (with an enhancement of the proton flux) is also observed,
(3) self-generated resistive magnetic fields are a key factor in fast electron beam transport that can be used to control the fast electron beam whilst it is traveling

in the overdense plasma,

Further investigations are needed to be able to systematically control the fast electron beam characteristics both at its source and during its propagation through the overdense plasma. It is shown in chapter 7, that an optimized preplasma density scale length enhances the laser energy absorption. However, the 'scaling' of the preplasma density scale length with the laser parameters remains approximate. Knowing more precisely the 'scaling' of the density scale length, with respect to the laser parameters, will enable the laser energy coupling to fast electrons to be optimized, and will also enable the shape of the fast electron energy spectrum and beam divergence around the critical density to be controlled. The effect of self-generated fields on the fast electron beam propagation, reported in chapter 5, is extensively investigated. However, for example, the self-generated field, responsible for the fast beam collimation at the fast electron source (i.e. the critical density region), depends on the source size as observed in chapter 6. This needs further investigation to experimentally demonstrate the scaling of the magnetic field strength with the source radius. Note that those self-generated fields have been only observed in numerical simulations. One of the major difficulties in measuring the fast-electron beam-size in an overdense medium, is that the X-ray 2D imager is mainly sensitive to 10s of keV electrons. Therefore, the measurements obtained from this diagnostic do not enable a proper characterization of the multi-MeV electron-beam-diameter, nor do they enable magnetic pinching to be observed. A new imaging technique, sensitive to higher energy electrons, will enable the beam divergence or pinching to be more accurately inferred, as well as allowing for beam-plasma instabilities to be recorded. The need for high-energy imaging diagnostics will become more pronounced as laser powers approach 10PW and new tight-focusing off-axis parabolas enable these beams to be focused down to unprecedented intensities.

Bibliography

[1] M. Coury *et al.* Influence of laser irradiated spot size on energetic electron injection and proton acceleration in foil targets. *Appl. Phys. Lett.*, **100**: 074105, 2012.

[2] M. Coury *et al.* Injection and transport properties of fast electrons in ultraintense laser-solid interactions. *Phys. Plasmas*, 20(4):043104, 2013.

[3] D. Strickland and G. Mourou. Compression of amplified chirped optical pulses. *Opt. Commun.*, **56**: 219, 1985.

[4] M. Tabak *et al.* Ignition and high gain with ultra powerful lasers. *Phys. Plasmas*, **1**: 1626, 1994.

[5] K. Wharton *et al.* Experiment vs. theory on electric inhibition of fast electron penetration of targets. *Phys. Rev. Lett.*, **81**, 1998.

[6] R. Kodama *et al.* Fast heating of ultrahigh-density plasma as a step towards laser fusion ignition. *Nature*, **412**: 798, 2001.

[7] H. Schwoerer *et al.* Mev x rays and photoneutrons from femtosecond laser-produced plasmas. *Phys. Rev. Lett.*, **86**:2317–2320, Mar 2001.

[8] S. C. Wilks *et al.* Energetic proton generation in ultra-intense laser solid interaction. *Phys. Plasmas*, **8**: 2, 2001.

[9] P. K. Patel *et al.* Isochoric heating of solid density matter with ultrafast proton beam. *Phys. Rev. Lett.*, **91**: 125004, 2003.

[10] A. Macchi *et al.* Ion acceleration by superintense laser-plasma interaction. *Rev. Mod. Phys.*, accepted for publication 2013.

[11] D. E. Hinkel *et al.* Stimulated raman scatter analyses of experiments conducted at the national ignition facility. *Phys. of Plasmas*, **18**(5):056312, 2011.

[12] `http://www.generalfusion.com`.

[13] S. Atzeni *et al.* *The physics of inertial fusion.* Oxford University Press, 2004.

[14] K. L. Lancaster *et al.* Measurements of energy transport patterns in solid density laser plasma interactions at intensities of 5×10^{20} wcm^{-2}. *Phys. Rev. Lett.*, **98**: 125002, 2007.

[15] J. S. Green *et al.* Effect of laser intensity on fast-electron-beam divergence in solid-density plasmas. *Phys. Rev. Lett.*, **100**: 015003, 2008.

[16] P. McKenna *et al.* Effect of lattice structure on energetic electron transport in solids irradiated by ultraintense laser pulses. *Phys. Rev. Lett.*, **106**: 185004, May 2011.

[17] M. Storm *et al.* High-current, relativistic electron-beam transport in metals and the role of magnetic collimation. *Phys. Rev. Lett.*, **102**:235004, Jun 2009.

[18] Cai Hong bo *et al.* Prepulse effects on the generation of high energy electrons in fast ignition scheme. *Phys. Plasmas*, **17**(2): 023106, 2010.

[19] S. D. Baton *et al.* Inhibition of fast electron energy deposition due to preplasma filling of cone-attached targets. *Phys. Plasmas*, **15**(4): 042706, 2008.

[20] V. M. Ovchinnikov *et al.* Effects of preplasma scale length and laser intensity on the divergence of laser-generated hot electrons. *Phys. Rev. Lett.*, **110**:065007, 2013.

[21] J. C. Adam *et al.* Dispersion and transport of energetic particles due to the interaction of intense laser pulses with overdense plasmas. *Phys. Rev. Lett.*, **97**:205006, Nov 2006.

[22] L. Gremillet *et al.* Filamented transport of laser-generated relativistic electrons penetrating a solid target. *Physics of Plasmas*, **9**(3):941–948, 2002.

[23] J. R. Davies *et al.* Magnetic focusing and trapping of high-intensity laser-generated fast electrons at the rear of solid targets. *Phys. Rev. E*, **59**: 6032–6036, 1999.

[24] A. R. Bell *et al.* Resistive collimation of electron beams in laser-produced plasmas. *Phys. Rev. Lett.*, **91**: 035003, 2003.

[25] A. R. Bell *et al.* Fast electron transport in high intensity short pulse laser solid experiments. *Plasma Phys. Control. Fusion*, **39**: 653, 1997.

[26] J J Honrubia *et al.* Fast ignition of fusion targets by laser-driven electrons. *Plasma Phys. Control. Fusion*, **51**(1): 014008, 2009.

[27] D. Hiroyuki *et al.* Review of laser-driven ion sources and their applications. *Reports on Progress in Physics*, **75**(5):056401, 2012.

[28] T. Bortfeld. An analytical approximation of the bragg curve for therapeutic proton beams. *Medical Physics*, **24**(12):2024–2033, 1997.

[29] M. Goitein *et al.* Treating cancer with protons. *Physics Today*, **55**(9):45–50, 2002.

[30] S. V. Bulanov and V. Khoroshkov. Feasability of using laser ion accelerators in proton therapy. *Plasmas Phys. Rep.*, **28**: 453, 2002.

[31] S. V. Bulanov *et al.* Interaction of electromagnetic waves with plasma in the radiation dominated regime. *Plasma Phys. Reports*, **30**: 196–213, 2004.

[32] E. Fourkal and C. Ma. Laser accelerated carbon ion beams. *Medical Physics*, **30**: 1448, 2003.

[33] E. Fourkal *et al.* Energy and intensity modulated radiation therapy using laser accelerated proton beams. *Medical Physics*, **31**: 1884, 2004.

[34] V. Malka *et al.* Practicability of proton therapy using compact laser systems. *Medical Physics*, **31**: 1587, 2004.

[35] G. M. Dyer *et al.* Equation-of-state measurement of dense plasmas heated with fast protons. *Phys. Rev. Lett.*, **101**:015002, Jul 2008.

[36] M. Roth *et al.* Fast ignition by intense laser accelerated proton beams. *Phys. Rev. Lett.*, **86**: 436, 2001.

[37] Y. Sentoku *et al.* High density collimated beams of relativistic ions produced by petawatt laser pulses in plasmas. *Phys. Rev. E*, **62**: 7271, 2000.

[38] S. P. Hatchett *et al.* Electron, photon, and ion beams from the relativistic interaction of petawatt laser pulses with solid targets. *Phys. Plasmas*, **7**: 2076, 2000.

[39] C. Courtois *et al.* High-resolution multi-mev x-ray radiography using relativistic laser-solid interaction. *Phys. of Plasmas*, **18**(2):023101, 2011.

[40] M. D. Perry *et al.* Hard x-ray production from high intensity laser solid interactions (invited). *Review of Scientific Instruments*, **70**(1):265–269, 1999.

[41] W. Theobald *et al.* Hot surface ionic line emission and cold k-inner shell emission from petawatt-laser-irradiated cu foil targets. *Phys. Plasma*, **13**(4):043102, 2006.

[42] P. M. Nilson *et al.* Scaling hot-electron generation to high-power, kilojoule-class laser-solid interactions. *Phys. Rev. Lett.*, **105**: 235001, 2010.

[43] P. M. Nilson *et al.* Time-resolved measurements of hot-electron equilibration dynamics in high-intensity laser interactions with thin-foil solid targets. *Phys. Rev. Lett.*, **108**: 085002, Feb 2012.

[44] W. L. Kruer. *The Physics of Laser Plasma Interactions (Frontiers in Physics)*. Westview Press; New edition edition (8 Jan 2003), 2003.

[45] B. Ersfeld. Plasma physics. Strathclyde university,University Lecture, 2007.

[46] S. Bale. Laser-driven plasma-based acceleration-theory of laser-plasma interaction. University of California, Berkeley,University Lecture, 2012.

[47] L. Spitzer and R. Härm. Transport phenomena in a completely ionized gas. *Phys. Rev.*, **89**: 5, 1953.

[48] H. M. Milchberg*et al.* Resistivity of a simple metal from room temperature to 10^6 k. *Phys. Rev. Lett.*, **61**: 2364–2367, Nov 1988.

[49] Y. T. Lee *et al.* An electron conductivity model for dense plasmas. *Physics of Fluids*, **27**(5):1273–1286, 1984.

[50] L. V. Keldysh *et al. Zh. Eksp. Teor. Fiz.*, **47**:1945, 1964.

[51] V. S. Popov. Tunnel and multiphoton ionization of atoms and ions in a strong laser field (keldysh theory). *Physics-Uspekhi*, **47**(9):855, 2004.

[52] J. S. Cohen. Reexamination of over-the-barrier and tunneling ionization of the hydrogen atom in an intense field. *Phys. Rev. A*, 64:043412, Sep 2001.

[53] M. V. Ammosov *et al.* Tunnel ionization of complex atoms and of atomic ions in an alternating electromagnetic field. *Sov. Phys. JETP*, **64**: 6, 1986.

[54] J. N. Bardsley *et al.* Relativistic dynamics of electrons in intense laser fields. *Phys. Rev. A*, **40**:3823–3835, Oct 1989.

[55] E. Esarey *et al.* Laser acceleration of electrons in vacuum. *Phys. Rev. E*, 52:5443–5453, 1995.

[56] A. Macchi. An introduction to ultraintense laser-plasma interactions. Universita di Pisa ,University Lecture, 2011.

[57] P. Gibbon. *Short pulse laser interaction with matter, an introduction.* Imperial College Press, 2005.

[58] F. V. Hartemann *et al.* Nonlinear ponderomotive scattering of relativistic electrons by an intense laser field at focus. *Phys. Rev. E*, **51**:4833–4843, May 1995.

[59] P. Mora *et al.* Kinetic modeling of intense, short laser pulses propagating in tenuous plasmas. *Phys. of Plasmas*, **4**:217, 1997.

[60] C. I. Moore *et al.* Observation of the transition from thomson to compton scattering in multiphoton interactions with low-energy electrons. *Phys. Rev. Lett.*, **74**: 2439–2442, Mar 1995.

[61] A. Pukhov. Laser hole boring into overdense plasma and relativistic electron currents for fast ignition of icf targets. *Phys. Rev. Lett.*, **79**:2686–2689, Oct 1997.

[62] H. C. Kapteyn *et al.* Prepulse energy suppression for high-energy ultrashort pulses using self-induced plasma shuttering. *Opt. Lett.*, **16**(7):490–492, Apr 1991.

[63] S. C. Wilks *et al.* Absorption of ultrashort, ultra-intense laser light by solids and overdense plasmas. *IEEE Journal of Quantum Electronics*, **33**: 1954–68, 1997.

[64] E. Lefebvre *et al.* Transparency/opacity of a solid target illuminated by an ultrahigh-intensity laser pulse. *Phys. Rev. Lett.*, **74**:2002–2005, Mar 1995.

[65] A. B. Borisov *et al.* Stability analysis of relativistic and charge-displacement self-channelling of intenselaser pulses in underdense plasmas. *Plasma Phys. Control. Fusion*, **37**:569–597, May 1995.

[66] H. S. Brandi *et al.* Relativistic and ponderomotive self-focusing of a laser beam in a radially inhomogeneous plasma. i. paraxial approximation. *Physics of Fluids B: Plasma Physics*, **5**(10):3539–3550, 1993.

[67] W. Rozmus *et al.* Skin effect and interaction of short laser pulses with dense plasmas. *Phys. Rev. A*, **42**:7401–7412, Dec 1990.

[68] G. J. Pert. Inverse bremsstrahlung in strong radiation fields at low temperatures. *Phys. Rev. E*, **51**:4778–4789, May 1995.

[69] V. L. Ginzburg. *The Propagation of Electromagnetic Waves in Plasmas: @ , by V. L. Ginzburg,... Translated by J. B. Sykes and R. J. Tayler.* New York, Paris, 1964.

[70] D. W. Forslund *et al.* Theory of hot-electron spectra at high laser intensity. *Phys. Rev. Lett.*, **39**:284, 1977.

[71] F. Brunel. Not-so-resonant, resonant absorption. *Phys. Rev. Lett.*, **59**: 52–5, 1987.

[72] P. Gibbon *et al.* Collisionless absorption in sharp-edged plasmas. *Phys. Rev. Lett.*, **68**:1535–1538, Mar 1992.

[73] W. L. Kruer *et al.* J x b heating by very intense laser light. *Phys. Fluids*, **28**(1): 430–432, 1985.

[74] G. Malka *et al.* Experimental confirmation of ponderomotive-force electrons produced by an ultrarelativistic laser pulse on a solid target. *Phys. Rev. Lett.*, **77**:75–78, Jul 1996.

[75] F. N. Beg *et al.* A study of picosecond laser–solid interactions up to 10[sup 19] W cm[sup - 2]. *Phys. of Plasmas*, **4**(2):447–457, 1997.

[76] P.A. Norreys *et al.* Recent fast electron energy transport experiments relevant to fast ignition inertial fusion. *Nuclear Fusion*, **49**(10):104023, 2009.

[77] M. G. Haines *et al.* Hot-electron temperature and laser-light absorption in fast ignition. *Phys. Rev. Lett.*, **102**: 045008, Jan 2009.

[78] R. H. H. Scott *et al.* A study of fast electron energy transport in relativistically intense laser-plasma interactions with large density scalelengths. *Phys. Plasmas*, **19**(5): 053104, 2012.

[79] B. S. Paradkar *et al.* Numerical modeling of fast electron transport in short pulse lasersolid interactions with long scale-length pre-formed plasma. *Plasma Phys. Control. Fusion*, **52**(12): 125003, 2010.

[80] T. Ma *et al.* Effect of pre-plasma on hot electron coupling and propagation in cone attached wire target. *Proc. 31st Eur. Conf. on Laser Interaction with Matter*, 2010.

[81] A. G. MacPhee *et al.* Limitation on prepulse level for cone-guided fast-ignition inertial confinement fusion. *Phys. Rev. Lett.*, **104**: 055002, Feb 2010.

[82] T. Yabuuchi *et al.* Transport study of intense-laser-produced fast electrons in solid targets with a preplasma created by a long pulse laser. *Phys. Plasmas*, **17**(6): 060704, 2010.

[83] P. McKenna *et al.* Effects of front surface plasma expansion on proton acceleration in ultraintense laser irradiation of foil targets. *Laser Part. Beams*, **26**(04): 591–596, 2008.

[84] J. R. Davies. Laser absorption by overdense plasmas in the relativistic regime. *Plasma Phys. Control. Fusion*, **51**(1): 014006, 2009.

[85] P. M. Nilson *et al.* High-intensity laser-plasma interactions in the refluxing limit. *Phys. Plasmas*, **15**: 056308, 2008.

[86] Z. M. Sheng *et al.* Angular distributions of fast electrons, ions, and bremsstrahlung x/ γ-rays in intense laser interaction with solid targets. *Phys. Rev. Lett.*, **85**: 5340–5343, Dec 2000.

[87] M. Sherlock. Universal scaling of the electron distribution function in one-dimensional simulations of relativistic laser-plasma interactions. *Phys. Plasmas*, **16**(10): 103101, 2009.

[88] H. Alfvèn. On the motion of cosmic rays in interstellar space. *Phys. Rev.*, **55**: 425, 1939.

[89] C. Deutsch *et al.* Interaction physics of the fast ignitor concept. *Phys. Rev. Lett.*, **77**:2483–2486, Sep 1996.

[90] G.Z. Moliére. Theorie der streuung schneller geladener teilchen. i. einzel-streuung am abgeschirmten coulomb-field. *Z. Naturforsch*, **2a**: 133–145, 1947.

[91] H. A. Bethe. Molière's theory of multiple scattering. *Phys. Rev.*, **89**:1256–1266, Mar 1953.

[92] B. Nigam *et al.* Theory of multiple scattering: Second born approximation and corrections to molière's work. *Phys. Rev.*, **115**:491–502, Aug 1959.

[93] M. A. Zucker M. J. Berger, J. S. Coursey and J. Chang. Estar, pstar, and astar:. *Computer Programs for Calculating Stopping-Power and Range Tables for Electrons, Protons, and Helium Ions (version 1.2.3)*, ((National Institute of Standards and Technology, Gaithersburg, 2005)).

[94] C. Møller. Zur theorie des durchgangs schneller elektronen durch materie. *Annalen der Physik*, **406**(5):531–585, 1932.

[95] M. Inokuti. Inelastic collisions of fast charged particles with atoms and molecules¯the bethe theory revisited. *Rev. Mod. Phys.*, **43**:297–347, Jul 1971.

[96] H. A. Bethe. Handbuch der physik. *S. Flügge, Ed. (Julius Springer-Verlag, Berlin)*, 24, 1933.

[97] R. M. Sternheimer. Density effect for the ionization loss of charged particles. *Phys. Rev.*, **145**:247–250, May 1966.

[98] F. Rohrlich *et al.* Positron-electron differences in energy loss and multiple scattering. *Phys. Rev.*, **93**:38–44, Jan 1954.

[99] R. M. Sternheimer *et al.* Density effect for the ionization loss of charged particles in various substances. *Phys. Rev. B*, **26**:6067–6076, Dec 1982.

[100] R.M. More. Pressure ionization, resonances, and the continuity of bound and free states. volume **21** of *Advances in Atomic and Molecular Physics*, pages 305 – 356. Academic Press, 1985.

[101] C. K. Li *et al.* Stopping of directed energetic electrons in high-temperature hydrogenic plasmas. *Phys. Rev. E*, **70**:067401, Dec 2004.

[102] A. A. Solodov *et al.* Stopping power and range of energetic electrons in dense plasmas of fast-ignition fusion targets. *Phys. of Plasmas*, **15**(4):042707, 2008.

[103] D. Pines *et al.* A collective description of electron interactions: Ii. collective vs individual particle aspects of the interactions. *Phys. Rev.*, **85**:338–353, Jan 1952.

[104] C. M. Lee *et al.* Electron bremsstrahlung spectrum, 1-500 kev. *Phys. Rev. A*, **13**:1714–1727, May 1976.

[105] H. Coulon. Interactions of particles with matter. Heidelberg University,University Lecture, 2011.

[106] M. Cantone *et al.* Radiation physics for nuclear medicine. *Springer Berlin Heidelberg*, 2011.

[107] J. R. Davies. How wrong is collisional monte carlo modeling of fast electron transport in high-intensity laser-solid interactions? *Phys. Rev. E*, **65**: 026407, Jan 2002.

[108] J. R. Davies. Electric and magnetic field generation and target heating by laser-generated fast electrons. *Phys. Rev. E*, **68**:056404, Nov 2003.

[109] J. R. Davies *et al.* Electron beam hollowing in lasersolid interactions. *Plasma Phys. Control. Fusion*, **48**:1181, 2006.

[110] S. Kar *et al.* Guiding of relativistic electron beams in solid targets by resistively controlled magnetic fields. *Phys. Rev. Lett.*, **102**: 055001, Feb 2009.

[111] A. P. L. Robinson *et al.* Artificial collimation of fast-electron beams with two laser pulses. *Phys. Rev. Lett.*, **100**: 025002, Jan 2008.

[112] B. Ramakrishna *et al.* Laser-driven fast electron collimation in targets with resistivity boundary. *Phys. Rev. Lett.*, **105**: 135001, Sep 2010.

[113] A. P. L. Robinson *et al.* Magnetic collimation of fast electrons produced by ultraintense laser irradiation by structuring the target composition. *Physics of Plasmas*, **14**(8): 083105, 2007.

[114] A. P. L. Robinson *et al.* Focusing of relativistic electrons in dense plasma using a resistivity-gradient-generated magnetic switchyard. *Phys. Rev. Lett.*, **108**: 125004, Mar 2012.

[115] J. R. Davies *et al.* Short-pulse high-intensity laser-generated fast electron transport into thick solid targets. *Phys. Rev. E*, **56**:7193–7203, Dec 1997.

[116] R. V. Lovelace *et al.* Plasma heating by high-current relativistic electron beams. *Phys. Rev. Lett.*, **27**:1256–1259, Nov 1971.

[117] L. Gremillet. PhD in Physics, Ecole Polytechnique,France, 2001.

[118] J. J. Santos *et. al.* Fast electron transport in ultraintense laser pulse interaction with solid targets by rear-side self-radiation diagnostics. *Phys. Rev. Lett.*, **89**:025001, Jun 2002.

[119] H. Chen *et al.* Evidence of enhanced effective hot electron temperatures in ultraintense laser-solid interactions due to reflexing. *Laser and Particle Beams*, **23**:411–416, 9 2005.

[120] E. E. Fill. Ultrashort-pulse laser plasmas: Fraction of hot electrons escaping from the target and electron spectra in planar and spherical geometry. *Phys. of Plasmas*, **12**(5):052704, 2005.

[121] J. Myatt *et al.* High-intensity laser interactions with mass-limited solid targets and implications for fast-ignition experiments on omega ep. *Physics of Plasmas*, **14**(5):056301, 2007.

[122] A. J. Mackinnon *et al.* Enhancement of proton acceleration by hot-electron recirculation in thin foils irradiated by ultraintense laser pulses. *Phys. Rev. Lett.*, **88**: 215006, 2002.

[123] A. Bret *et al.* Exact relativistic kinetic theory of an electron-beam˘plasma system: Hierarchy of the competing modes in the system-parameter space. *Phys. Rev. Lett.*, **100**:205008, May 2008.

[124] O. Buneman. Dissipation of currents in ionized media. *Phys. Rev.*, **115**:503–517, Aug 1959.

[125] E. S. Weibel. Spontaneously growing transverse waves in a plasma due to an anisotropic velocity distribution. *Phys. Rev. Lett.*, **2**:83–84, Feb 1959.

[126] R. Jung. PhD in Physics, Heinrich-Heine-Universität,Düsseldorf, 2007.

[127] M. Honda *et al.* Two-dimensional particle-in-cell simulation for magnetized transport of ultra-high relativistic currents in plasma. *Phys. of Plasmas*, **7**(4):1302–1308, 2000.

[128] A A Solodov *et al.* Simulations of electron-beam transport in solid-density targets and the role of magnetic collimation. *Journal of Physics: Conference Series*, **244**(2): 022063, 2010.

[129] H. S. Uhm. Theory of the filamentation instability in an intense electron beam propagating through a collisional plasma. *Physics of Fluids*, **26**(10):3098–3106, 1983.

[130] M. Manclossi *et al.* Study of ultraintense laser-produced fast-electron propagation and filamentation in insulator and metal foil targets by optical emission diagnostics. *Phys. Rev. Lett.*, **96**:125002, Mar 2006.

[131] A. Debayle *et al.* Filamentation instability of a fast electron beam in a dielectric target. *Phys. Rev. E*, **78**:066404, Dec 2008.

[132] A. Macchi *et al.* Laser acceleration of ion bunches at the front surface of overdense plasmas. *Phys. Rev. Lett.*, **94**:165003, Apr 2005.

[133] L. Yin *et al.* Three-dimensional dynamics of breakout afterburner ion acceleration using high-contrast short-pulse laser and nanoscale targets. *Phys. Rev. Lett.*, **107**:045003, Jul 2011.

[134] S. J. Gitomer *et al.* Fast ions and hot electrons in the laser–plasma interaction. *Phys. of Fluids*, **29**(8):2679–2688, 1986.

[135] J. Fuchs *et al.* Comparative spectra and efficiencies of ions laser-accelerated foward form the front and rear surfaces of thin solid foils. *Phys. Plasmas*, **14**: 053105, 2007.

[136] P. Mora. Plasma expansion into a vacuum. *Phys. Rev. Lett.*, **90**: 185002, 2003.

[137] M. C. Kaluza. PhD in Physics, Max-Planck-Institute,München, 2004.

[138] J. Fuchs *et al.* Laser-driven proton scaling laws and new paths towards energy increase. *Nat. Phys.*, **2**: 48, 2006.

[139] C. Perego *et al.* Target normal sheath acceleration analytical modeling, comparative study and developments. *Rev. Sci. Instr.*, **83**(2):02B502, 2012.

[140] P. Mora *et al.* Thin foil expansion into vacuum. *Phys. Rev. E*, **72**: 056401, 2005.

[141] A. Diaw **et al.** Thin-foil expansion into a vacuum with a two-temperature electron distribution function. *Phys. Rev. E*, **86**:026403, Aug 2012.

[142] M. Roth *et al.* Energetic ions generated by laser pulses: A detailed study on target properties. *Phys. Rev. ST. Accel. Beams*, **5**: 061301, 2002.

[143] R. A. Snavely *et al.* Intense high energy proton beams from petawatt laser irradiation of solids. *Phys. Rev. Lett.*, **85**: 2945, 2000.

[144] D. C. Carroll *et al.* Active manipulation of the spatial energy distribution of laser-accelerated proton beams. *Phys. Rev. E*, **76**: 065401, 2007.

[145] L. Romagnani *et al.* Dynamics of electric fields driving the laser acceleration of multi-mev protons. *Phys. Rev. Lett.*, **95**: 195001, 2005.

[146] E Brambrink *et al.* Modeling of the electrostatic sheath shape on the rear target surface in short-pulse laser-driven proton acceleration. *Laser and Particle Beams*, **24**:163–168.

[147] H. Ruhl *et al.* The generation of micro-fiducials in laser accelerated proton flows, their imaging property of surface structures and application for the characterization of the flow. *Phys. Plasmas*, **11**: L17, 2004.

[148] M. Borghesi *et al.* Multi-mev proton source investigations in ultra intense laser foil interaction. *Phys. Rev. Lett.*, **92**: 055003, 2004.

[149] F. Nürnberg *et al.* Radiochromic film imaging spectroscopy of laser-accelerated proton beams. *Rev. Sci. Instrum.*, **80**: 033301, 2009.

[150] J. Fuchs *et al.* Comparison of laser ion acceleration from the front and rear surfaces of thin foils. *Phys. Rev. Lett.*, **94**: 045004, 2005.

[151] K. Zeil *et al.* The scaling of proton energies in ultrashort pulse laser plasma acceleration. *New Journal of Physics*, **12**(4):045015, 2010.

[152] MacPhee *et. al.* Diagnostics for fast ignition science (invited). *Rev. Sci. Instrum.*, **79**(10):10F302, 2008.

[153] R. Benattar *et al.* Polarized light interferometer for laser fusion studies. *Rev. Sci. Inst.*, **50**(12):1583–1586, 1979.

[154] I. Watts *et al.* Dynamics of the critical surface in high-intensity laser-solid interactions: Modulation of the xuv harmonic spectra. *Phys. Rev. Lett.*, **88**:155001, Mar 2002.

[155] J. A. Koch *et al.* High-energy x-ray microscopy techniques for laser-fusion plasma research at the national ignition facility. *Appl. Opt.*, **37**(10): 1784–1795, 1998.

[156] C. Bellei *et. al.* Coherent transition radiation in relativistic lasersolid interactions. *Plasma Phys. Control. Fusion*, **54**(3):035011, 2012.

[157] R. Nolte *et al.* A tld-based few-channel spectrometer for x ray fields with high fluence rates. *Radiation Protection Dosimetry*, **84**(1-4):367–370, 1999.

[158] E. B. Treacy. Optical pulse compression with diffraction gratings. *IEEE J. Quantum Electron. QE-5*, page 454, 1969.

[159] G. Cheriaux. PhD in Physics, Universit Paris 11, France, 1997.

[160] G. Chériaux*et al.* Aberration-free stretcher design for ultrashort-pulse amplification. *Opt. Lett.*, **21**(6):414–416, 1996.

[161] A. Öffner. U.s. patent 3,748,015. 1971.

[162] `https://www.cvimellesgriot.com`.

[163] C. A. Quarles. Semiempirical analysis of electron-induced k-shell ionization. *Phys. Rev. A*, **13**:1278–1280, Mar 1976.

[164] J. H. Hubbell *et al.* A review, bibliography, and tabulation of k, l, and higher atomic shell x-ray fluorescence yields. *Journal of Physical and Chemical Reference Data*, **23**(2):339–364, 1994.

[165] H.-K. Chung *et al.* Flychk: Generalized population kinetics and spectral model for rapid spectroscopic analysis for all elements. *High Energy Density Physics*, **1**(1):3–12, 2005.

[166] S. N. Chen *et al.* X-ray spectroscopy of buried layer foils irradiated at laser intensities in excess of 10^{20} w/cm^2. *Phys. Plasma*, **16**(6):062701, 2009.

[167] E. Förster *et al.* X-ray microscopy of laser-produced plasmas with the use of bent crystals. *Las. Part. Beams*, **9**:135–148, Aug 1991.

[168] Y. Aglitskiy *et al.* High-resolution monochromatic x-ray imaging system based on spherically bent crystals. *Appl. Opt.*, **37**(22):5253–5261, Aug 1998.

[169] J. A. King *et al.* Ti $K\alpha$ radiography of Cu-doped plastic microshell implosions via spherically bent crystal imaging . *Appl. Phys. Lett.*, **86**: 191501, 2005.

[170] `http://www.fujifilm.com/`.

[171] F. Peréz. PhD in Physics, Ecole Polytechnique,France, 2010.

[172] C. A. Quarles *et al.* Differential cross section for k-shell ionization of copper and silver by electron bombardment. *Phys. Rev. Lett.*, **31**: 859–862, 1973.

[173] `http://online1.ispcorp.com/_layouts/Gafchromic/index.html`.

[174] `http://www.srim.org/SRIM/SRIMLEGL.htm`.

[175] C. K. Birdsall and A. B. Langdon. *Plasma Physics Via Computer Simulation.* Taylor & Francis, New York, 2005.

[176] P. J. Roache. *Fundamentals of Computational Fluid Dynamics.* Hermosa Pub; Revised edition (Jan 2003), 2003.

[177] R. J. Kingham *et al.* Nonlocal magnetic-field generation in plasmas without density gradients. *Phys. Rev. Lett.*, **88**:045004, Jan 2002.

[178] A. R. Bell *et al.* Fast electron transport in laser-produced plasmas and the kalos code for solution of the vlasovfokkerplanck equation. *Plasma Phys. Control. Fusion*, **48**(3):R37, 2006.

[179] R. Fonseca *et al. Lect. Notes Comput. Sci.*, **2331**:342–351, 2002.

[180] J. C. Joachim. Quantum collision theory. *(North-Holland Amsterdam)*, 3rd ed., 1987.

[181] International committee on radiation units report no. 37. *ICRU Bethesda MD*, 1984.

[182] Y. Sentoku *et al.* High energy proton acceleration in interaction of short laser pulse with dense plasma target. *Phys. of Plasmas*, **10**(5):2009–2015, 2003.

[183] D. S. Hey *et al.* Laser-accelerated proton conversion efficiency thickness scaling. *Phys. of Plasmas*, **16**(12):123108, 2009.

[184] C. N. Danson *et al.* Well characterized $10^{19}\,w\,/cm^2$ operation of vulcanan ultra-high power nd:glass laser. *J. Mod. Optic.*, **45**(8):1653–1669, 1998.

[185] P. McKenna *et al.* Lateral electron transport in high-intensity laser irradiated foils diagnosed by ion emission. *Phys. Rev. Lett*, **98**: 145001, 2007.

[186] X. H. Yuan *et al.* Effect of self-generated magnetic fields on fast-electron beam divergence in solid targets. *New J. Phys.*, **12**: 063018, 2010.

[187] P. McKenna *et al.* Effects of front surface plasma expansion on proton acceleration in ultraintense laser irradiation of foil targets. *Las. Part. Beams*, **26**: 591, 2008.

[188] D. Batani. Studies on fast electron transport in the context of fast ignition. *NUKLEONIKA*, **56**, 2011.

[189] M. N. Quinn *et al.* Refluxing of fast electrons in solid targets irradiated by intense, picosecond laser pulses. *Plasma Phys. Control. Fusion*, **53**: 025007, 2011.

[190] S. Agostinelli *et al.* Geant4a simulation toolkit. *Nuclear Instruments and Methods in Physics Research Section A: Accelerators, Spectrometers, Detectors and Associated Equipment*, **506**(3): 250–303, 2003.

[191] M. H. Key. Status of and prospects for the fast ignition inertial fusion concept. *Phys. of Plasmas*, **14**(5):055502, 2007.

[192] L. Robson *et al.* Scaling of proton acceleration driven by petawatt laser plasma interactions. *Nature Physics*, **3**: 58, 2007.

[193] J. S. Green *et al.* Enhanced proton flux in the mev range by defocused laser irradiation. *New J. Phys.*, **12**(8):085012, 2010.

[194] C. M. Brenner *et al.* Dependence of laser accelerated protons on laser energy following the interaction of defocused, intense laser pulses with ultra-thin targets. *Laser Part. Beams*, **29**:345–351, 8 2011.

[195] M. Passoni *et al.* Target normal sheath acceleration: theory comparison with experiments and future perspectives. *New J. Phys.*, **12**: 045012, 2010.

[196] M. H. Xu *et al.* Enhancement of ion generation in femtosecond ultraintense laser-foil interactions by defocusing. *Appl. Phys. Lett.*, **100**(8):084101, 2012.

[197] W. J. Smith. *Modern Optical Engineering, 4th Ed.: The Design of Optical Systems*. McGraw-Hill, New York, 2008.

[198] R. J. Gray *et al.* Surface transport of energetic electrons in intense picosecond laser-foil interactions. *Appl. Phys. Lett.*, **99**(17): 171502, 2011.

[199] R. J. Gray *et al.* In preparation. .

[200] Sun Guo-Zheng *et al.* Self-focusing of short intense pulses in plasmas. *Phys. Fluids*, **30**(2): 526–532, 1987.

[201] Claire Ellen Max *et al.* Self-modulation and self-focusing of electromagnetic waves in plasmas. *Phys. Rev. Lett.*, **33**: 209–212, Jul 1974.

[202] J. P. Freidberg *et al.* Resonant absorption of laser light by plasma targets. *Phys. Rev. Lett.*, **28**: 795–799, Mar 1972.

[203] T. Tajima *et al.* Laser electron accelerator. *Phys. Rev. Lett.*, **43**: 267–270, Jul 1979.

[204] V. Malka. Laser plasma accelerators. *Phys. Plasmas*, **19**(5): 055501, 2012.

[205] K. A. Tanaka *et al.* Studies of ultra-intense laser plasma interactions for fast ignition. *Phys. Plasmas*, **7**(5): 2014–2022, 2000.

[206] R. Mishra *et al.* Hot electron generation forming a steep interface in super-intense laser-matter interaction. *Phys. Plasmas*, **16**(11): 112704, 2009.

[207] G.J Pert. Algorithms for the self-consistent generation of magnetic fields in plasmas. *J. Comput. Phys.*, 43(1):111 – 163, 1981.

[208] R. H. H Scott *et al.* Controlling fast-electron-beam divergence using two laser pulses. *Phys. Rev. Lett.*, **109**:015001, Jul 2012.